Understanding Learning Control of Molecular Fragmentation

A Dissertation Presented

by

David Michael Cardoza

to

The Graduate School

in Partial Fulfillment of the Requirements

for the Degree of

Doctor of Philosophy

in

Physics

Stony Brook University

June 2006

Stony Brook University

The Graduate School

David Michael Cardoza

We, the Dissertation committee for the above candidate for the Doctor of Philosophy degree, hereby recommend acceptance of the Dissertation.

Thomas C. Weinacht, Thesis Advisor

Assistant Professor, Department of Physics and Astronomy

Dominik Schneble

Assistant Professor, Department of Physics and Astronomy

Philip Johnson

Professor, Department of Physics and Astronomy

Jacobus Verbaarschot

Professor, Department of Physics and Astronomy

This Dissertation is accepted by the Graduate School.

Dean of the Graduate School

Abstract of the Dissertation

Understanding Learning Control of Molecular Fragmentation

by

David Michael Cardoza

Doctor of Philosophy

in

Physics

Stony Brook University

2006

This thesis describes efforts that we have made in trying to understand learning control of molecular fragmentation. In particular,we will discuss how we understood and developed a model for control in trifluoroacetone (CH_3COCF_3, TFA). Using this model, we were able to make predictions about control in a family of molecules. Family members included trichloroacetone (CH_3COCCl_3, TCA) and trideuteratedacetone (CH_3COCD_3, TDA). We will show that we are able to predict control in these molecules using our control model. We also discuss how our model extends to the molecule dimbromo-trifluoroacetone ($CHBr_2COCF_3$, Br2TFA). By changing the structure of the molecule, we see

that the control mechanism changes to charge transfer. Finally, pump-probe measurements in the halogenated ketones have shown that we are measuring the quantum mechanical probability density of the dissociative wave packet in these molecules. We will discuss current and future efforts that involve performing dynamic wave packet interferometry to measure the phase and amplitude of these dissociative wave functions. These measurements may lead to the making of detailed molecular movies of dissociation, and to the knowledge of the complicated shapes of the these dissociative potential energy surfaces along the dissociative coordinate in polyatomic molecules.

To Linda and Kara, without whom this would have never been possible.

Contents

List of Figures

Acknowledgements

This may be the most difficult section of the dissertation to write. I know that I will probably forget to thank some people who were instrumental in helping me reach this point. To those of you who don't find your names, please know that you are appreciated.

The first person I would like to thank is Thomas Weinacht. I came to him one day and asked him about ultrafast processes and how his work investigated them. Three and a half years later I have gained the awesome experience of working in a world class laboratory with a world class scientist. I truly appreciate Tom giving me a chance, knowing that I had little research experience. I don't think that I will ever truly be able to pay him back for giving me this opportunity. Thanks Tom.

The second person I have to thank is the man who introduced me to Tom, Luis Orozco. He took this nervous kid who was initially to scared to talk to Tom and introduced me to him. So maybe he should have been first thanked...

Part of the fun of this dissertation was coming into a mostly empty laboratory, and building an experimental apparatus. Partick Neurnberger and I spent some pretty wild nights working in the lab. I would like to think that we ended up being pretty good experimentalists, but I would not consider us great plumbers! Florian Langhojer was another Weurzburg exchange student whom with I worked extensively. He taught me some neat code tricks, and without these tricks I probably would still be writing incomprehensible code (although some may say it is still not crystal clear!).

Carlos Trallero has been a friend and a colleague for many years now. I have enjoyed having conversations about both lab work and sports over the years. Sarah Nichols and Brett Pearson have always provided helpful suggestions, particularly about writing and conference talks, which I feel are both weak points of mine. I don't know how many people thank undergraduates in the lab, but Brendan Keller has been an outstanding student to work with and deserves the thanks. He has contributed a lot to this lab and to my work over the past year. Others who have been in the lab and have contributed to making it a happy place are Dominik Maxein, Dan Flickinger, Jay Brown and Doug Broege. I could not of imagined that I would have had such great "labmates". Thanks everyone.

I would also like to thank my family back in California. They have always

supported my goals, and gave me encouragement when I was down. I want to thank Kara, for teaching me what it means to be a person. She is the first person to teach me how to put things into perspective. Funny how someone who cannot talk yet can teach you something. And last, but certainly not least, I would like to thank my wife, Linda. I would never have stayed in college if it wasn't for her. When I was about to drop out and give up, she convinced me to stay in school. Everything that I have accomplished up to this point academically and in life is due to her seeing potential in me. I want it to be documented that my success is actually her success and that this degree has been earned by her as well. Thanks honey, for keeping me on the right track and for making everyday the best day.

Chapter 1

Introduction

Controlling molecular phenomena on a microscopic level has been a goal of researchers since the advent of the laser. In particular, people have been interested in selectively breaking bonds in large, polyatomic molecules [1]. It was once thought that if one could tune the frequency of a laser to match the vibrational mode of a given bond in one of these polyatomic molecules, then one could resonantly break that particular bond. However, it was soon realized that intramolecular energy redistribution would almost always cause the weaker bonds to break first. Researchers found that if bond selective chemistry was to become reality, methods would have to be devised to beat this intramolecular energy redistribution.

In the late 1980's, the idea of coherent control was developed. One of these theories, developed by Tannor and Rice , suggested that by controlling wave

packet evolution, one could allow for the selection of the final product of a chemical reaction [2]. This time domain approach to coherent control relies on the fact that a vibrational wave packet will be launched onto a molecular excited electronic state at time t_1. As time evolves, this wave packet will evolve on this excited state. At another time t_2 later, the wave packet can be "dumped" back down onto the ground electronic state at a location where the selected products of the chemical reaction are produced. Another approach, developed by Brumer and Shapiro, takes a frequency domain approach to the problem [3].

Zhu *et. al* presented the first experimental demonstration of coherent control by modulating the products of the molecule HI simply by altering the phase relationship between two, continuous wave lasers with frequencies ω and 3ω [4]. This simple experimental demonstration of control sparked wide spread interest in coherently controlling chemical reactions. In particular, interest was directed to more complicated control and to control reactions in large, polyatomic molecules.

Another major advancement to the field of coherent control arose with the development of ultrafast laser systems. These broadband laser sources are capable of producing pulses with time durations on the order of the vibrational periods of many molecular modes ($\sim 10^{-14}$ s). They are also capable of pro-

ducing electric fields comparable to the field that binds the electron to the proton in a hydrogen atom. With high electric field strengths, and timescales comparable to vibrational periods of molecular bonds, these laser pulses can both beat the intramolecular energy redistribution and also Stark shift electronic states into and out of resonance, which is not possible with low intensity laser sources. Shortly after the introduction of the ultrafast laser pulse, it was found that these pulses could be shaped in time [5, 6]. With the ability to shape the electric field in time, then one could design pulses that optimally control wave packet evolution.

The process of finding the appropriate shape to control a particular dissociative reaction, however, is not trivial. In large polyatomic molecules, it is difficult to obtain an exact analytic form of the Hamiltonian. Detailed knowledge of the Hamiltonian is needed to *a priori* design a shaped laser pulse. The problem becomes more difficult when one considers the interaction of the strong electric field with the molecule. This problem was addressed by Judson and Rabitz [7]. They proposed that feedback could be used to find the appropriate pulse shape. This method, called closed-loop learning control, uses global optimization algorithms (e.g. Genetic Algorithms) that find a shape of the laser electric field to control a particular reaction by trial and error and by combining pulse shape features of successful pulse shapes. This feed-

back approach has the advantage that one needs little or no prior information about the molecular Hamiltonian to obtain a tailored electric field to control a molecular reaction.

In recent years, there have been many demonstrations of control over various molecular processes using closed-loop learning control and pulse shaping. [8, 9, 10, 11, 12, 13, 14]. This method has been shown to be successful in controlling various phenomena such as molecular fragmentation, high harmonic generation and florescence. While closed-loop learning control typically works well at controlling molecular dynamics, it unfortunately provides no explanation for why the control worked. This means that a complete understanding of the molecular mechanism that yielded the control is not readily understood. One has to use the optimized pulse obtained from the learning control process to try and understand the dynamics responsible for the control. Recent efforts have concentrated on understanding the solutions found by learning algorithms. It has been shown in a few cases that information about the control mechanism can be obtained by analyzing the optimal pulse solution [15, 16, 17, 18].

This thesis work began at the time when efforts were being made to not only control molecular dynamics using closed-loop learning control, but to also develop methods to understand the solutions yielded by the learning al-

gorithms. My thesis work has concentrated on trying to develop and use these methods to understand solutions found in learning control. In Chapter 3, we will discuss techniques that we have developed that have helped us to understand control mechanisms. These methods helped us to find an understanding of the control mechanism responsible for control over the CF_3^+/CH_3^+ ratio in 1,1,1-trifluoroacetone.

In Chapter 4, we analyze the data from the control experiments, and show that we understand the control mechanism. We interpret the results in terms of a time domain, wave packet picture. We develop a model for the control mechanism in an effort to make predictions about control in similar but different molecules. In Chapter 5, we show that we can use our model to successfully make predictions about how the control mechanism changes with the structure of the molecule. By extending the control model to this family of molecules, we are advancing the idea that shaped, ultrafast laser pulses can be used as "photonic reagents" in chemical reactions.

In Chapter 6, we discuss how the control mechanism changes when we make another change to the molecular structure. We find that charge transfer will play a role in the control mechanism.

Finally, in Chapter 7, we discuss how our efforts to understand control in the halogenated acetones has opened up other interesting opportunities for

controlling molecular dynamics. We discuss our current efforts that have concentrated on trying to measure the dissociative wavefunction of a polyatomic molecule. Preliminary data indicates that these types of wavefunction imaging experiments are feasible.

Chapter 2

Experimental Apparatus

The laser system employed in our experiments consists of a Kerr-lens mode-locked Titanium:Sapphire oscillator (KM Labs) that seeds a Titanium:Sapphire chirped-pulse amplified ultrafast laser system (KM Labs HAP-AMP) in a multi-pass configuration [19]. It is capable of producing 30 fs pulses at a repetition rate of 1 kHz. The pulse energies are typically $\sim$ 1 mJ. Figure 2.1 shows the intensity and phase as a function of time for a pulse from our amplifier. All of the pulses that are discussed in this thesis are characterized using second-harmonic generation frequency resolved optical gating (SHG FROG) [20, 21].

The experimental setup is shown in Figure 2.2. Pulses from the amplifier are injected into a Mach-Zender interferometer, where the pulse is split into a reference pulse and a shaped pulse. The reference arm of the interferometer is

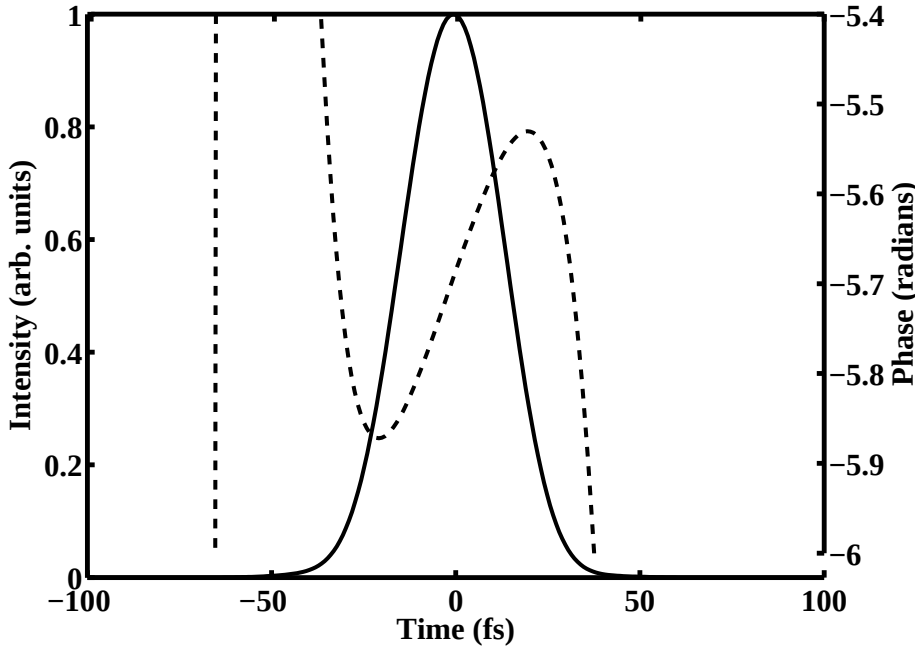

Figure 2.1 ($I(t)$ and $\phi(t)$ for pulse from our amplifier.

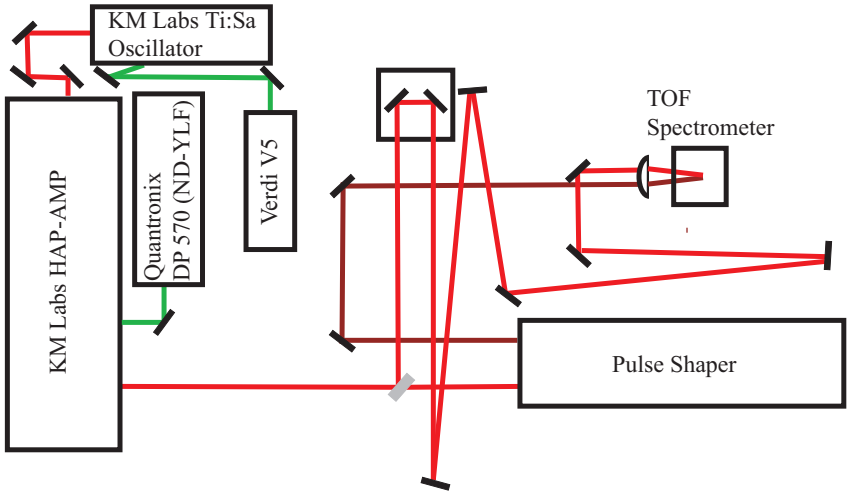

Figure 2.2 Diagram of experimental setup.

equipped with a stepper motor (Zaber Technologies T-LA28) and stage that allow us to control the length of the reference arm, which translates into a time delay between the shaped and reference pulse. The minimum travel step size of the stepper motor is 100 nm which gives us time resolution of ~ 0.33 fs. This allows us to perform pump-probe spectroscopy with ~ 1 fs resolution. The other arm of the interferometer contains the pulse shaper, which is discussed in more detail below. The pulses coming out of the arms of the interferometer are then sent through a 150 mm lens that focuses the pulses into a time-of-flight mass spectrometer (TOFMS) which is under high vacuum (pressure $\sim 1\times10^{-6}$ torr) where an effusive molecular beam is injected between two acceleration plates. The pulses in the focus are both spatially and temporally overlapped. It is here where the laser pulses dissociatively ionize molecules in the beam.

Figure 2.3 shows the apparatus that feeds the molecules into our TOFMS. Liquid samples are placed into the sample holder shown in Fig. 2.3. To ensure that the sample was not contaminated by air, we performed freeze-pump cycles by submerging the sample holder into liquid nitrogen. Vacuum valve B remained closed during the freeze pump cycle, while vacuum valve A remained open to pump contaminants out of the sample during the freeze-pump cycle. Vacuum valve B was then opened to allow molecules into the entrance manifold, shown in Fig. 2.3(b). The two-dimensional translation stage allowed us

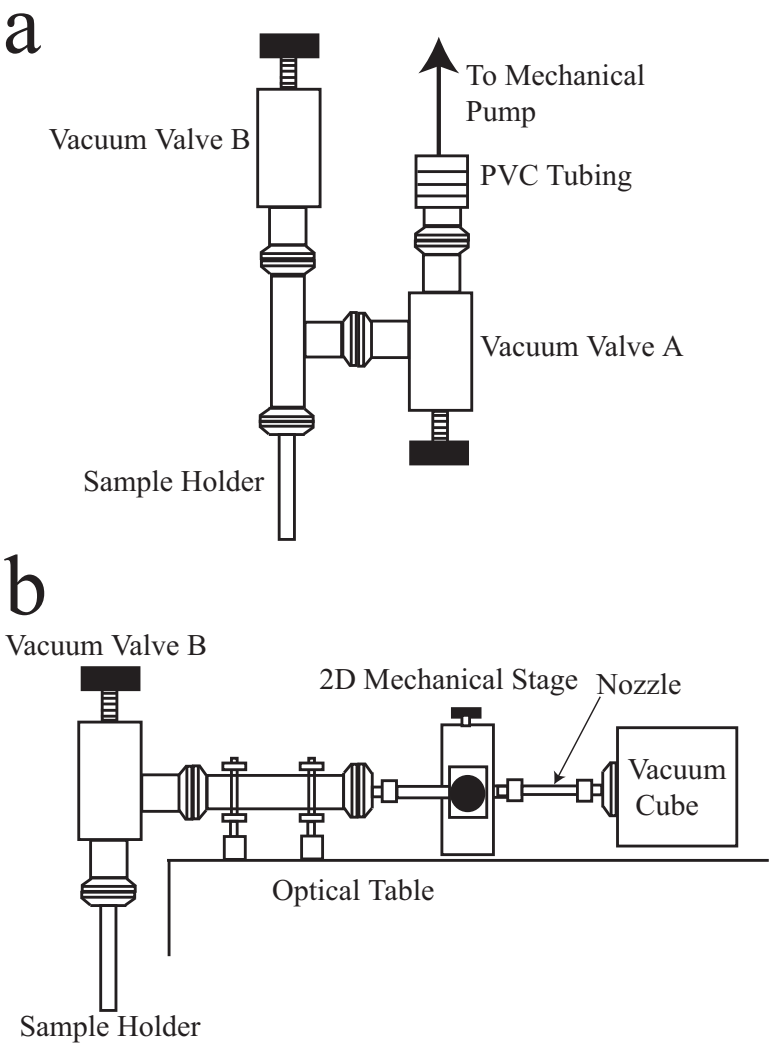

Figure 2.3 (a) Front view of manifold (b) Side view.

to vary the position of the molecular beam nozzle relative to the laser focus. Ultra-Torr fittings acted as motion feedthroughs. We typically allowed sample pressures in the vacuum chamber to reach $\sim 5\times10^{-6}$ - 2×10^{-5} torr. Pressures in the manifold shown in Fig. 2.3(b) were typically much higher, usually ~ 10

torr. The molecular beam is fed into the TOFMS by a 1/4 inch outer diameter stainless steel tube that has a 1/16 inch thick disk welded to be vacuum tight onto the stainless steel tube. The stainless steel disc was machined with the amplified laser system to have a hole ~ 50 μm in diameter. This hole acts as the nozzle that feeds the molecular gas into the plate assembly.

Figure 2.4(a) shows a diagram of the acceleration plate assembly. A number of modifications have been made to this assembly since its original construction [21]. The plate assembly is held by four nylon rods with 8-32 thread (Microplastics) which are screwed into a homemade O-ring holder [21]. The two plates are separated by 0.76 cm. This plate separation is made constant and easily fixed by the machinable glass (Macor) standoffs, which are 6.7 mm in diameter. Prior designs had the plates held by nylon 8-32 nuts [21], but it was found that these nylon parts would easily hold a charge which produced stray, unpredictable electric fields. The standoffs were designed to not protrude as far into the interaction region, thereby not modifying the electric field between the plates. The plates are then fixed to the assembly by 8-32 nuts which sit on top of the top plate.

The ions are accelerated through the two plates by an electric field that is created by placing +750 V on the bottom plate. The top plate is grounded to the optical table on which it sits via an electrical feedthrough. The top

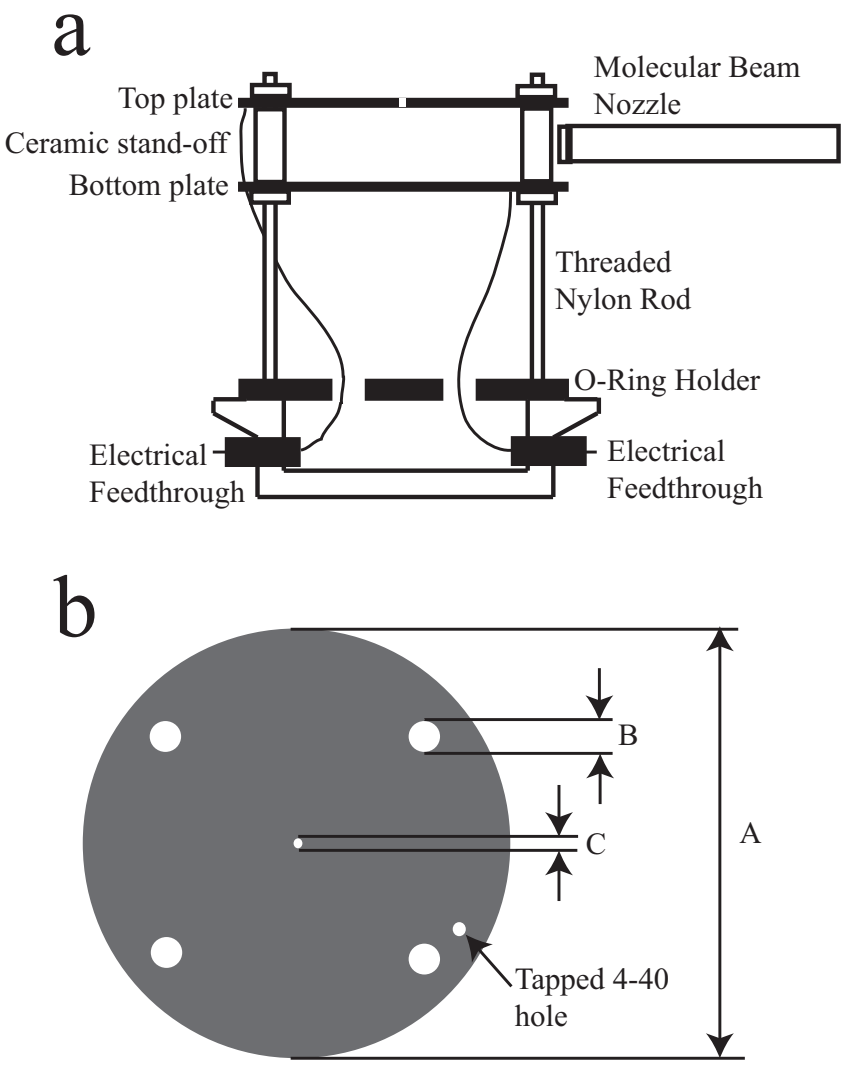

Figure 2.4 (a) Acceleration plate assembly. (b) Top view of top acceleration plate. The distances are A=3.5 cm, B=0.4 cm and C=500μm.

plate is shown in Fig. 2.4(b). A hole was machined in the middle of the plate to be 500μm in diameter. The size of the hole was chosen to act as both an aperture to reduce the effects of intensity volume averaging, and to act as a rough kinetic energy filter. This will be discussed further in Chapter 4. After

acceleration through the aperture, the molecules then see a field free region. It is here that the lighter molecular ion fragments, which acquired a faster velocity in the acceleration plate region, begin to pull away from the heavier ions. The field-free region is $\sim$ 45 cm in length.

The time resolved ions were detected by a dual microchannel plate (MCP) assembly in the Chevron configuration [21]. The front steel electrode typically had voltages of -1900 V applied, which helped to accelerate the cations into the plate assembly. The threaded nylon rods (Microplastics) and nylon nuts in front of the front steel electrode were covered with a thin film of graphite to help prevent any excess charge buildup. We then applied 30 V to the MCP back steel electrode to help accelerate the cascading electrons from the cation impact into the steel anode. The signal from the anode was typically sent into a 350 MHz pre-amplifier (Stanford Research Systems SIM914) where the output anode signal was amplified. The signal from the pre-amplifier was then monitored with a 500 MHz, 8-bit computer based oscilloscope (GAGE Compuscope 8500).

A typical TOF spectrum is shown in Figure 2.5. This spectrum was taken with only the background gas in the chamber, at a pressure of 7×10^{-7} torr. The major peaks in the spectrum are H_2O^+, N_2^+, and O_2^+. These peaks are associated with air. We can also see small amounts of H^+, which also comes

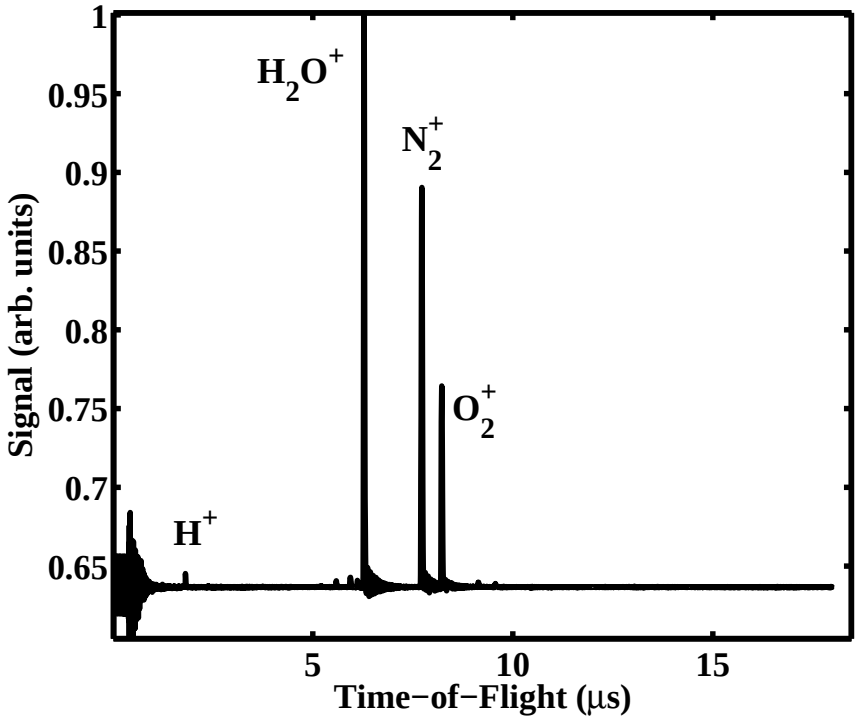

Figure 2.5 TOF spectrum taken of the background gas in the TOFMS.

from air and from outgassing from the stainless steel in the chamber. The turbo pump is not efficient at pumping out H^+.

To aid in finding spatial and temporal overlap of the two pulses, we have a 200 mm lens that images the crossing point between the laser focus and the molecular beam. We split the image beam into two arms, where one arm is sent to a screen to optimize spatial overlap of the laser pulses. The other arm is sent to a nonlinear optical crystal where we optimize temporal overlap. An external view of the entire chamber with lenses is shown in Figure 2.6.

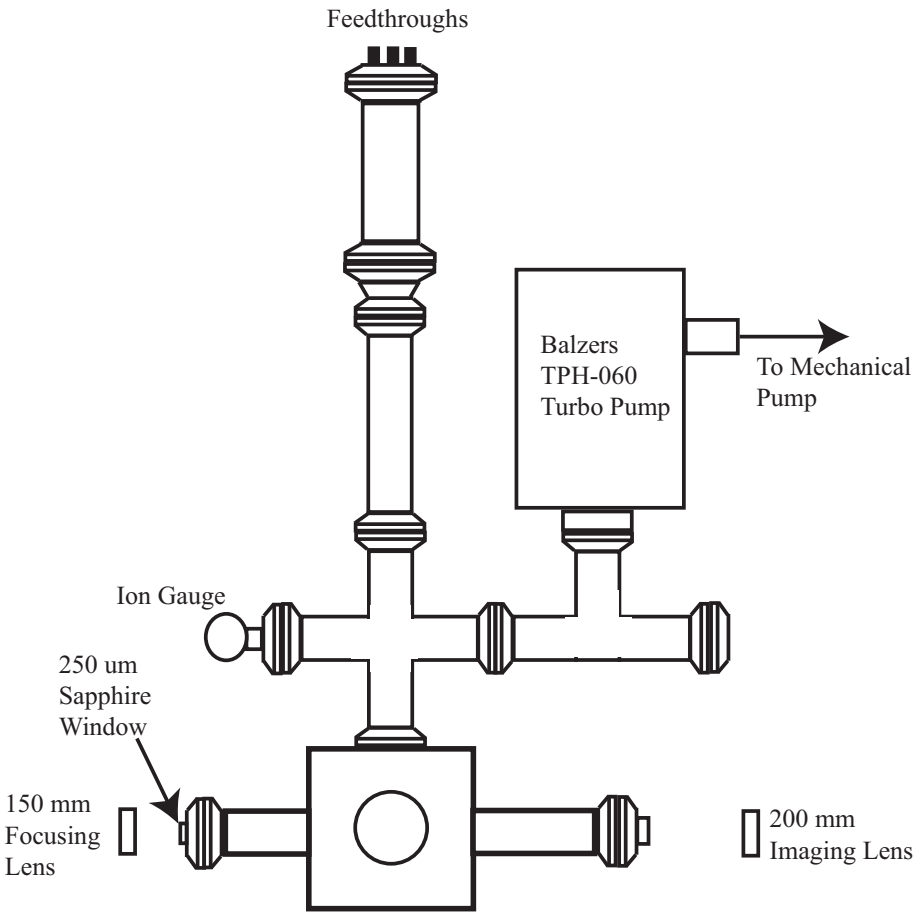

Figure 2.6 Outer view of time-of-flight mass spectrometer.

2.1 Pulse Shaper

Because the laser pulses are temporally faster than any electronics, it is impossible to shape the laser pulses without performing some "trick". To get around the fact that the pulses are short, we use the method developed by Weiner [5].

Figure 2.7 shows a schematic diagram of the pulse shaper that we use. The

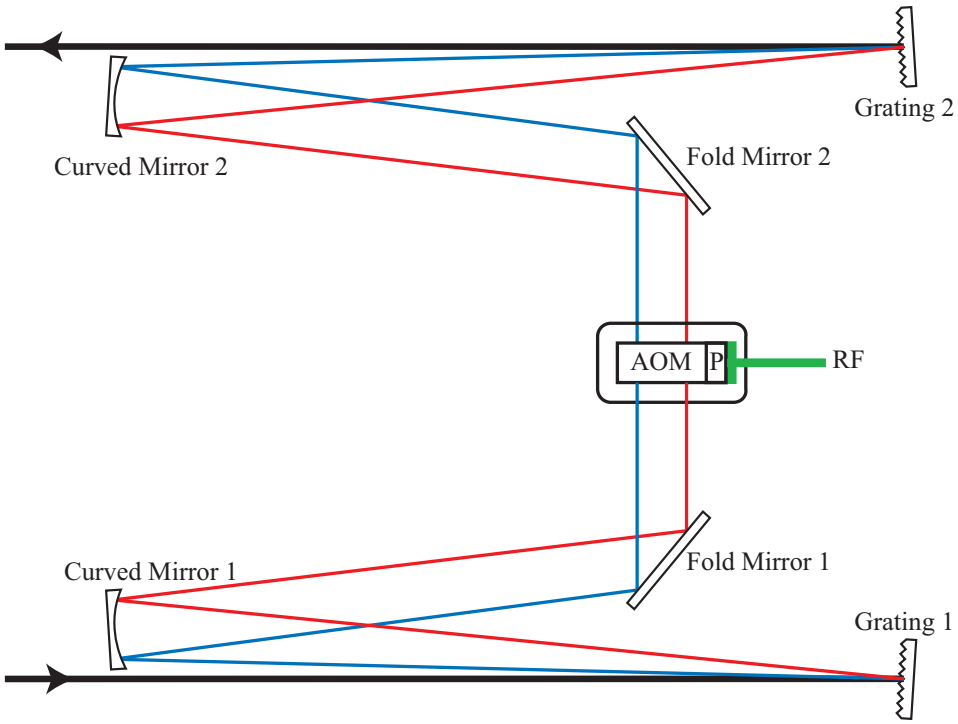

Figure 2.7 Diagram of pulse shaper.

ultrafast laser pulses are dispersed by a diffraction grating, causing each color in our spectrum to be mapped to a particular angle. The dispersed light is then collimated by a reflective focusing element. This collimates the dispersed light, thereby mapping each color in the spectrum to a particular point in space, i.e. making a "ribbon" of light. At the Fourier plane of the focusing element we place a programmable phase modulating mask (in our case an acousto-optic modulator (AOM) [6]), that allows us to manipulate the phase between groups of adjacent frequency components. If we have the incoming

pulse $E(\omega)$, then after the AOM, we have

$$E(\omega)_{shaped} = E(\omega)e^{i\phi(\omega)}M(\omega) \tag{2.1}$$

Where $M(\omega)$ is the frequency dependent transfer function that represents the AOM. $M(\omega)$ is dependent on the spatial overlap of the laser spectrum and the RF wave [6]. We manipulate $\phi(\omega)$ by manipulating the temporal phase of the acoustic wave in the AOM crystal. The AOM behaves like a transmission grating, where the grooves are the compressions and rarefactions of the sound wave in the AOM crystal. By manipulating the phase of the acoustic wave about the central RF frequency, the different optical frequency components of the pulse will see different phases of the acoustic wave, thereby causing the colors to undergo slightly different dispersion. This causes the phase relationship between the different optical frequency components to change. The AOM also allows us to manipulate the amplitude of the spectral components by changing the amplitude of the acoustic wave. The light is then re-focused onto another grating, where the frequency components are placed back together. The result is a temporally shaped laser pulse.

Our AOM was designed to work at an RF central frequency of 150 MHz. The overall efficiency of the pulse shaper is typically 35%. This number is

affected both by the AOM and by the loss on the diffraction gratings. We tested the AOM to be about 65% efficient. The efficiency of the AOM takes into account both the crystal properties and the impedance network of the device. The efficiency is effected by how the transducer (the device that turns the electrical signal into an acoustic wave in the crystal) is matched to the crystal [22].

Figure 2.8 shows both the $I(t)$ and $\phi(t)$ from an SHG FROG reconstruction for an unshaped pulse from the AOM pulse shaper.

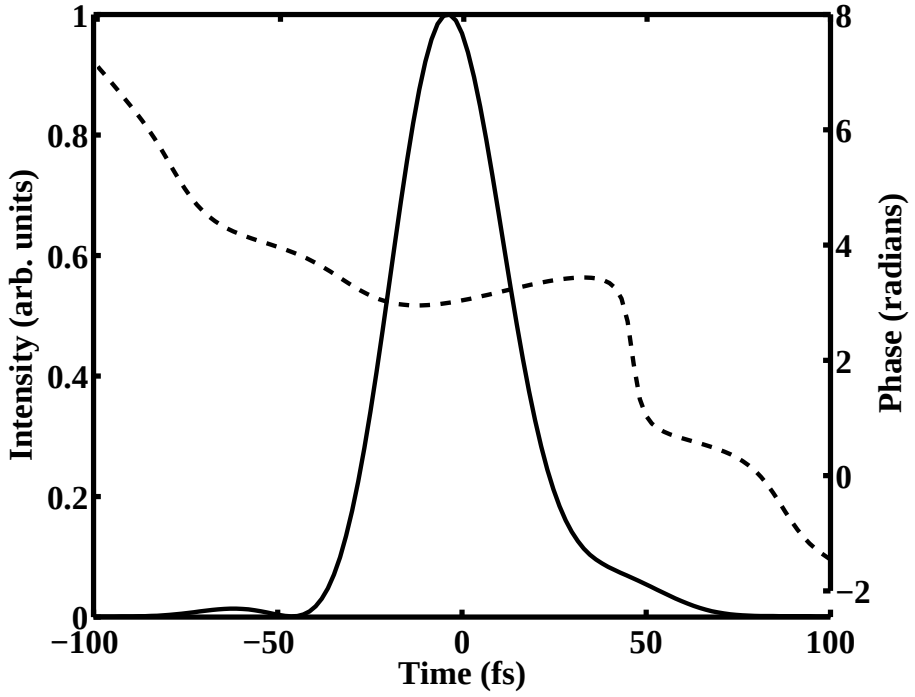

Figure 2.8 $I(t)$ and phase for an unshaped pulse from our pulse shaper.

As stated before, we shape the laser pulse by creating a shaped acoustic

wave in the AOM. We can manipulate the phase of the acoustic wave by using arbitrary waveform generators. We have employed two different methods for creating the RF waveforms that are used to create the shaped acoutic waves.

The first method that we used to create the acoustic waves was an RF mixing technique. The mixing method was implemented because we did not have an arbitrary waveform generator capable of producing a 150 MHz waveform. The dual waveform generators were capable generating points at a rate of 80 MHz. However, we recently implemented a new system for shaping pulses. The second method we used to shape the acoustic wave consisted of using a single waveform generator board (GAGE Compugen 11G), which can generate points at a rate 1 GHz. This board does allow us to create a 150 MHz waveform, which means that the mixing method is no longer needed. Here the waveform that is written directly from the board is

$$Y(t) = A(t)\cos(\Omega t + \phi(t)). \tag{2.2}$$

where $A(t)$ is the controllable amplitude, $\phi(t)$ again is the phase. With this new method, we now program the complete waveform as a function of time. We program on an RF pulse that is 8.5 μs long. We are capable of producing a maximum phase of 100π across the spectrum. If we put the maximum phase

shift into second order dispersion of the spectrum, we can make our 30 fs pulses come out of the pulse shaper with temporal widths of over 2 ps.

2.2 Closed-Loop Learning Control and the Genetic Algorithm

To find optimal pulse shapes to control molecular reactions, we utilize the method of closed-loop learning control [23, 24]. Figure 2.9 shows a diagram depicting the adaptive learning feedback system. A genetic algorithm (GA) runs the adaptive learning feedback loop. It is a global search algorithm that uses strategies adapted from natural selection. We will discuss how these strategies are used in the GA, and how they apply to pulse shape selective chemistry experiments.

Fig. 2.9 shows a diagram depicting a learning control feedback loop. The computer, armed with a GA, produces $\phi(\omega)$ for many different pulse shapes. These phases are the genetic codes for the pulse shapes. Because we shape our pulses in the frequency domain, this is a natural way to define the "genetic" makeup of the pulse. Each pulse shape is referred to as an *individual*. At the beginning of the adaptive learning feedback process, the GA generates a collection of pulses, called a *population*. We typically have populations that

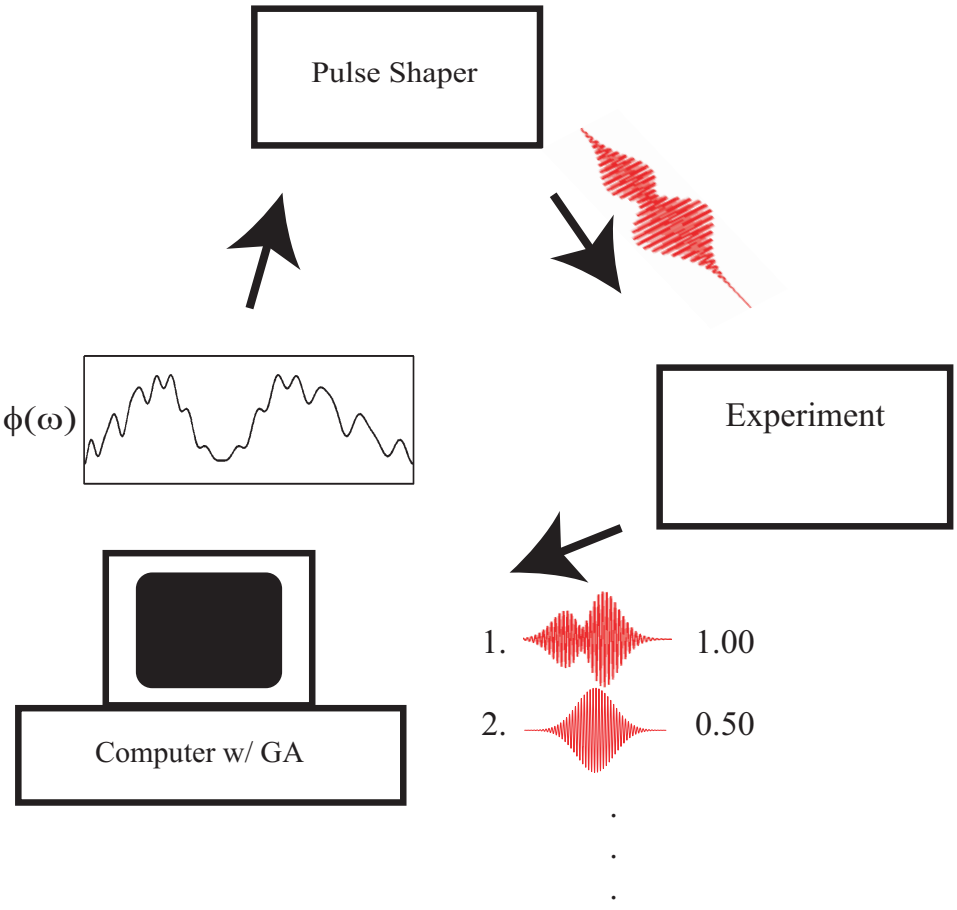

Figure 2.9 Diagram depicting the feedback system used to find optimal pulse shapes.

consist of forty pulse shapes. These pulses can either be completely random, which corresponds to a large initial sampling of the solution space, or they can be centered around a bias solution. Typically in our experiments, we bias the initial population to be centered around a transform limited pulse shape, which corresponds to a pulse with no phase. However, any pulse shape can serve as the bias. The distribution of the initial population around the bias

pulse shape can also be adjusted. This determines how large a portion of the solution space will initially be sampled by the initial population.

After the first population of pulse shapes are generated by the GA, they are programmed onto the AOM pulse shaper. The shaped laser pulses are then sent to the experiment. The results of the experiment are recorded on our computer based oscilloscope. At the beginning of the adaptive learning feedback process, we define a goal that determines what we would like to optimize. In this thesis, this goal will be to selectively enhance the production of one molecular fragment at the expense of another. The GA evaluates each pulse shape by how well it performed with respect to the goal that was defined. This evaluation assigns a number to the pulse shape called the *fitness*. In our GA, higher fitness values correspond to greater success with respect to the control goal.

The GA ranks pulse shapes from highest to lowest fitness. It is here that we program a threshold for how many pulse shapes were successful at accomplishing the defined goal. Those pulse shapes that performed poorly with respect to the control goal will be eliminated from the optimization process. The pulse shapes that perform well are selected to move on to operators that mix the genetic code of the best pulse shapes. These are called *mating* operators. In our GA, we typically take the top 50% of pulse shapes to move on to

the mating process. The mating operators accomplish what mating in nature accomplishes: genetic diversity, or the swapping of genetic material between the pulse shapes. We use only two main mating operators, *two-point crossover* and *mutation*. This is in contrast to other operators that can be used [23, 24]. We discuss the details of these operators in Appendix A. Typically, 70% of the pulse shapes are sent to two-point crossover and 20% are sent to the mutation operator. The other 10% are considered to be the best pulse shapes of the group, and are passed on in the GA through a process called *elitism*. The pulse shapes that are considered elite are not modified in any way. Elitism ensures that the best genetic material is not lost as there is a small chance that the mating operators can create pulse shapes that will have an overall lower fitness.

After the mating operations, *children* pulse shapes are created. Each iteration of the GA is referred to as a *generation*. Typically, 20-100 generations are needed for convergence, which is defined as zero change in the overall fitness. We can monitor the optimization process by looking at the average fitness of the best N pulse shapes from each generation. Figure 2.10 shows a typical fitness graph which is seen during the GA optimization process. It can be seen from Fig. 2.10 that the fitness initially starts out poor, but then undergoes a rapid growth. At the end of the optimization, the fitness growth begins slow

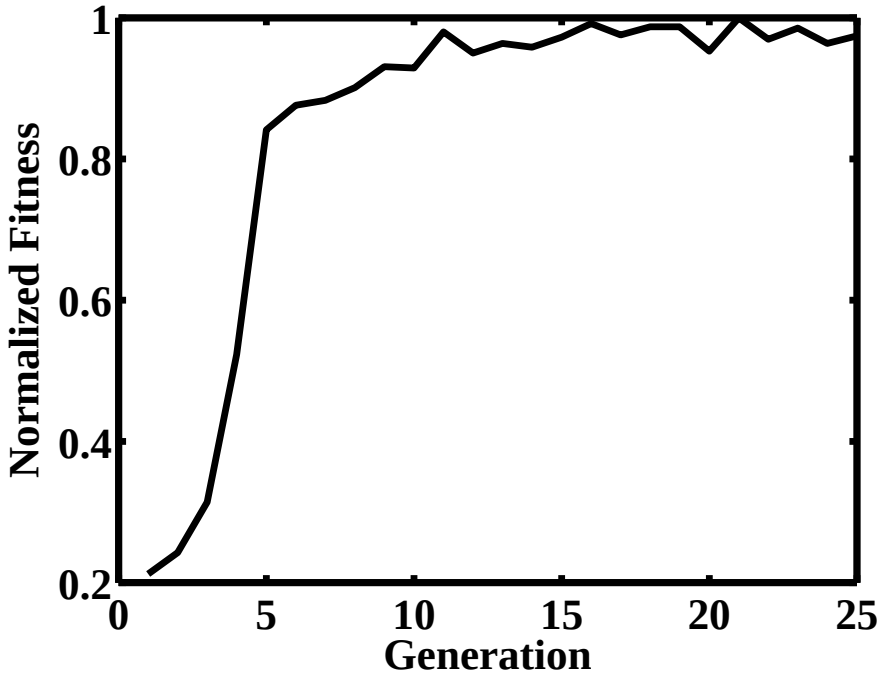

Figure 2.10 Fitness as a function of generation from a typical GA optimization.

down and eventually ends. This zero slope in the fitness curve is considered to be a convergence on an optimal solution. It is at this point that we stop the optimization process.

All of the GA parameters that are implemented in our genetic algorithm are summarized in Appendix A.

Closed-loop learning control allows us to find optimal pulse shapes for controlling molecular fragmentation. However, we typically end up with a solution and have little idea about how this pulse shape interacted with the molecular system to yield control. In Chapter 3, we will talk about our efforts

in trying to develop methods to understand the optimal pulse shapes solutions found by the GA in the adaptive learning feedback loop.

Chapter 3

Methods for Understanding Closed-Loop Learning Control

As discussed in Chapter 1, we typically do not have sufficient information about the molecular Hamiltonian to *a priori* design an optimal electric field that controls a particular molecular reaction. To design such an electric field, we would have to solve the time dependent Schroedinger equation

$$i\hbar\frac{d\Psi(t)}{dt} = \hat{H}_{tot}\Psi(t) \tag{3.1}$$

where

$$\hat{H}_{tot} = \hat{H}_0 + \hat{H}_{int} \tag{3.2}$$

contains both the field free Hamiltonian, H_0, and the molecule-field interaction term,

$$\hat{H}_{int} = -\hat{\mu} \cdot E(t) \tag{3.3}$$

where $\hat{\mu}$ is the dipole moment operator. In polyatomic molecules, which have $3N$-5 degrees of freedom, obtaining information about H_0 can be difficult. Furthermore, the molecule-field term adds additional complexity because $\hat{H}_{int}$ can be as large as $\hat{H}_0$. In our case, the electric fields can exceed $5 \times 10^{10} V/m$, meaning that the molecule-field interaction term can include strong field effects such as Stark shifting of energy states [25, 26, 27]. In order to discover optimal control fields for control in these situations, we utilize the method of closed-loop learning control.

The idea of closed-loop learning control is to let the molecule guide the system, via feedback, toward the correct pulse shape [7]. In essence, we are using the molecule's "knowledge" of its own Hamiltonian to help us find the right pulse shape for control. This method requires no prior understanding of the molecular structure. Learning control is typically efficient at finding optimally shaped electric fields to control a particular reaction [7]. However, it does not readily yield information about the mechanism responsible for the control. One of the goals of this thesis is to take the solutions found using learning control and uncover information about the control mechanism.

To this end, we would like to develop methods that will help us to reverse engineer the optimal pulse shape solution. In this chapter, we will discuss different methods that we have used in an attempt to understand learning control solutions found in experiments performed on molecular systems in our laboratory.

3.1 Cost Functional

Once an optimal electric field is found to control a particular reaction, we would like to understand how the shaped electric field interacts with the molecule to yield control. A starting point for understanding the laser-molecule interaction is to assess which pulse features are necessary for control. That is, we would like to separate the necessary from the merely sufficient features responsible for controlling the reaction. Sufficient but unnecessary features in an optimal pulse shape add unwanted complexity to the overall goal of understanding the control mechanism. We eliminate these unnecessary features by using a cost functional [28]. The cost functional pressures solutions toward a selected bias solution. In our case, the bias solution is a reference pulse shape. This reference can be any shaped pulse. In the experiments discussed in this thesis, the reference was always an unshaped, transform limited pulse.

In Chapter 2 we discussed how the GA controls the phase, $\phi(\omega)$, of the

ultrafast laser pulse. It does this by creating a vector of gene values that encode the spectral phase. It then measures the pulse shape fitness, or how well the pulse shape performed with respect to a given goal. Using the cost functional, we would like to achieve similar fitness values for pulse shapes that only have features that are necessary for optimally controlling a given molecular reaction. Mathematically, the cost functional is represented as

$$\zeta = W \sum_{i=1}^{N} (x_{oi} - x_i)^p, \tag{3.4}$$

where x_{oi} is the ith gene value of the reference pulse shape, x_i is the ith gene value of the pulse being shaped, N is the number of genes, W is a weight (which is determined empirically), and p is chosen to be between 0.25 and 2. The choice of p is discussed in more detail below.

The cost functional is then subtracted from the original fitness,F, of each pulse shape, resulting in a new fitness F',

$$F' = F - \zeta, \tag{3.5}$$

By inspecting Eq. 3.5, one can see that any deviation from the reference results in a decreased fitness. The cost functional acts to *penalize* differences in the pulse shape that deviate from the reference pulse shape. The cost functional

was found to work best if the fitness F' went to $\sim$ 95% of the fitness, F, found without the cost functional. In this regime, the cost functional does not prevent the GA from converging, but it is able to suppress unnecessary genetic variations from the reference.

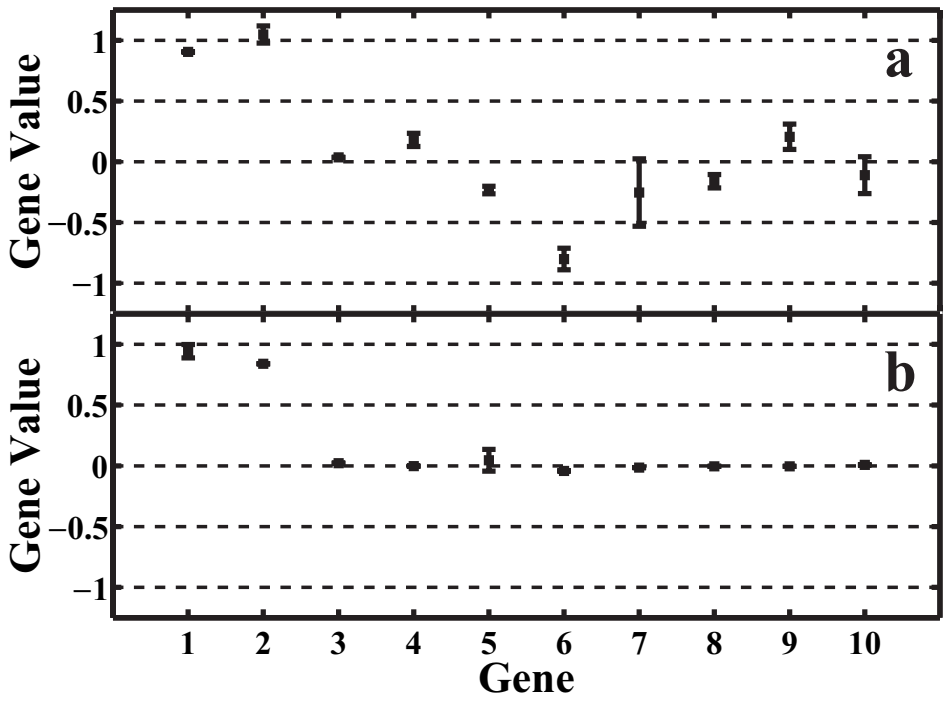

Figure 3.1 Results of simulated GA optimization on a two-dimensional problem, Eq. 3.6, using 20 genes. The values are the averages of each gene from all pulse shapes of the last generation. The vertical bars represent the standard deviation of those gene values. (a) Without the cost functional (b) with the cost functional. Note that the optimization without the cost functional produces non-zero values for genes known to be unimportant. [29].

One way to test the effectiveness of the cost functional is to start with a simple toy problem. Fig. 3.1 shows the average gene values and the standard deviation (vertical bars) of those values from ten pulse shapes from the last

generation of two GA optimizations on the function

$$F(x_1, x_2) = \mathrm{e}^{-(x_1-1)^2-(x_2-1)^2}, \tag{3.6}$$

using twenty genes a) without a cost functional and b) with a cost functional (with $p = 0.25$) [29, 30]. This function is specifically designed to be two-dimensional, so that the solution only depends on genes x_1 and x_2. Because values for genes x_3-x_{20} are not needed to optimize Eq. 3.6, we would expect that their gene values will have large standard deviations around zero value since their values do not affect F. This expectation is based on the fact that the gene values for each gene are randomly selected around an unshaped pulse at the beginning of the GA optimization. Fig. 3.1(a) demonstrates that our expectations are not borne out. It shows that the GA finds solutions containing large values and small standard deviations for genes x_3-x_{20}, despite the fact that these genes are unimportant for optimization of the fitness. It is evident that the GA is carrying values for these unimportant genes from one generation to the next, which would make it impossible to separate the necessary from sufficient gene values by employing a method using only the standard deviation of the gene values.

Fig. 3.1(b) shows that the cost functional helps to eliminate this problem.

The absolute values of genes x_3-x_{20} are near zero (which are the values of the reference pulse) after convergence when the cost functional is utilized. Note that the the solutions found by the GA with the cost functional applied do not exactly have the expected values for genes x_1 and x_2 ($x_1 = x_2 = 1$) but are have slightly smaller values. This is because the cost functional modifies the fitness landscape by pressuring the solutions toward the reference. It introduces a gradient in all dimensions of the fitness landscape pointing towards the reference fitness. One has to be careful to choose a weight, W, for the cost functional that allows it to restrict unnecessary deviations from the reference pulse shape while not overly distorting the fitness space. It was found that noise in the problem was also a factor in determining the size of the weight factor. Smaller noise values in the problem allow for a smaller weight of the cost functional.

The nature of the gradient in the direction of the reference is determined by the parameter p. Low values (e.g. $p = 0.25$) put more pressure on small gene values, i.e., there is a larger fitness increase for decreasing small gene values than for decreasing large gene values by the same amount. High values (e.g. $p = 2$) put more pressure on large gene values, i.e., there is a larger fitness increase for decreasing large gene values than for decreasing small gene values by the same amount. Of course, the deviation from zero is not always

a good measure for the importance of a gene. Small gene values can also be important for control (i.e., changing their value to zero can significantly reduce the fitness). Determining the number of important parameters required for a solution means setting some threshold value for small gene values to be considered insignificant. After setting such a threshold, one has to justify the choice by checking whether an individual with all gene values that are smaller than the threshold set to exactly 0 still yields a fitness of at least 95% of its original fitness. We performed this check for all of our control results. While it is possible to consider the effect of genes on many attributes of solutions such as robustness and efficiency, we determine the importance of particular genes based solely on the fitness here.

By adding the cost functional to our learning algorithm, we are able to find which genes are important (with respect to the bias solution) for control. In the case of our simple problem, we were able to reduce the dimensionality of the solutions to the required number of parameters. Having fewer number of parameters helps in the interpretation of the control mechanism, as we can systematically scan a small number of parameters around their optimal values.

3.2 Changing Basis-Control in Trifluoroacetone

In addition to using the optimal pulse shape as a guide to understanding the control mechanism, we would like to know whether or not we can learn something else from the learning algorithm solutions. [16, 31]. That is, we would like to take the gene values that the GA uses to encode the phase and infer physical properties of the atomic or molecular system that we are studying. Systematic scans of gene values can lead to information about the molecular Hamiltonian. The gene values are variables that make up a vector in the fitness space. Mathematically, encoding of the spectral phase, $\phi(\omega)$ can be expressed as

$$\phi(\omega) = \sum_{n=1}^{N} x_n G_n(\omega), \tag{3.7}$$

where x_n are the gene values and G_n are the genes. One way to learn something about the fitness space would be to systematically scan the values x_n for all G_n's. This would form a "picture" of the fitness space. However, in our experiments, we typically set $N = 20$. This high dimensionality makes it experimentally difficult to perform a systematic scan of all gene values.

Before performing any systematic gene value scans of the fitness space, we would like to know whether or not our pulse shapes are represented in the best possible basis. We define the best possible basis as being a diagonal basis,

where each of the genes are orthogonal and uncoupled and can fully represent the fitness space in the fewest number of genes.

Reducing the control problem to as few independent genes as possible requires a transformation to a new basis. Of special interest is the identification of a transformation to a nearly diagonal basis, where there is minimal coupling between the newly defined genes. For the purposes of this thesis, we will define two genes to be uncoupled when the dependence of the overall optimization process on one is independent from the other. This corresponds to a physical fitness function F that can be written as a sum of one dimensional functions,

$$F(x_1, x_2...x_N) = \Sigma_n f_n(x_n). \tag{3.8}$$

If the function is in the form of a product of one dimensional functions,

$$F(x_1, x_2...x_N) = \Pi_n f_n(x_n), \tag{3.9}$$

one can simply take the logarithm of F to produce a sum of one dimensional functions. In molecular learning control experiments, F is typically the ratio of the fragment ion yields in competing dissociative ionization channels. The function F depends on the shaped electric field, $E(\omega)$, which is constrained to just depend on spectral phase. The transformations we would like to make are

between different bases G_n. The expression in Eq. (3.7) may be identified as a scalar product $\mathbf{x^T} \cdot \mathbf{G}(\omega)$, and a linear transformation to a new basis can be written as $\mathbf{G'}(\omega) = \mathbf{\Omega} \cdot \mathbf{G}(\omega)$ and $\mathbf{x'} = \mathbf{\Omega} \cdot \mathbf{x}$, with $\mathbf{\Omega}$ being a constant unitary matrix. The question addressed here is whether a transformation $\mathbf{\Omega}$ can be found such that $\mathbf{G'}$ is a "good" basis to describe the fitness function $F(\mathbf{x'})$ over a relevant global search space domain of $\mathbf{x'}$.

We would like to apply the idea of basis changing to the process of trying to understand the solutions that learning control yields in molecular fragmentation experiments. We want to be able to find an optimal basis to encode our genes so that the genes are 1) uncoupled and 2) that the solution can be represented in the minimal number of genes possible. So we ask the question: Can we apply the idea of basis transformation to the problem of understanding learning control of molecular dynamics?

To test whether or not changing basis would work on an experimental system, we performed learning control experiments on triflouroacetone (CH_3COCF_3, TFA), which is shown in ball and stick representation in Figure 3.2.

In these learning control experiments, we tried to enhance the breaking of the $C - CF_3$ bond over the $C - CH_3$ bond. Our goal was to increase the CF_3^+/CH_3^+ ratio. The reaction that we were trying to control is illustrated in Figure 3.3.

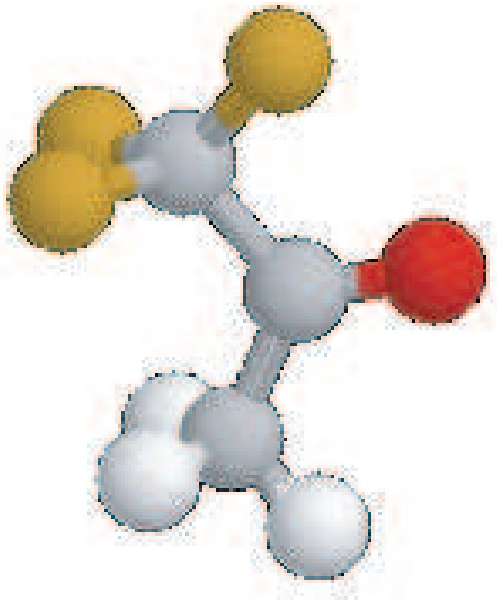

Figure 3.2 Ball and Stick figure of trifluoroacetone.

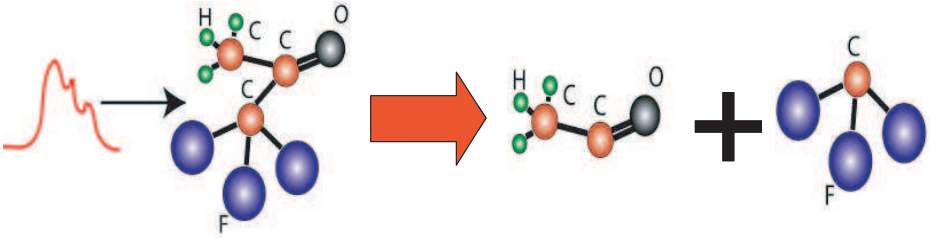

Figure 3.3 Cartoon of bond-breaking reaction that we were trying to control in TFA.

These experiments were successful at controlling the methyl ratios. A detailed discussion of the results for these learning control experiments is presented in Chapter 4. Figure 3.4 shows the $I(t)$ for an optimal pulse found to optimize the CF_3^+/CH_3^+ ratio. The optimal pulses for producing CF_3^+ were

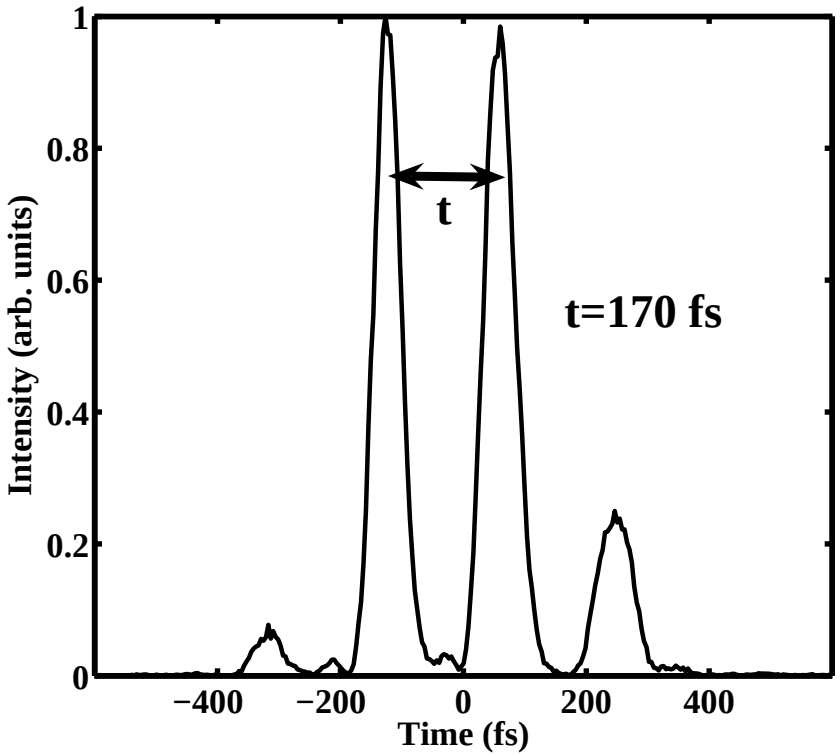

Figure 3.4 $I(t)$ of the optimal pulse. The time dependence between the two main intensity structures was found to be $\sim$ 170 fs for many different GA optimizations.

discovered by the GA while searching the solution space using a straightforward basis in which each of the 20 genes coded for the spectral phase at 20 different frequencies within the bandwidth of the laser pulse. The spectral

phase was interpolated between these 20 frequencies

$$\phi(\omega) = \sum_j x_j H(\omega - \omega_j), \tag{3.10}$$

with $H(\omega - \omega_j)$ being a smooth (continuous and differentiable) approximation to the Heaviside step function. This basis set is essentially the derivative of the simple, often used basis where the spectral phase is interpolated from a set of discretely sampled points. The derivative helps ensure that meaningless phase differences over 2π do not complicate the analysis and that trivial couplings between basis vectors are avoided. The periodic structure of the pulse shape solutions, such as that shown in Fig. 3.4, found by the GA suggest that a better basis for solving problems that involve matching periodic motion should be one that allows each gene to code for a separate periodicity. For this we make use of a Fourier Phase Modulation (FPM) basis [32] that expresses the spectral phase as

$$\phi(\omega) = \sum_i x_i \cos(k_i \omega), \tag{3.11}$$

where the frequency, k_i, is

$$k_i = \frac{2\pi i}{\Delta\omega}, \tag{3.12}$$

where $\Delta\omega = 2\pi\Delta\nu = 2\pi \cdot 24$ THz is optical bandwidth of our pulse shaper.

Note that going from the basis in Eq. 3.10 to Eq. 3.11 requires a nonlinear transformation of variables because we are using a finite sum. It is obvious from Eq. 3.11 that this is not the case.

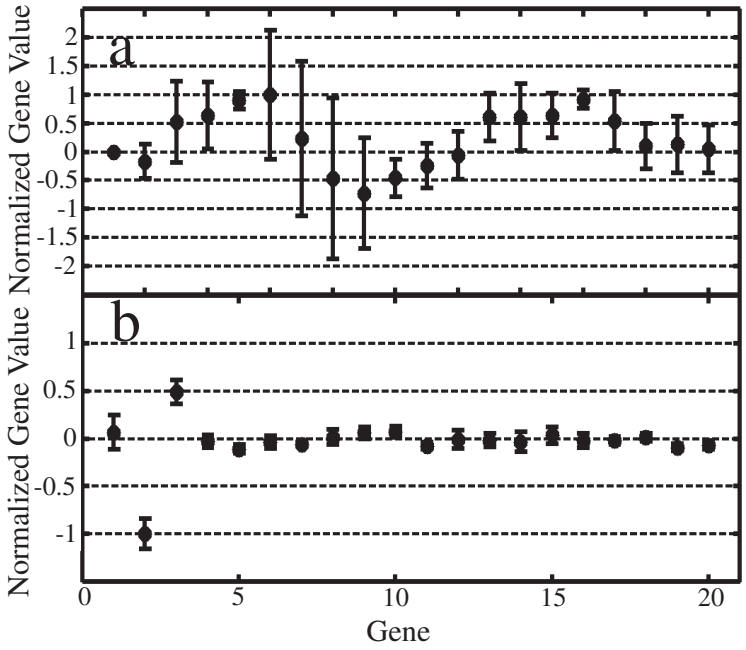

Figure 3.5 Average of the five fittest solutions from mulitple GA optimizations performed in (a) the difference basis and (b) the FPM basis. The vertical bars represent the standard deviation of the gene values.

Figs. 3.5(a) and 3.5(b) show the genetic code for pulses optimized in the two bases. In Fig. 3.5(a), the genetic code represented was found with the GA that encoded the genes in the original phase difference basis. Fig. 3.5(b) shows the genetic code found by the GA in which the genes were encoded in the FPM basis. Both data sets were taken with the cost functional actively

suppressing unnecessary differences from an unshaped pulse. The genetic code for each data set represents an average of the fittest five pulses from multiple GA runs. The vertical bars in these figures represent the standard deviation of gene values over solutions from multiple optimizations. It can be seen from these bars that the solutions in the original basis varied significantly from each other. However, the gene values found using the FPM basis have very small vertical bars, indicating that the different GA optimizations found very similar results.

The number of genes with values that differed substantially from zero for the FPM basis is far less than for the original basis. We found that the number of genes with important values for control scaled with the number of genes for the original basis, but it did not scale for the FPM basis. The reduction in the number of important genes as shown in Fig. 3.5 suggests that the dimensionality of the problem was reduced to ~ 2 when the GA was allowed to search using the more intuitive basis. To ensure that the gene values in genes x_1 and x_4-x_{20} were not necessary, we programmed a pulse onto the pulse shaper with those gene values set to zero. The resulting pulse shape yielded a TOFM spectrum with a fitness of over 95% of the original fitness, indicating that the genes with near zero value in the FPM basis were not important. This was done for all of the solutions found in this basis, and was

found to work for all of the solutions. We also tried setting the lowest 13 out of 20 genes for the solutions in Fig. 3.5(a) to zero but this resulted in a lowering of the fitness to around 65% of the optimal pulse fitness. This confirms that the dimensionality of the problem is significantly higher in the original basis.

As a test to see whether or not we were successful at decoupling the fitness space we decided to examine the relationship between a pair of genes in both the phase difference and FPM basis as we scanned their possible gene values. Fig. 3.6 shows the CF_3^+/CH_3^+ ratio as a function of gene value for basis function genes x_9 and x_{10} in the phase difference basis and genes x_2 and x_5 in the FPM basis.

Fig. 3.6(a) shows that there is an obvious coupling between the two genes x_9 and x_{10}. If it were not for the modulations of the diagonal ridges in the figure, a 45° rotation of the axes would essentially diagonalize this two-dimensional subspace. The presence of these modulations requires a nonlinear transformation to decouple the dependence of the fitness function with respect to the two basis functions. On the other hand, Fig. 3.6(b) shows that the FPM basis results in almost no coupling between the two genes. This subspace shows that the basis transformation helped to eliminate coupling between these two genes.

We also note also that the depth of modulation in the landscape (i.e.,

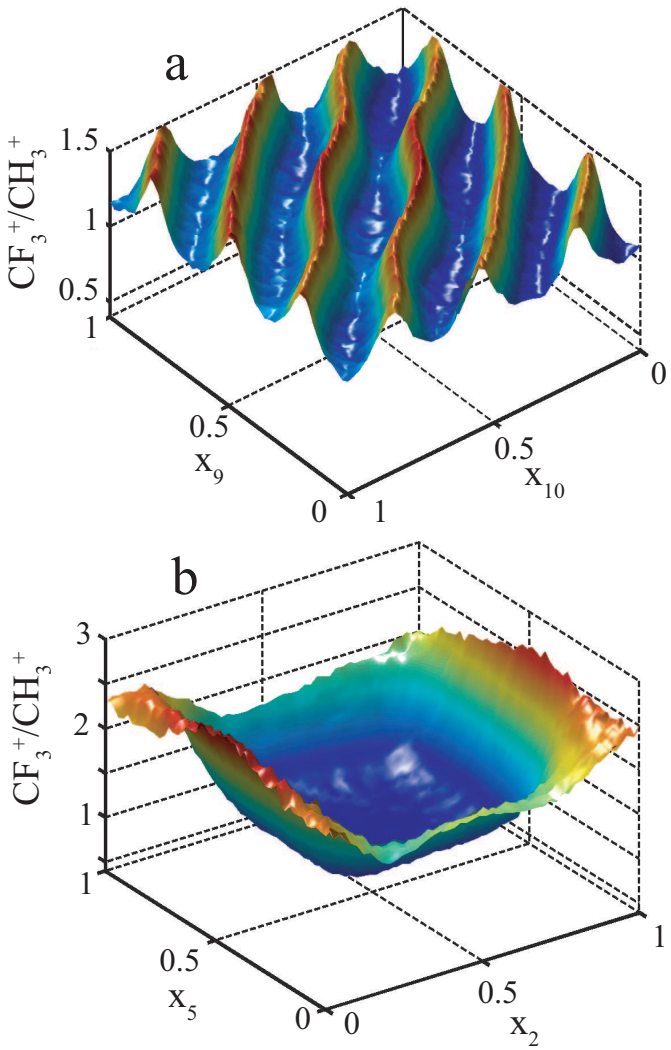

Figure 3.6 (a) The CF_3^+/CH_3^+ ratio as a function of basis function coefficients 9 and 10 in the differential phase basis. (b) The CF_3^+/CH_3^+ ratio as a function of basis function coefficients 2 and 5 in the FPM basis.

the difference between the fitness extrema) of Fig. 3.6(b) is larger than in Fig. 3.6(a), indicating that these two FPM genes are more effective in controlling the CF_3^+/CH_3^+ ratio while acting independently.

The original basis and the FPM basis represent two different approaches

to constructing and interpreting solutions to optimal control problems. This parallels two paradigms for coherent control, with the original phase difference basis following a frequency domain approach, and the FPM basis following a wave packet or time domain approach [3, 33]. We argue that a natural basis for problems that involve wave packet oscillations (with possibly many frequency components) is a basis such as the FPM basis that allows for encoding the temporal periodicity with a minimum number of genes.

The transformation to the FPM basis was made by making an educated guess after analysis of the data taken in the phase difference basis. However, we would like to develop systematic methods for finding new bases. Before we do this, we have to address the important question of whether the transformation to a new basis is linear or nonlinear. In cases where a linear transformation is satisfactory, there are techniques that can be employed to identify the appropriate transformation [34]. In the case of problems where a nonlinear transformation is required, it is still an open question of how one can discover the right transformation. In the case discussed above, the transformation ended up having to be nonlinear. However, it would be better to have methods that test whether or not a nonlinear basis transformation is necessary, or if a simple linear transformation can effectively diagonalize the fitness space. In order to determine whether or not a linear transformation can separate the optimiza-

tion problem into N one-dimensional problems, as in Eq. 3.8, we construct the Hessian matrix, $\mathbf{A}$, whose elements are given by

$$A_{ij} = \partial_i \partial_j F, \tag{3.13}$$

where $\partial_i = \frac{\partial}{\partial x_i}$. If $\mathbf{A}$ is diagonal everywhere in the control search space for all $\mathbf{x}$, then F is separable. If $\mathbf{A}$ is not diagonal, the question becomes whether there is a linear transformation *independent of position* $\mathbf{x}$ that can diagonalize $\mathbf{A}$. If we consider two points in the phase space, $\mathbf{x_i}$ and $\mathbf{x_j}$, then the same linear transformation $\mathbf{\Omega}$ can diagonalize $\mathbf{A}$ at these two points if

$$[\mathbf{A}(\mathbf{x_i}), \mathbf{A}(\mathbf{x_j})] = 0. \tag{3.14}$$

If Eq. (3.14) is satisfied for all points $\mathbf{x_i}$ and $\mathbf{x_j}$ in the physically significant control domain, then a linear transformation can reduce the original N-dimensional optimization problem to a series of N one-dimensional problems. Establishing the existence of a global transformation would imply that the control problem in that domain is fully described by the identified separable variables.

To illustrate the basic formalism presented above, we consider two separate

two-dimensional fitness functions:

$$F_1(x, y) = x^2 + y^2 + xy \tag{3.15}$$

and

$$F_2(x, y) = x^2 + y^2 + xy^2. \tag{3.16}$$

As the Hessian for F_1,

$$\mathbf{A_1} = \begin{pmatrix} 2 & 1 \\ 1 & 2 \end{pmatrix}, \tag{3.17}$$

is constant (i.e., independent of the variable x), it is obvious that the commutator of the Hessian evaluated at any two different locations will always be zero. For F_2, the Hessian matrix is

$$\mathbf{A_2} = \begin{pmatrix} 2 & 2y \\ 2y & 2 + 2x \end{pmatrix}. \tag{3.18}$$

The commutator for this matrix evaluated at two different locations will in general not be zero. A linear transformation can diagonalize the Hessian for F_1 but not for F_2. These two functions are both simple and analytical. However, there is typically no *a priori* analytical expression available for the fitness function over the control variables in molecular fragmentation experiments, so

we have to use experimental data to test Eq. 3.14.

We performed the experimental test of the formalism by applying Eq. 3.14 to the two, two-dimensional subspaces that are shown in Fig. 3.6. To do this, we calculated the Hessian matrix at the center of each subspace. Then we calculated Hessian matrices at points along the direction of each of the diagonals, which are illustrated by the white arrowed lines in Figure 3.7. We then took the commutators between each one of the Hessians along the diagonals and the center Hessian matrix. As a measure of how well each of the Hessian matrices commuted with the center, we took the spectral norms of both the commutators and the Hessian matrices,

$$\frac{||C||}{||A||} = \frac{\sqrt{maximum\ eigenvalue\ of\ C^H C}}{\sqrt{maximum\ eigenvalue\ of\ A^H A}} \tag{3.19}$$

where C is the commutator matrix and the superscript H indicates that the conjugate transpose is taken.

Fig. 3.8 plots the average of the spectral norm ratios from all of the points taken in all directions for both the phase difference and the FPM basis.

The solid line corresponds to the analysis for the phase difference basis and the dotted line corresponds to the analysis for the FPM basis. Note that the ratios of the spectral norms are larger for the phase difference basis than for

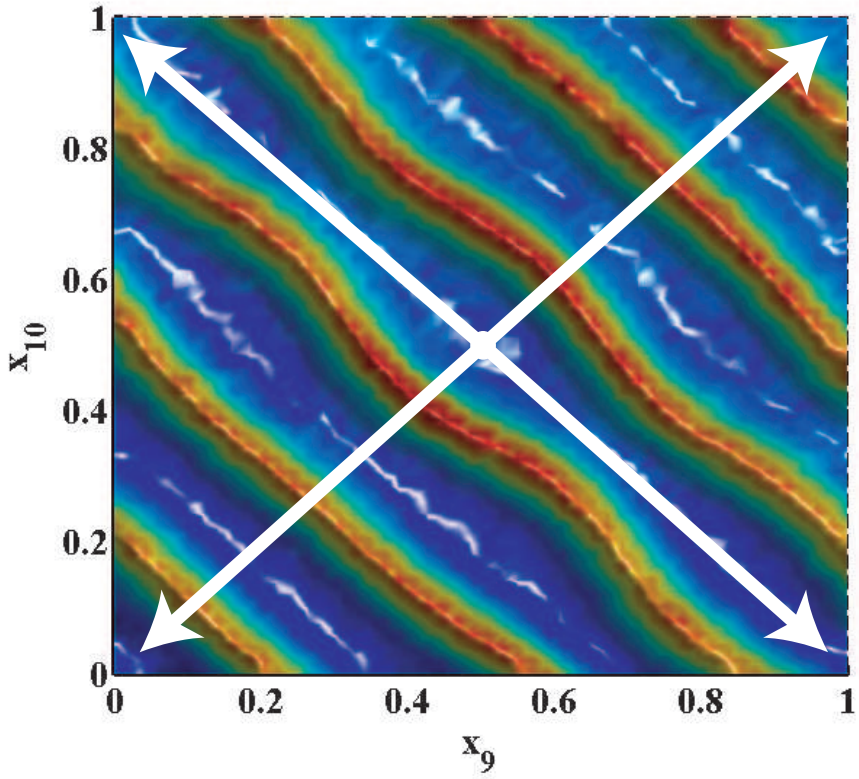

Figure 3.7 Hessian matrix was calculated at center of both the phase difference subspace and the FPM subspace. Then Hessians were calculated along the directions indicated by the arrows. The commutators of these Hessians with the center were then taken.

the FPM basis. This is consistent with the intuitive picture gained from the surface plots where the nonlinear coupling was evident in Fig. 3.6(a). The large decrease in the spectral norms for the FPM basis illustrates the effectiveness of this basis in decreasing the coupling between the control variables. No linear transformation from the difference basis would be capable of reducing the coupling, as compared to making a nonlinear transformation to the FPM basis.

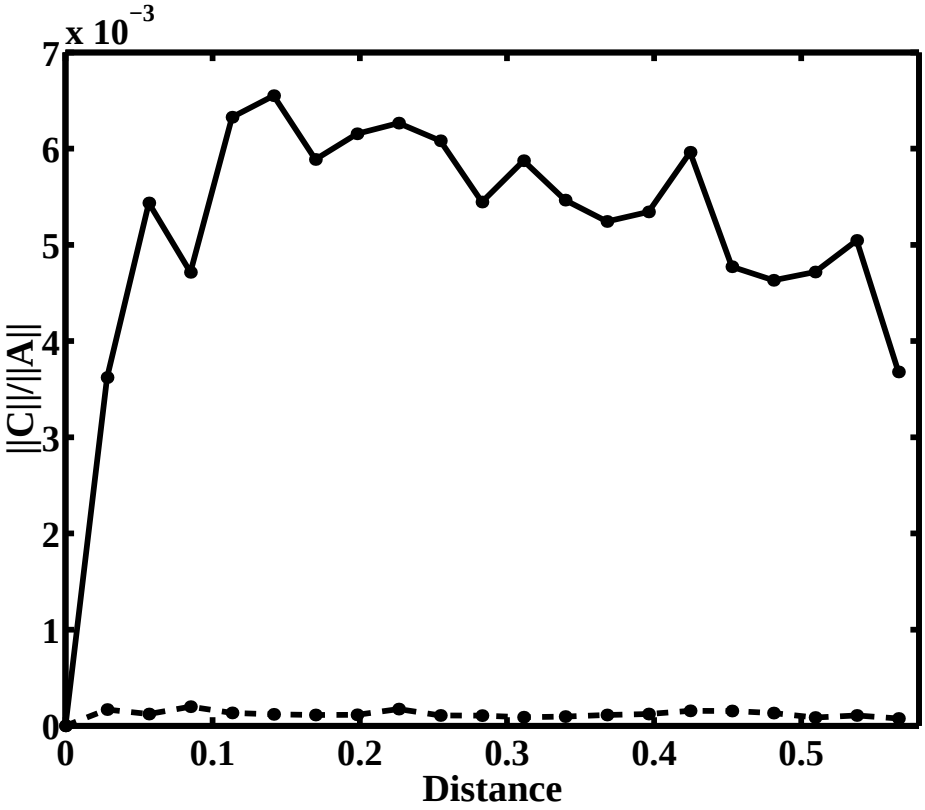

Figure 3.8 The ratio of the spectral norms for Hessian analysis of the subspace shown in Fig. 3.6(a) taken in the phase difference basis (solid line) and for the subspace taken in the FPM basis (dotted line) shown in Fig. 3.6b (dotted line).

The discovery of a basis in which a problem is separable is an important aspect of understanding learning control problems and their solutions. The use of a cost functional in the search algorithm in our GA allowed us to pick out the essential elements of our solutions. This led to the choice of a new basis that reduced the number of genes needed to parameterize the fitness space. This allowed us to perform systematic scans along these important fitness space dimensions.

In general, one would ideally like to discover an ideal basis in which the dimensionality of the problem is reduced in some automated fashion. What we have shown here is that it is possible to find such bases and quantitatively measure the difference between them. We would like to build a library of known bases that correspond to different types of control mechanisms, such as the FPM basis in the event that wave packet timing is essential for control. We could then do automated searches through our library of preexisting bases. Finding an optimal basis set in our library would then yield useful clues about the mechanism responsible for control.

We have already demonstrated this for another molecule, CH_2BrI, where control over the CH_2I^+/CH_2Br^+ showed pulse shapes that appeared to have large amounts linear chirp across the laser pulse spectrum. Using this knowledge, we created a polynomial basis that encoded each gene as a coefficient in polynomial expansion. Solutions to the control experiments in this basis showed that the gene responsible for second order phase was the only active gene [29]. In this case, we had to make another nonlinear basis transformation. It may be the case that nonlinear transformations will be needed in general to globally diagonalize fitness spaces. We have not found any molecular cases where the fitness space has been diagonalizable by a linear transformation.

The change of basis discussed here has allowed us to perform scans which

will help us in our attempt to develop an understanding of the learning control seen in TFA. By being able to perform scans such as those shown in Fig. 3.6 we can develop some insight into how the fitness landscape looks. Similarly, by performing other parameter scans, such as pump-probe scans, we can hope to learn something about the specific molecular processes responsible for the control. We will use the knowledge acquired here to discuss mechanistic properties of the control in the next chapter. It will become apparent that the change of basis to the FPM basis will allow us to choose other parameter scans that will ultimately lead us to a better understanding of the control mechanism.

Chapter 4

Understanding the Control Mechanism in Trifluoroacetone

As discussed in Chapter 3, the goal of our learning control experiments in trifluoroacetone was to maximize the CF_3^+/CH_3^+ ratio [12].

Results from a learning control experiment are shown in Fig. 4.1, which shows two TOFM spectra. The top spectrum was obtained using an optimal pulse shape found by the learning control apparatus. The bottom spectrum was obtained using an unshaped, near transform limited pulse. The intensity and phase of the optimal pulse shape are shown in Figure 4.2. The inset in Fig. 4.2 shows the CF_3^+/CH_3^+ ratio as a function of generation for the GA optimization that found this optimal pulse shape. Note that the shaped pulse lead to an increase in the absolute CF_3^+ yield as well as a decrease in the absolute CH_3^+ yield. Correlated with the increased CF_3^+ yield is an increase

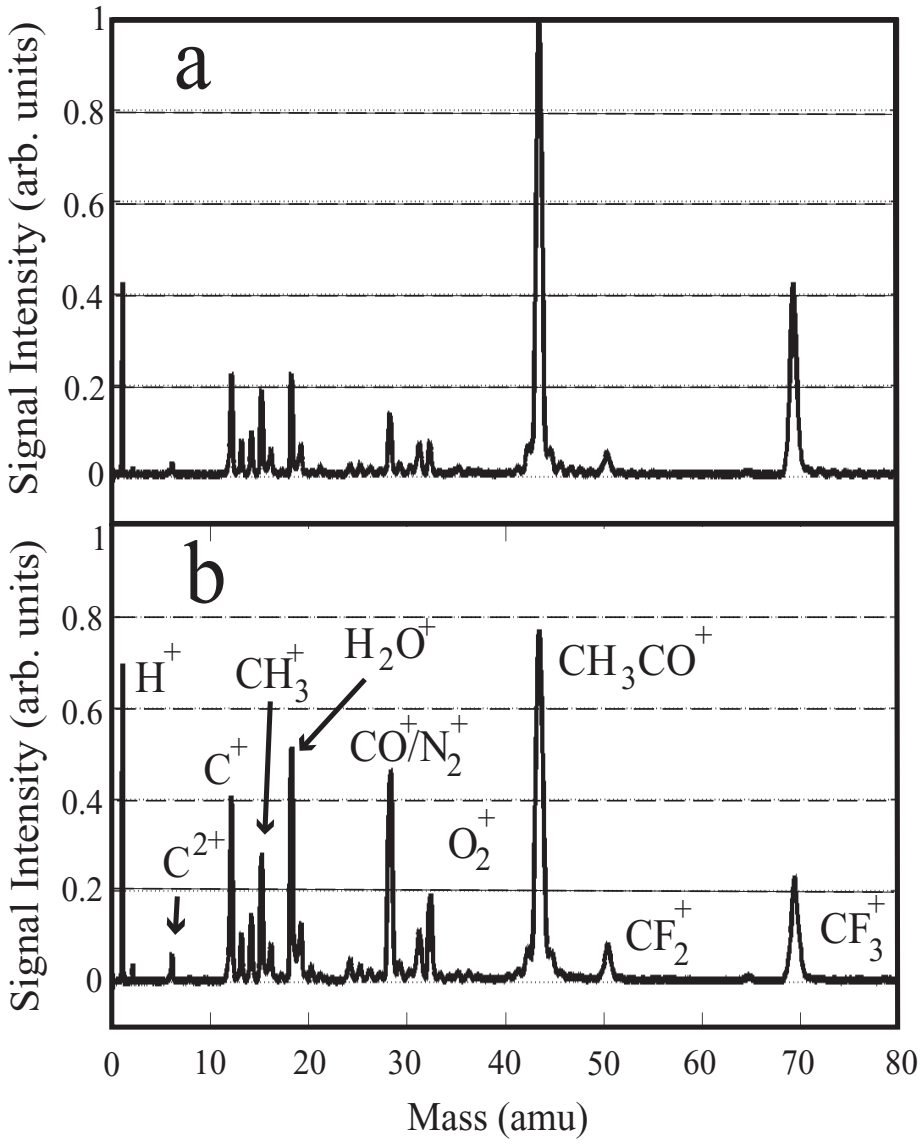

Figure 4.1 (a) Trifluoroacetone spectrum obtained with an optimally shaped laser pulse. (b) Spectrum obtained with an unshaped pulse on the pulse shaper. N_2^+, O_2^+, H_2O^+, and the other unlabeled peaks are background peaks seen prior to the introduction of trifluoroacetone into our apparatus. Note that both spectra are plotted on the same absolute scale so that peak heights may be compared.

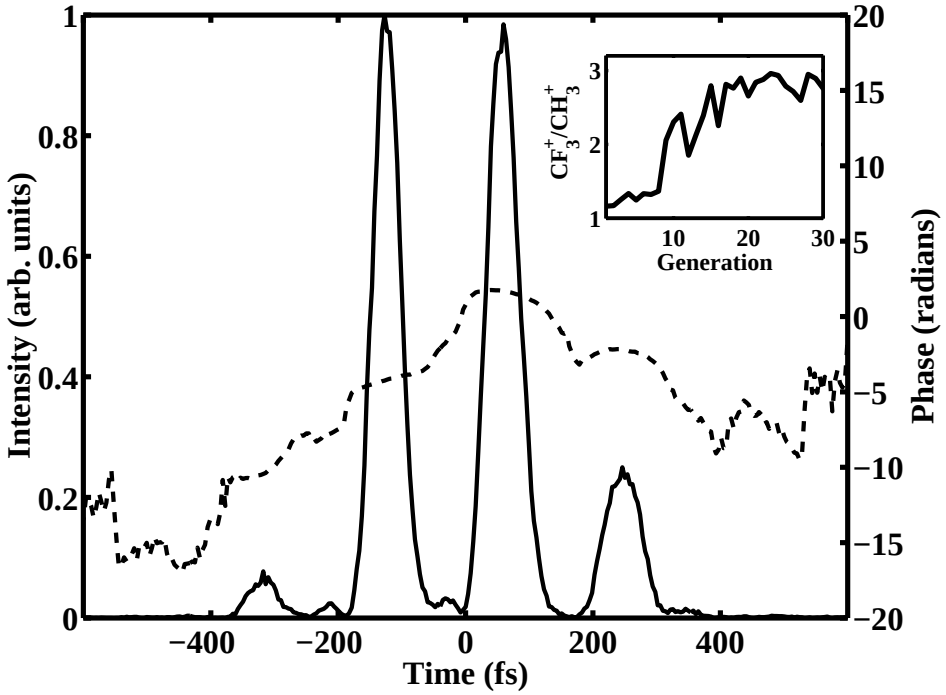

Figure 4.2 Optimal $I(t)$ and phase for pulse found to enhance the production of CF_3^+ while reducing the production of CH_3^+. The inset is the CF_3^+/CH_3^+ ratio yield as a function of generation for the optimization.

in the CH_3CO^+ yield. The other peaks in the spectrum decreased. Many runs of the GA with random initial pulse shapes yielded similar TOFM spectra. In Fig. 4.1, the CF_3^+/CH_3^+ ratio was 1.2 with an unshaped pulse programmed on the AOM. With the solution found by the GA, the ratio went to 3.0. Other experiments were performed with the control goal of producing CH_3^+ while suppressing the production of CF_3^+ as well. We were able to drive the ratio of CH_3^+/CF_3^+ to 0.6. We ran the GA with both goals at various intensities. We found that the optimal solution for producing CH_3^+ is a low energy pulse that

is nearly transform limited. The energy of the pulse for this goal was 65μJ. The energy of the pulses that produced the spectra in Fig. 4.1 is 165μJ. To ensure that intensity variation alone cannot be responsible for the control, we studied the TOFMS as a function of intensity. The CF_3^+/CH_3^+ ratio did not exceed 1.2 in a simple intensity scan.

Two important observations from our learning control experiments are the persistent absence of the parent ion in the TOFMS and the fact that the pulse shape that maximizes CF_3^+/CH_3^+ is a sequence of pulses. Since the pulse shaper was limited to phase only modulation (in order to work at a fixed pulse energy and to limit the number of search parameters that the GA utilizes), it was unable to create a simple pulse pair in the time domain. We therefore concentrate on the separation between the two main pulses in the sequence for our interpretation, considering the other smaller pulses in the sequence a result of the pulse shaper constraints. The time between these two pulses was found to be 170 fs for many different GA optimizations. This temporal separation does not correspond to any known neutral vibrational frequencies.

These observations along with the knowledge gained from the transformation to the FPM basis motivated a methodical study of control with a pump-probe pulse pair and a series of calculations. In our experiments, ionization of TFA occurs within a fraction of the laser pulse duration (peak intensities

are up to 5×10^{14} W/cm^2 for an unshaped pulse). This assertion is consistent with our own measurements and those of others [35, 36, 37, 38].

Molecular structure calculations were also performed on TFA. These calculations were carried out using GAMESS [39] at the MP2/6-311++G(d) [40] level of theory. Initial examination of these calculations show that after ionization, the parent ion becomes unstable and undergoes dissociation into CH_3CO^+ and CF_3. Figure 4.3 shows the charge on the CF_3 as a function of the distance between the CH_3CO^+ and CF_3 fragments. This calculation indicates that the charge remains on the fluorinated methyl group as the parent ion dissociates. This result is not surprising, as fluorine is the most electronegative element in the periodic table, and the fluorine atoms on the CF_3 fragment attract the remaining unpaired electron after ionization most strongly. These results are also consistent with our experimental data, which shows a lack of $CF_3COCF_3^+$ signal in our TOFMS. Further evidence for the parent ion to dissociate into these fragments is that for low laser intensities, where multiple ionization is not possible, the only signal observed in the TOFMS is CH_3CO^+.

Since we know from our initial studies of the calculations that dissociation occurs along the $C - CF_3$ bond length, we construct a ground ionic potential energy surface (PES) along this coordinate, which is shown in Figure 4.4. This PES was created by stepping the $C - CF_3$ bond length and allowing all of the

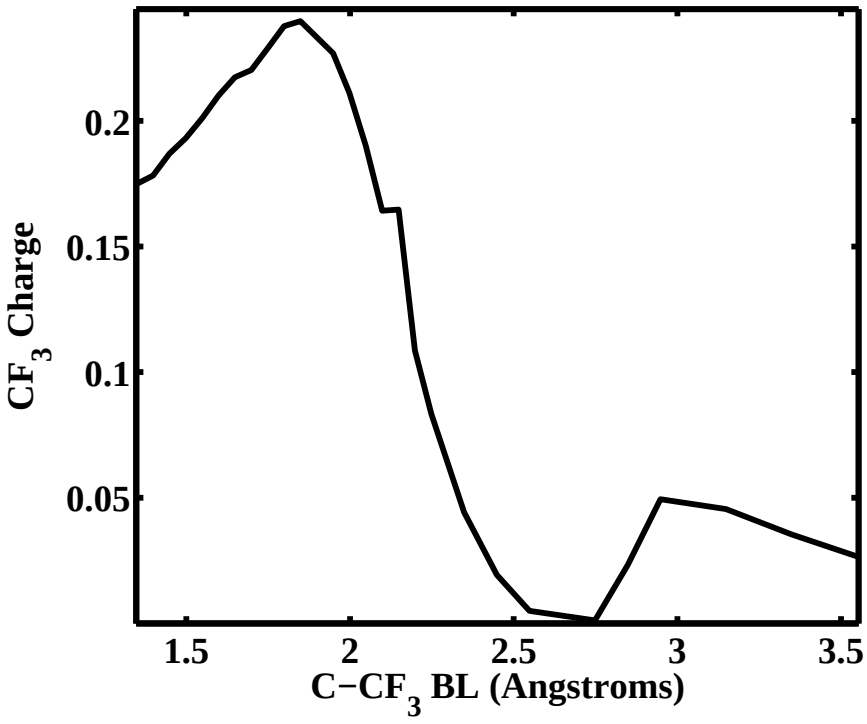

Figure 4.3 Positive charge on the CF_3 fragment as a function of $C-CF_3$ bond length.

other molecular degrees of freedom to relax, minimizing the energy. For this reason, we refer to this PES as the "relaxed" ionic PES. It is clear from Fig. 4.4 that TFA is unstable in the ground ionic state, and will dissociate.

While our calculations demonstrate that the parent ion is unstable and dissociates, others have predicted that there is a small barrier to dissociation in the geometry for the parent ion, but with the bond between CH_3CO^+ and CF_3 being too long and weak to play a role in these experiments [37]. Various density functional theory calculations performed by ourselves and others [41]

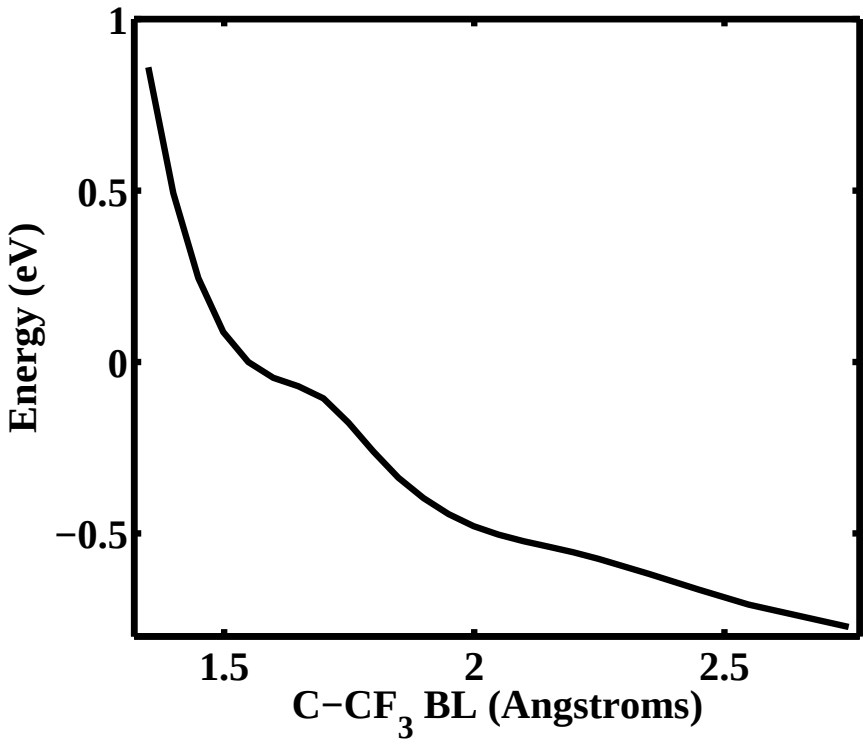

Figure 4.4 Ground ionic state PES for TFA as a function of $C - CF_3$ bond length. This was calculated by allowing all of the molecular degrees of freedom to relax at each $C-CF_3$ bond distance. It is clear that the PES is dissociative.

confirm that $CH_3COCF_3^+$ is, at most, marginally stable and forms CH_3CO^+ and CF_3 upon dissociation.

Thus, the first component of our model for the dynamics of the control mechanism is that the ionization of TFA leads to autodissociation into CH_3CO^+ and CF_3 fragments. This occurs during the first main pulse feature shown in Fig. 4.2. However, we have seen that the control doubled the CF_3^+ signal. Because we are only measuring cations in our experiments, and we have confirmed that $CH_3COCF_3^+$ dissociates into CH_3CO^+ and CF_3, the

control must be over the subsequent ionization of CF_3. Other mechanisms for controlling the charge on the CF_3 have been considered and rejected. Multiple ionization of TFA to produce CF_3^+ requires high laser intensities and, therefore, is much more efficient with an unshaped pulse. Another scenario would be charge transfer from the CH_3CO^+ fragment. This would create an anti-correlation between the CH_3CO^+ and CF_3^+ peaks in the TOFMS, which is not observed in the TOFMS taken with the optimal pulse (see Fig. 4.1 in Chapter 3). The question, then, is why the particular structure of the optimal control pulse is ideal for ionizing the CF_3 fragment.

To understand the periodic structure in the optimal control pulse we measured CF_3^+ and CH_3CO^+ yields as a function of delay between a pair of unshaped, 33 fs laser pulses. The results are shown in Figure 4.5. The ion yields are normalized to the maximum ion signal in each scan. Peak intensities for the pump and probe pulses were 2.2×10^{14} W/cm^2 and 1.2×10^{14} W/cm^2 respectively, comparable to (but not exactly the same as) the larger peaks in the optimal pulse shown in Figure 4.2. Our peak laser intensities were calibrated by measuring the ion yield as a function of laser intensity for benzene and finding the saturation intensity as described in [38] and resulted in an uncertainty of about 20%. TOFMS signals for both CF_3^+ and CH_3CO^+ as well as all other fragments showed a large increase when the pulses temporally

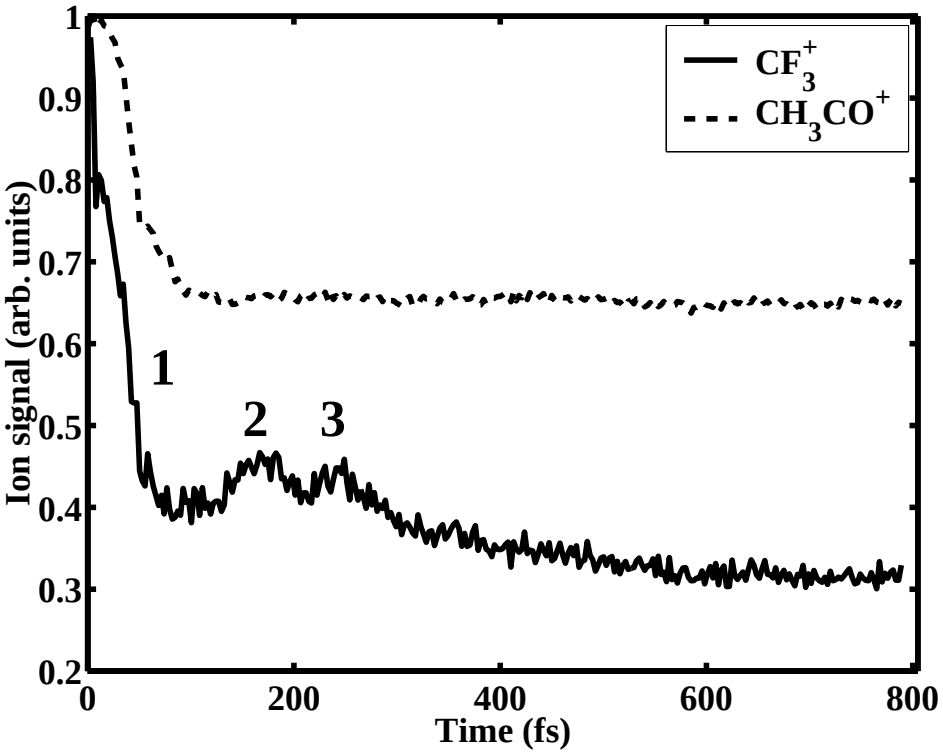

Figure 4.5 CF_3^+ and CH_3CO^+ yields as a function of pump-probe delay. Note that the time between ion yield enhancements 1 and 2 is 170 fs, which is the same as the time between the two large intensity structures seen in the optimal control pulse. Ion enhancement 1 is due to coherent optical effect of the two pulses being overlapped.

overlapped (peak 1 in Figure 4.5). Of greater interest to this control study are the modulations in CF_3^+ yield as a function of pump-probe delay (peaks 2 and 3). The spacing of peaks 1 and 2 match the spacing between subpulses in the optimal pulses discovered by the GA [14]. No other fragments yields showed significant modulations. In particular, note the lack of anti-correlation between the CH_3CO^+ and CF_3^+ fragments, which helps us to eliminate charge transfer between the two fragments as the mechanism for control. The heights

of peaks 2 and 3 in Fig. 4.5 were very sensitive to the laser pulse intensities of both the pump and probe. At higher pump and probe intensities, we saw that the height of the two peaks could be larger than the enhancement of peak 1, consistent with the fact that the GA found this time delay to be optimal for controlling the CF_3^+ yield.

Understanding the origin of the temporal structure in the pump-probe data is necessary for uncovering the control mechanism. A lack of phaselocking between the pump and probe pulses rules out electronic coherences as the source of the modulations in the CF_3^+ yield. This leaves the relative motion between the CH_3CO^+ and CF_3 fragments as the most likely source. The peaks in the pump-probe data when the pulses are separated suggests that there is an optimal CH_3CO^+ - CF_3 separation at which CF_3 ionization is enhanced. The pump-probe data, with the quasi-static molecular ionization calculations and the molecular structure calculations indicate that a nuclear wave packet is evolving on the ionic state PES shown in Fig. 4.4. At some point during this evolution, the wave packet has to move into a region where it can be excited to another PES where the CF_3 fragment is ionized.

Using this reasoning, we explored the idea of enhanced ionization being the reason for the enhancement in CF_3^+ yield [42, 43]. This model was developed for diatomic molecules, and then extended to triatomics, but there is every

indication that it applies, at least qualitatively, to larger molecular ions. The theory predicts that the ionization probability of a diatomic ion demonstrates non-monotonic behavior.

Figure 4.6 shows the same double well potentials for a diatomic molecule with (a) no field and (b)with a field. During every half-cycle of a laser pulse, the

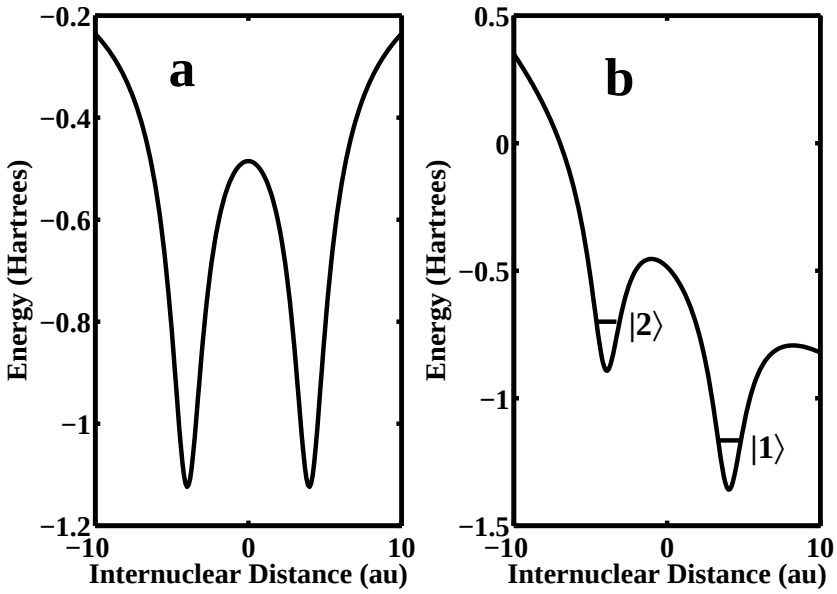

Figure 4.6 Same double well potential a) with a field and b)without a field.

double well potential will be suppressed, similar to what is seen if Fig. 4.6(b). This lowers the outer potential barrier, allowing electrons to tunnel through to the continuum. It can be seen from these plots that if the suppression of the outer barrier by the field is adiabatic, then one would see a monotonic increase in the ionization of the molecule as a function of internuclear separation as the

wavefunction would always settle to have more amplitude in the lowest energy state $|1\rangle$. This condition would occur if the laser frequency was less than the energy difference between states $|1\rangle$ and $|2\rangle$, i.e. $\omega_{laser} < \omega_{12}$. However, if $\omega_{laser} > \omega_{12}$, then wavefunction could be trapped in the upper state during every half cycle of the laser pulse. In this situation, the theory of enhanced ionization says that electric field of the ion itself and the laser electric field can create a superposed electric field, which under the right conditions could enhance the ionization probability from the upper state, $|2\rangle$, through the inner barrier and then over the outer barrier to the continuum. This is depicted in Figure 4.7. The ionization probability will be enhanced at some internuclear distance, R_0. This is because for long internuclear distances, the inner barrier between the two wells is large, which lowers the tunneling probability. At small internuclear distances, you have to consider the tunneling probability through the outer barrier as well. Therefore, the critical parameters for enhanced ionization are the internuclear distance, as this dictates how broad the inner barrier is and the strength of the electric field, which determines how the outer barrier is suppressed [42].

However, in the case of TFA we know from Fig. 4.3 that the unpaired electron will be localized on the CF_3 fragment. In this case, we do not need the dynamic localization of the wavefunction in the upper well which was

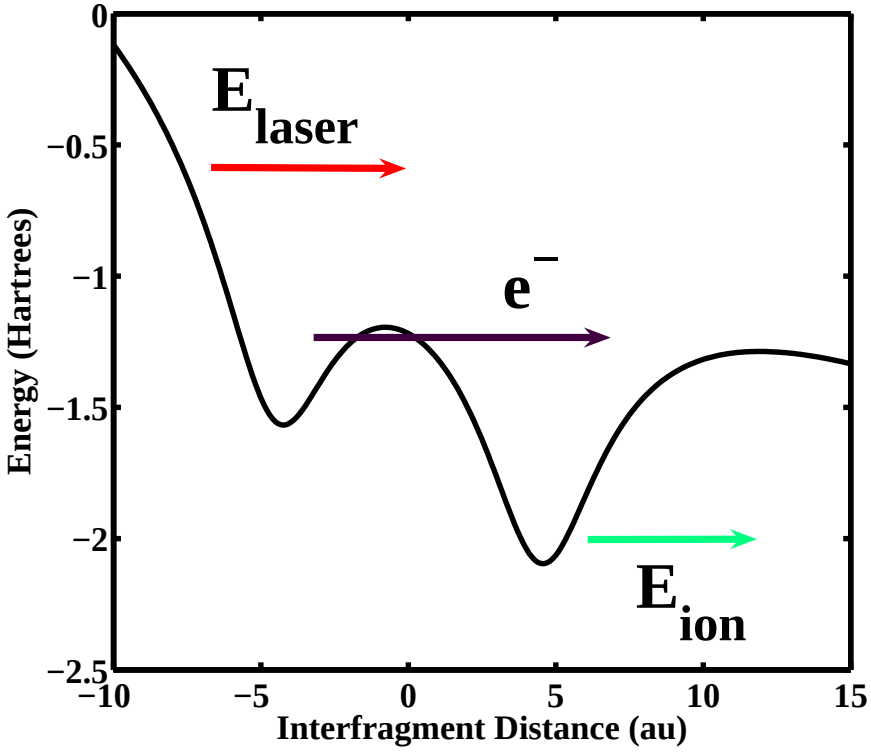

Figure 4.7 Illustration of enhanced ionization. The electric field of the laser adds with the field of the ion to create a superposed field that enhances the electron's probability of tunneling through the inner barrier to the continuum.

discussed above. So, if we assume that TFA is "diatomic" like, taking the CF_3 and CH_3CO^+ fragments to be "atomic" like, then we can use the enhanced ionization formalism to approximate what inter-fragment distance will give us an enhancement in the ionization probability of TFA.

Using the hypothesis that the theory of enhanced ionization explains the temporal features of both the optimally shaped pulse in Fig. 4.2 and in the pump-probe spectroscopy, we performed our own enhanced ionization calcula-

tions treating TFA like a "diatomic" molecule. The calculation was made by considering the quasi-static ionization rate from the CF_3 fragment, in two limits. The first limit is taken at large inter-fragment separations, and the second limit is taken at short inter-fragment distances [42]. For long inter-fragment distances, we calculate the ionization rate, $u_1(t)$, using molecular ADK theory [35, 36],

$$u_1(t) = u_{moadk}[IP_{CF_3}; E_{tot}; Q_{CF_3}] \tag{4.1}$$

where u_{moadk} is the molecular ADK calculation for ionization from the CF_3 fragment, IP is the ionization potential of the CF_3 fragment, and Q_1 is the charge of the CF_3 fragment, which is zero in our case. The ionization potentials that were used in this calculation come from the molecular structure calculations. The total electric field, E_{tot}, is expressed as

$$Etot = E|sin(\omega t)| + |E_{CH_3CO^+}| \tag{4.2}$$

which shows that the electric field of the ion and the electric field of the laser are acting in the same direction during a cycle of the laser pulse. However, because we have to consider the fact that $|E_{CH_3CO^+}|$ changes as a function of inter-fragment distance, we have to make a change to the second term in E_{tot} that accounts for this. To do this, we rewrite E_{tot} to be homogenous at the

maximum of the inner barrier,

$$E_{tot} = E|sin(\omega t)| + \frac{Q_{CH_3CO^+}}{(R - R_0)^2} \tag{4.3}$$

where $R_0 = R_0(Esin(\omega t), Q_{CF_3}, Q_{CH_3CO^+})$ takes into account the offset of the inner barrier maximum by the CF_3 fragment charge, where the upper state is localized [42].

For small inter-fragment distances, we have to consider other effects, such as the stark shift,Δ, of the upper state in the CF_3 well and the IP of the CH_3CO^+ fragment, which depends on the inter-fragment distance, R. This rate is then written as

$$u_2(t) = u_{adk}[IP_{CH_3CO^+}(R) - \Delta(Esin(\omega t), R); Esin(\omega t); Q_{CF_3} + Q_{CH_3CO^+}]. \tag{4.4}$$

Using both Eqs. 4.1 and 4.4, we can write down an expression for the total ionization rate, u_{tot}, from the CF_3 fragment,

$$u_{tot}(t) = \frac{u_1(t)u_2(t)}{u_1(t) + u_2(t)}. \tag{4.5}$$

The code for these calculations are presented in detail in Appendix B. Figure 4.8 show the results of of our calculations. It shows that there is an ap-

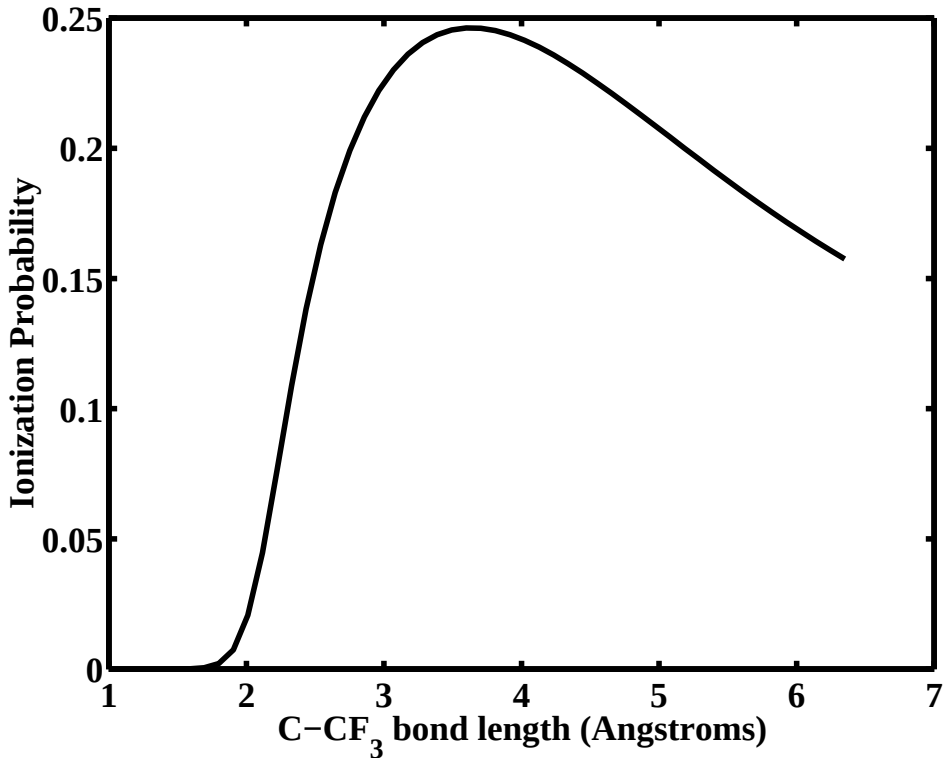

Figure 4.8 Results of enhanced ionization calculations on TFA. Note the enhancement in the ionization probability at $3.5\mathring{A}$

parent enhancement in the ionization probability for TFA at a critical inter-fragment distance of $3.5\mathring{A}$. This result suggests that enhanced ionization is perhaps the mechanism for the enhancement in the CF_3^+ production.

To be certain about whether or not a wave packet could make it to this critical inter-fragment distance in the time scales that we observe in the structure of the optimal pulse and the pump-probe ion yield, we have to perform wave packet calculations. To do this rigorously, we would have to form a PES that takes into account the full dimensionality of the molecule. For a poly-

atomic molecule, the dimensionality could be as large as $3N$-6, where N is the number of atoms in the molecule. For TFA, this would give us a staggering 24 dimensional potential energy surface. Of course, this is difficult to imagine. So we look further into the structure calculations to see what are the most important dimensions responsible for the control. Figures 4.9 and 4.10 show all of the relevant bond lengths and bond angles associated with creating the relaxed PES shown in Fig. 4.4. This data is plotted as a function of energy using the one-to-one relationship between energy and C-CF_3 distance.

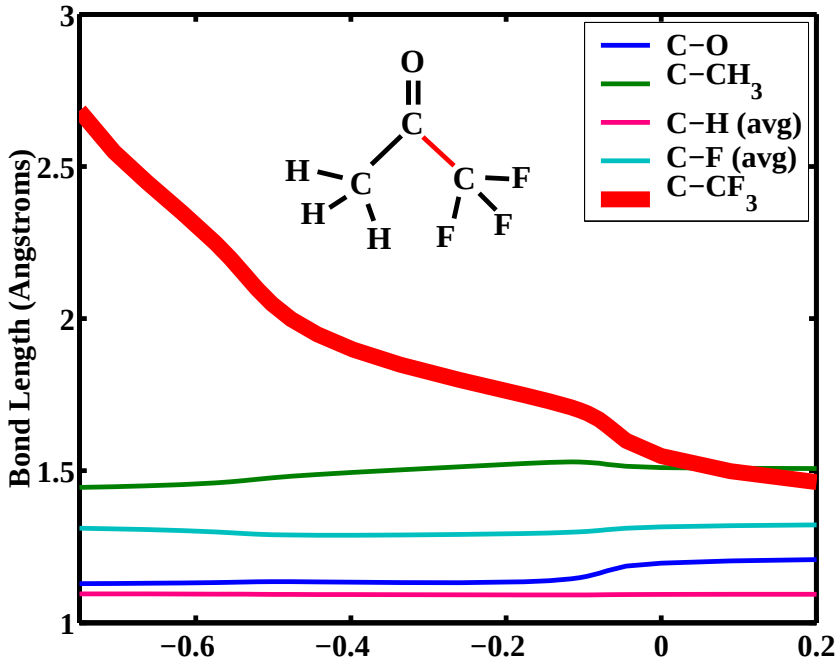

Figure 4.9 Bond lengths as a function of relaxation energy. Note that the bond that undergoes the largest change as a function of energy is the C-CF_3 bond. Zero energy corresponds to the zero energy of the ion in the neutral geometry of TFA.

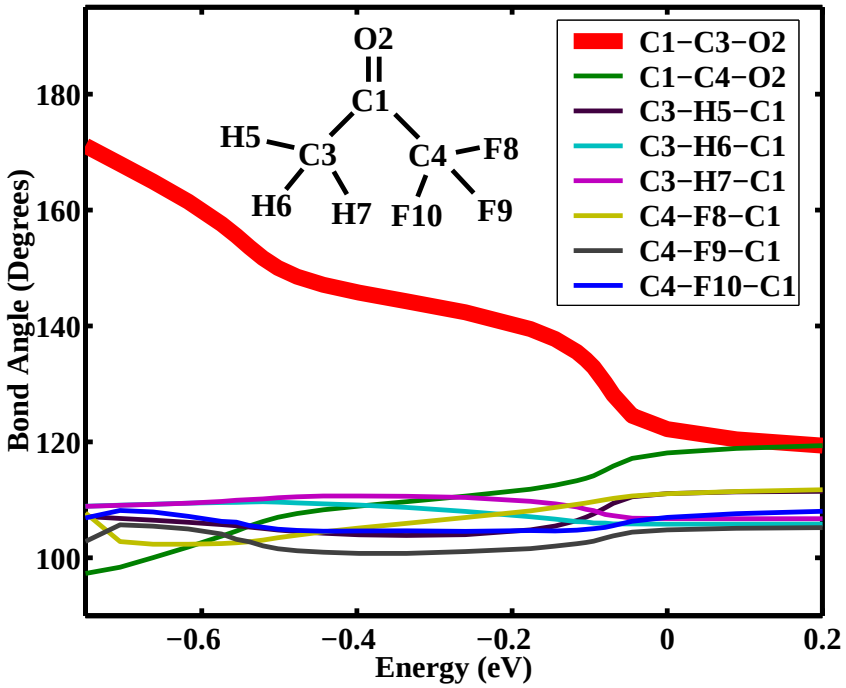

Figure 4.10 Bond angles as a function of relaxation energy. The $C-C-O$ angle in the CH_3CO fragment is the bond angle that undergoes the most significant change.

Figs. 4.9 and 4.10 illustrate that molecule relaxes predominantly along two coordinates. The $C-CF_3$ bond length and the $C-C-O$ bond angle. As the molecule dissociates, we have already ascertained that the $C-CF_3$ bond length elongates until the molecule dissociates. As this process occurs, however, the $C-C-O$ bond angle opens up, going from an angle of $\sim 120°$ to $\sim 180°$. This means that the CH_3CO^+ fragment is almost linear after the molecule dissociates. All other bond lengths and bond angles make relatively small changes. Because of this, we can describe the dissociation using only

two coordinates.

A complete theoretical treatment of the wave packet dynamics during dissociation would require propagation of a wave packet along a two-dimensional PES defined by these coordinates. We can begin to characterize the wave packet motion by considering carefully chosen one-dimensional potential energy curves as a function of the dissociation coordinate. In our present analysis we use two potential energy curves which are shown in Figure 4.11. The

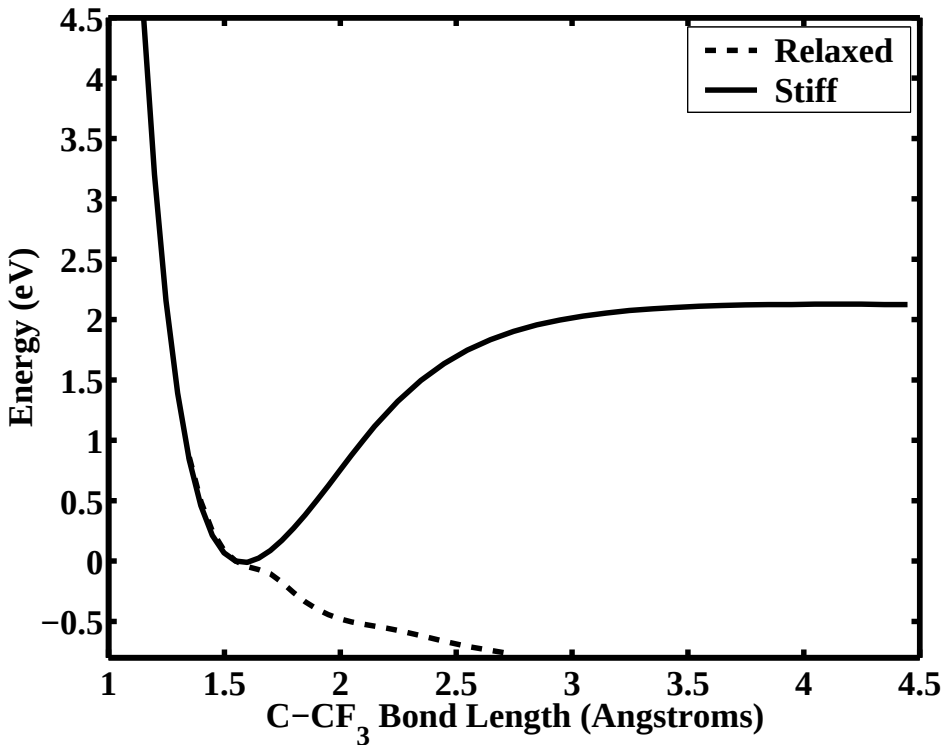

Figure 4.11 "Stiff" (solid) and "relaxed" (dashed) curve for the ground ionic state of TFA.

"relaxed" curve (dashed line), which is the same as that shown in Fig. 4.4,

corresponds to slow motion along the $C - CF_3$ axis relative to the other coordinates. The "stiff" curve (solid line) corresponds to rapid motion along $C - CF_3$ relative to other coordinates, and was constructed by scanning over C-CF_3 distance while holding the CH_3CO^+ and CF_3 fragments fixed in their respective geometries for neutral TFA.

An important difference between these two curves is that the "relaxed" curve is a monotonically decreasing function of $C - CF_3$ distance while the "stiff" curve shows a potential well. In other words, the "stiff" curve shows a barrier to dissociation while the "relaxed" curve does not. The existence of a barrier in the "stiff" curve indicates that relaxation of the fragments must occur prior to dissociation. In terms of the one-dimensional potential energy curves, relaxation of the fragments (primarily a straightening out of the C-C-O angle in CH_3CO^+) causes a collapse of the barrier to dissociation that exists in the "stiff" curve. On the two-dimensional PES, this means that the wave packet cannot move straight out along the $C - CF_3$ distance but must also move in the direction of increasing $C - C - O$ angle so that the wave packet can go around the barrier. Figure 4.12 shows an approximate two dimensional PES as a function of both of these coordinates. The white line in Fig. 4.12 is a classical wave packet trajectory calculated on this surface. The surface was created from the structure calculations, but the sampling along

the $C-C-O$ angle is too coarse to perform accurate quantum mechanical wave packet calculations.

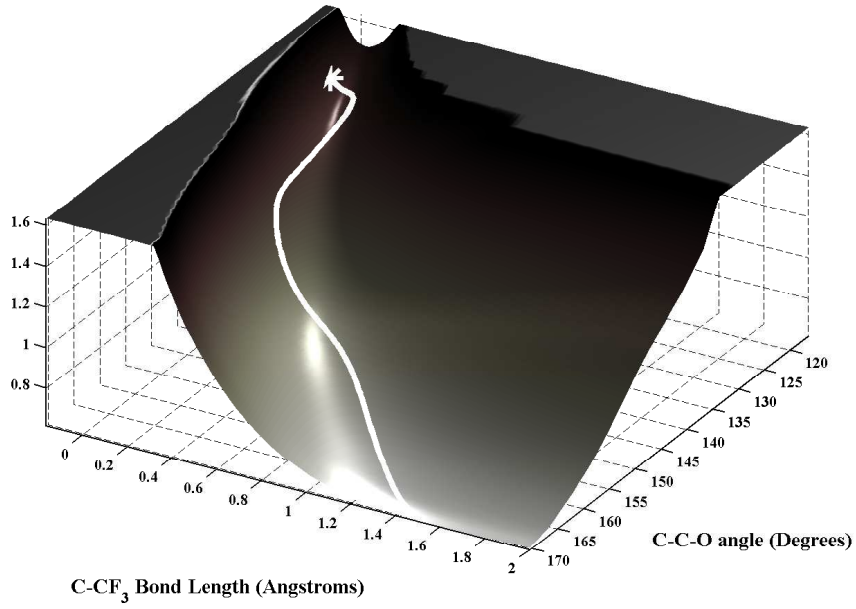

Figure 4.12 Cartoon two-dimensional PES for TFA illustrating path of wave packet after ionization of the molecule.

Following rapid ionization of TFA, a wave packet forms on the ionic PES at the location of the equilibrium geometry for the neutral molecule. Since the fragment geometries do not immediately change significantly from those for the neutral molecule, the initial dynamics of the wave packet can be characterized by the "stiff" curve in Fig. 4.11. Specifically, the wave packet initially forms about 0.05 Å to the left of the minimum of the well. As the primary nuclear motion needed to get around the barrier is the straightening of the $C-C-O$

angle in the CH_3CO^+ fragment, the timescale for the "collapse" of the barrier to dissociation seen in the "stiff" curve is given by the time for the $C-C-O$ angle to open up from 120° to about 175°.

To get a rough estimate of this timescale we considered an isolated CH_3CO^+ fragment. We calculated a potential energy curve for CH_3CO^+ as a function of $C-C-O$ angle with both the $C-C$ and the $C-O$ bond lengths held fixed. A one-dimensional wave packet launched on this potential energy curve at a $C-C-O$ angle of 120° was found to reach 175° in about 55 fs. In the actual dissociation of $CF_3COCF_3^+$ this timescale will be modified by the presence of the CF_3 radical and the fact that the C-O bond length changes. Thus, we expect that after about 55 fs the wave packet evolving on the two-dimensional PES should be able to move unencumbered towards dissociation.

Now we consider the timescales for motion along the C-CF_3 distance. A one-dimensional wave packet launched 0.05 Å to the left of the minimum of the "stiff" potential energy curve reaches its classical turning point on the other side in less than 40 fs. Comparing this with the 55 fs timescale for relaxation of the CH_3CO^+ fragment it seems likely that the wave packet evolving on the two-dimensional PES will encounter the outer barrier rather than simply go around it. These timescales are estimates, but the model presented here has the potential of providing a means for experimentally determining the

relaxation timescales during dissociation.

When the wave packet encounters the outer barrier, a portion of the wave packet is reflected, with the rest either tunneling through or going over the end of the barrier. Any portion that reflects off the outer barrier will then travel to and from the inner barrier. The time for the reflected portion of the wave packet to return to the outer barrier is approximately the vibrational period of the "stiff" potential. If the reflected portion of the wave packet were to again encounter the outer barrier, the process would repeat, leading to a series of wave packets that reach the critical distance at time intervals of, approximately, the vibrational period of the stiff potential. This phenomenon could be responsible for peak 3 in Fig. 4.5. A major test of this model is whether or not this period corresponds to the spacing between peaks 2 and 3 in Figure 4.5.

The vibrational frequency of the "stiff" potential is 12 THz, giving a period of 85 fs. This matches the temporal spacing between peaks 2 and 3 in the pump-probe data, which is 85 ± 8 fs. Thus, our model correctly predicts the time delay between peaks, strongly suggesting that the two peaks in the pump-probe data result from partial reflection of a molecular wave packet during fragmentation.

Since only two peaks are observed in the pump-probe data, we infer that

the wave packet is able to go around the barrier (without reflection) after some time between 1/2 and 3/2 of the $C - CF_3$ vibrational period (42 to 126 fs using the vibrational period from the stiff curve) following the initial ionization. Indeed, our estimate of 55 fs for the opening up of the $C - C - O$ angle lies within this range.

To conclude our analysis, we consider the timing of the second peak. This should correspond to the time it takes the first piece of the wave packet to reach the $C - CF_3$ distance for enhanced ionization. To estimate this time, we launched a one-dimensional wave packet on the "stiff" and "relaxed" potential energy curves. Since the most relevant curve near the launch of the wave packet is the "stiff" curve, we first propagate the wave packet from the launch point (the neutral equilibrium geometry) to the classical turning point on the "stiff" curve. Then we take the wave packet at this position and propagate it until it reaches the position where we predict enhanced ionization to be maximal (between 3.3 and 4.1 Å). The time it takes the wave packet to reach the classical turning point in the "stiff" curve is about 40 fs, and the time it takes the wave packet to propagate the remaining distance on the "relaxed" potential is between 105 and 135 fs (corresponding to the time it takes to reach 3.3 and 4.4 $\mathring{A}$ respectively). This leads to a prediction that the wave packet should reach the critical distance for enhanced ionization between 145 and 175

fs. The first peak in our pump-probe data is at 170 fs, which lies within the range of predicted values. Thus the one-dimensional wave packet calculations agree well with our experimental data.

As a final test of the control model, we made a rough measurement of the kinetic energy of the controlled fragments. We placed a small aperture (500 μm) in the TOFMS, and measured the fragment yield through the aperture for optimally shaped pulses with the laser polarized both parallel and perpendicular to the TOFMS axis. Figure 4.13 illustrates the measurement. The

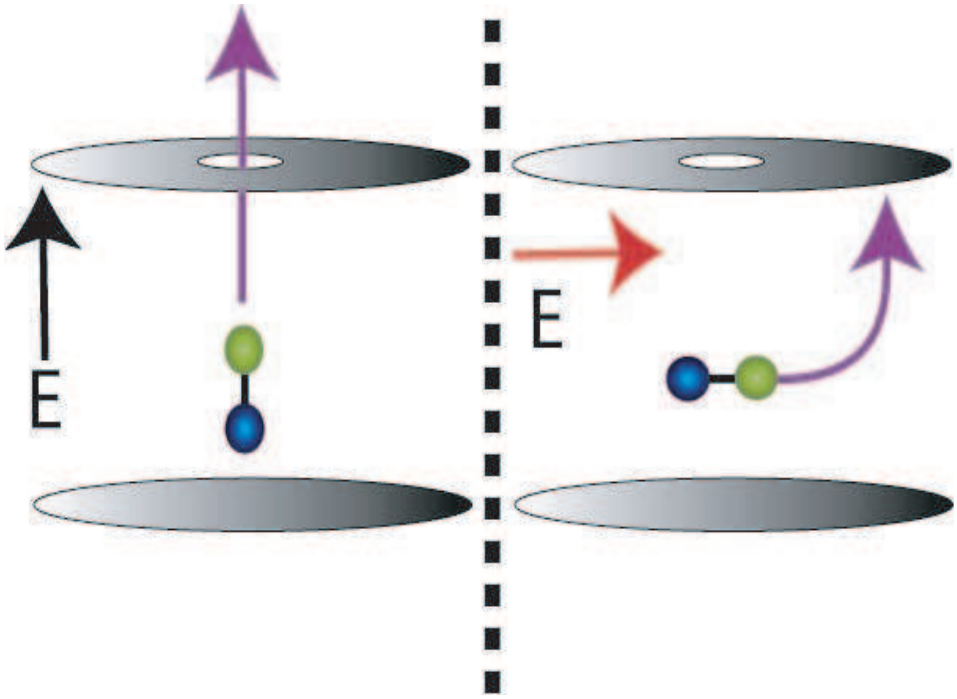

Figure 4.13 Illustration of kinetic energy experiment. Molecules with their enhanced ionization axis perpendicular to the TOF axis will acquire kinetic energy perpendicular to the TOF axis and miss the aperture (right side of figure). Molecules with their axis aligned parallel to the TOF axis will dissociate with KE parallel to the TOF axis and make it through the aperture (left side of figure).

control model predicts a reduction in CF_3^+ and CH_3CO^+ signal in going from parallel to perpendicular polarization. This is because these fragments should acquire additional momentum along the laser polarization when they are created through enhanced ionization, thus missing the aperture. Figure 4.14 shows two TOFMS, one taken with the polarization parallel to the TOF axis, and one taken with the polarization perpendicular to the TOF axis. With an

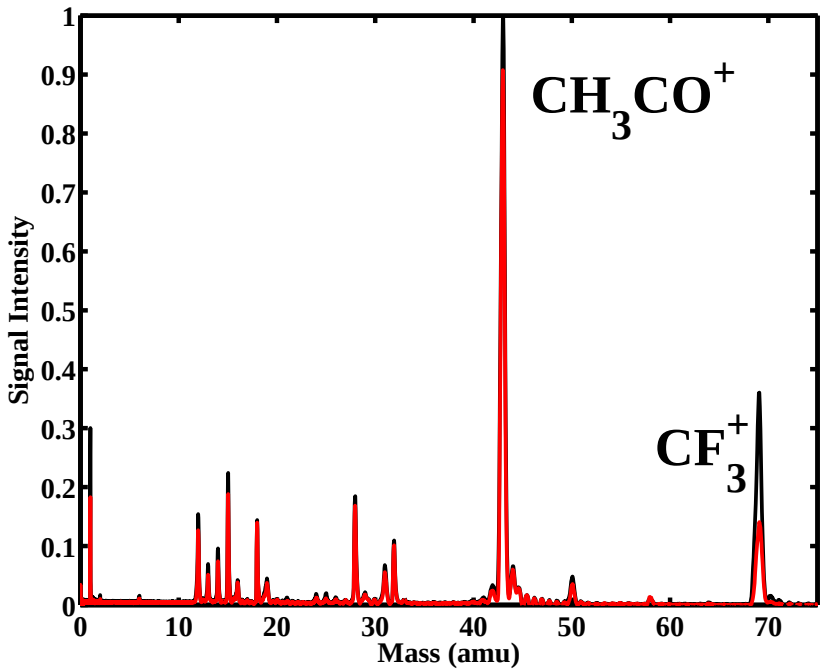

Figure 4.14 TOFMS for polarizations perpendicular (red) and parallel (black) the TOF axis.

optimal pulse incident on the molecular sample, both the CF_3^+ and CH_3CO^+ yields showed a marked increase (2.43 and 1.14 times, respectively) for the laser polarized parallel to the TOFMS axis, while all other peaks in the TOFMS

changed very little with polarization. Note that the mass peaks that have no relevance to the TFA mass spectrum, such as H_2O^+, show no change as a function of polarization.

In summary, we have developed a model for the control mechanism that allowed us to increase the amount of CF_3^+ created in our learning control experiments. This model can be succinctly described in three steps: 1) Ionization of TFA, leading to a dissociative parent molecule, 2) wave packet evolution on the ground ionic state PES, and 3) enhanced ionization when the wave packet reaches the critical $C - CF_3$ distance of $3.5\mathring{A}$. The ideas in Chapter 3 helped in the development of the model. These ideas included which included changing basis in our genetic algorithm and making key parameter scans, like the pump-probe scans described in this chapter.

One reason for creating a model for the control mechanism is to use of the model to predict control in molecules that display similar behavior, or to predict control in a family of molecules. We would like to test the model's predictive power on family members of the halogenated acetones. In the next chapter, we will discuss our efforts towards the goal of having predictive power when using laser pulses to control fragmentation. This will further our goal of using our shaped, ultrafast laser pulses as photonic reagents in chemical reactions.

Chapter 5

Predicting Control in Halogenated Acetones

In Chapter 4, we used methods from Chapter 3 to help us develop a model for the mechanism responsible for controlling the CF_3^+/CH_3^+ ratio in learning control experiments performed on trifluroacetone. The model consisted of three steps: 1) Ionization of the molecule which leads to an unstable parent ion that autodissociates, 2) wave packet evolution on the dissociative ionic PES and 3) enhanced ionization when the wave packet reaches the critical inter-fragment distance.

We use this model to predict control of dissociative ionization in a family of halogenated acetones. In this chapter, we will concentrate our efforts on 1,1,1-Trichloroacetone (CH_3COCCl_3, TCA) and Acetone-alpha,alpha,alpha-d3 (CH_3COCD_3, TDA). From the chemical formulas it can be seen that the TCA and TDA are different from TFA only in that we are exchanging fluorine

for chlorine and deuterium in these molecules.

Armed with an initial hypothesis, we start our analysis by looking at molecular structure calculations performed on TCA and TDA. Figure 5.1 shows both the "stiff" (solid) and "relaxed" (dashed) PES's for the ground ionic states of TCA and TDA. The dotted line in Fig. 5.1(a) refers to the equilibrium position

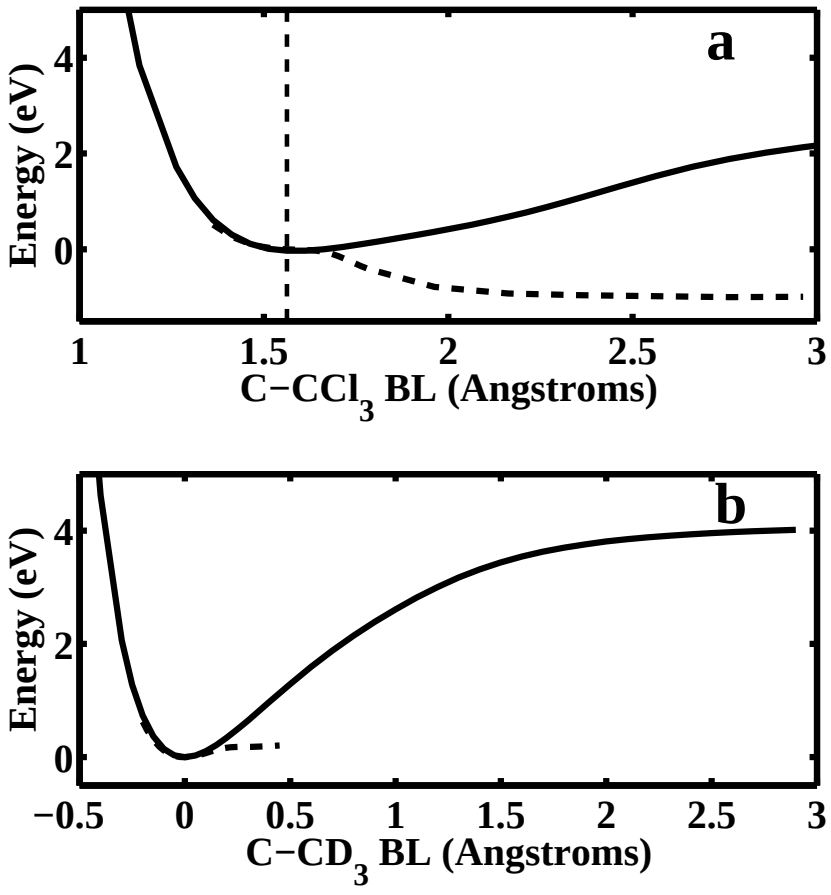

Figure 5.1 Both the "stiff" and "relaxed" curves for (a) TCA and (b) TDA.

of the neutral ground state. The PES's here were made in similar fashion to

those made for TFA which are shown in Chapter 4, Fig. 4.11. The "relaxed" curve in Fig. 5.1(a) clearly shows that autodissociation of TCA^+ will occur after ionization. In the case of TDA, however, the "relaxed" curve shown Fig. 5.1(b) has a barrier to dissociation. This will lead to a stable parent ion.

As a zeroth order check of our calculations, we look to the TOFMS of both TCA and TDA to see if there are any signs of a stable parent ion. Figures 5.2 and 5.3 show the TOFMS for TCA and TDA, respectively. Both of these

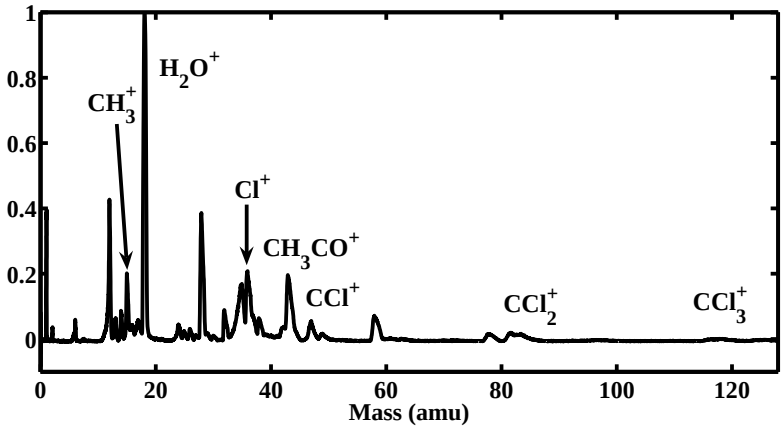

Figure 5.2 TCA TOFMS.

spectra were taken with nearly transform limited, unshaped laser pulses. We see from the TCA TOFMS that there is no sign of a parent ion. This is consistent with the fact that the "relaxed" curve in Fig. 5.1(a) shows that the parent ion is not bound. However, looking at Fig. 5.3, it is clear that the major peak in the spectrum is the parent ion, TDA^+. This result is also consistent with our calculations. With this information, we can hypothesize that TCA

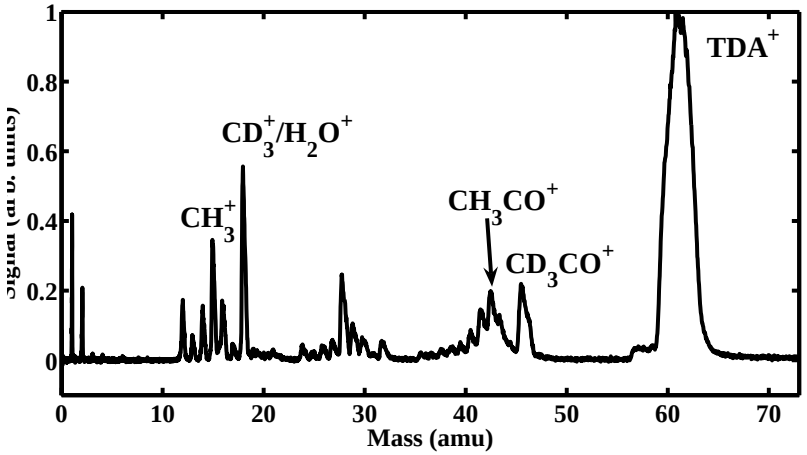

Figure 5.3 TDA TOFMS.

will be controllable through enhanced ionization, similar to TFA. However, TDA appears to have a stable parent ion. This means that a wave packet will not be able to reach the critical inter-fragment distance required for enhanced ionization to occur.

The TFA results, coupled with the initial data taken on TCA and TDA, have led us to perform molecular structure calculations that led to the PES's that are shown in Fig. 5.1. Using information gained from the calculations, we want to make more specific predictions about how the control will take place in TCA. We do this by comparing and contrasting the "relaxed" curves for both TFA and TCA. Figure 5.4 shows close up views of the "relaxed" PES's for both TFA and TCA around the points where the initial wave packets are launched. Again, the dotted line in the figures refers to the equilibrium

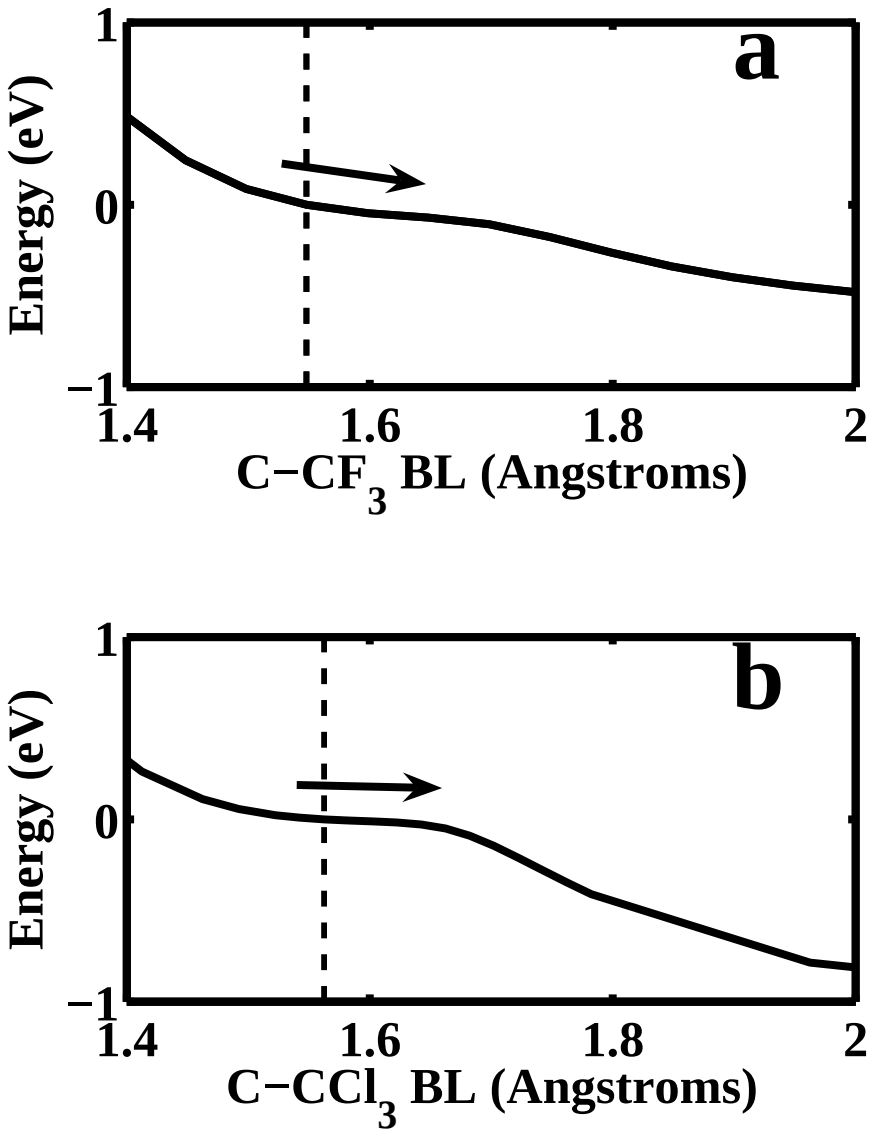

Figure 5.4 Close up views of the positions on the "relaxed" curves where the wave packet is initially launched to for (a) TFA and (b) TCA.

position of the neutral ground state. One observation that can be made from this figure is that the TFA "relaxed" PES has a much larger slope near the launch point than that seen in the "relaxed" curve for TCA. There is a ledge near the launching point of the wave packet in the TCA case. The difference in the gradients around the launching points is noted by the arrows in Fig. 5.4. The gradient for the TFA curve is ~ 3 times faster than it is in TCA. Also, the calculations tell us that the "stiff" curve in the TCA is shifted by 0.02 Åwith respect to the neutral ground state. This shift is smaller than that seen in the "stiff" curve in TFA, which was found to be 0.06 Å. Both of these differences will cause a wave packet formed on the "relaxed" surface of TCA to acquire less kinetic energy after being launched, leading the wave packet to initially move slower on the "relaxed" PES. We predict that this will cause a wave packet that propagates on this "relaxed" curve to become dispersed, leading to a spatially large wave packet.

To confirm this hypothesis, we perform one-dimensional wave packet calculations on the TCA "relaxed" surface, and compare the wave packet shape with that of a wave packet that propagates on the TFA "relaxed" surface. Figure 5.5 shows the results of those calculations, where the leading edge of the wave packets are allowed to propagate a distance of ~ 2 Å. The calculations show that the wave packet that evolves on the TCA PES slowly leaks

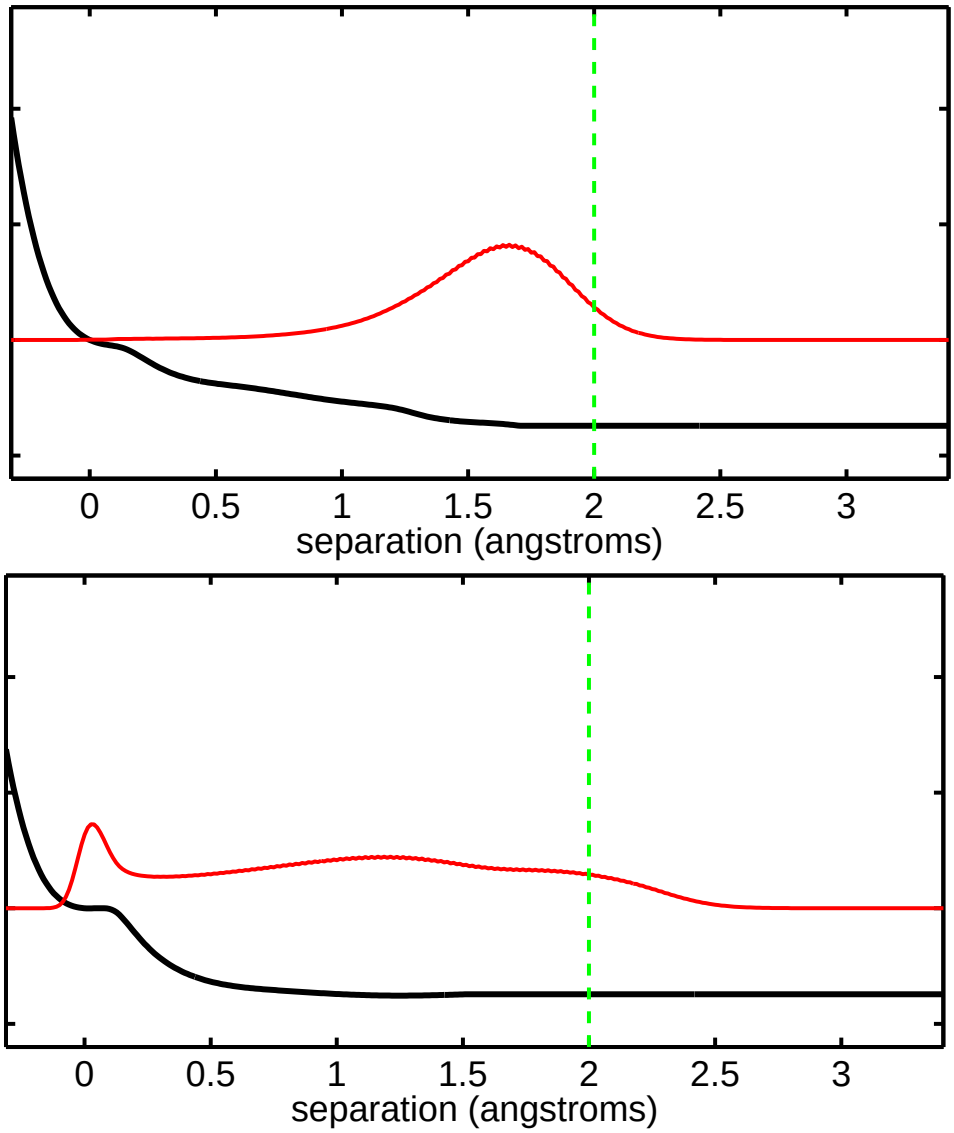

Figure 5.5 Simulated wave packet evolution on "relaxed" curves of (a) TFA and (b) TCA. These are snapshots of the simulation at the point where the wave packets reach 2 Å.

off the ledge, leading to a dispersed, spatially broad wave packet. The wave packet in Fig. 5.5(b) shows that the wave packet that evolves on the TFA PES disperses, but not in the same manner as seen in the TCA. There is no

evidence of wave packet around the launching point, meaning that the wave packet quickly moves away from the launch point. this leads to a relatively smaller spatial spread of the wave packet.

The time at which enhanced ionization can occur after the parent ion begins to dissociate is a function of both the wave packet dynamics en route to the enhancement position as well as the location of the enhancement position itself. Quasi-static molecular ionization calculations predict enhanced ionization of the CCl_3 fragment at a $C - CCl_3$ inter-fragment distance of 2.9 Å, somewhat smaller than the $C - CF_3$ distance for TFA, which we have calculated to be 3.6 Å[17]. This would indicate that energy considerations (which predict longer timescales) outweigh the smaller distance to enhanced ionization in TCA, resulting in a broader wave packet which reaches the enhanced ionization position at longer times.

In our control experiments, we expect to see evidence of a broad wave packet. This evidence will manifest itself in the form of longer delays between the ionization pulse and the enhanced ionization sub-pulse in the optimal control sub-pulse. We also expect to see evidence of a broad wave packet passing the enhanced ionization distance in the pump-probe spectroscopy, which would look like a broad enhancement in the CCl_3^+ ionization yield as a function of pump-probe delay. Using the knowledge gained from the analysis above, we

test our hypotheses.

We performed learning control experiments on TFA, TCA and TDA with the goal of optimizing the CX_3^+ to CH_3^+ ratio. The amount of control we were able to achieve for each species is illustrated in Figure 6.1, where the CX_3^+/CH_3^+ ratios are given both for optimized (white bars) and unshaped (black bars) laser pulses. The small difference between the ratios for shaped

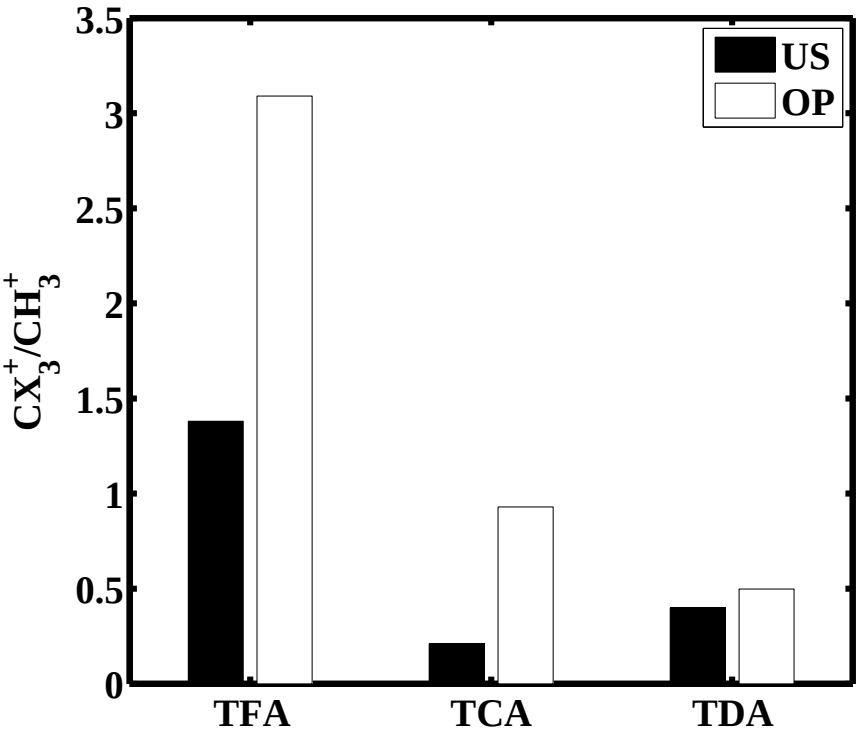

Figure 5.6 CX_3^+/CH_3^+ ratios for unshaped pulses (black) and optimally shaped pulses (white).

and unshaped pulse with TDA illustrates the lack of control, while the larger

differences with TFA and TCA demonstrate significant control for these molecules. This data bears out the initial predictions we made from looking at the PES in Fig. 5.1. Figure 5.7 shows the TOFMS for TCA taken with both a shaped and an unshaped pulse. The insets in Fig. 5.7 show that the CCl_3^+ signal was

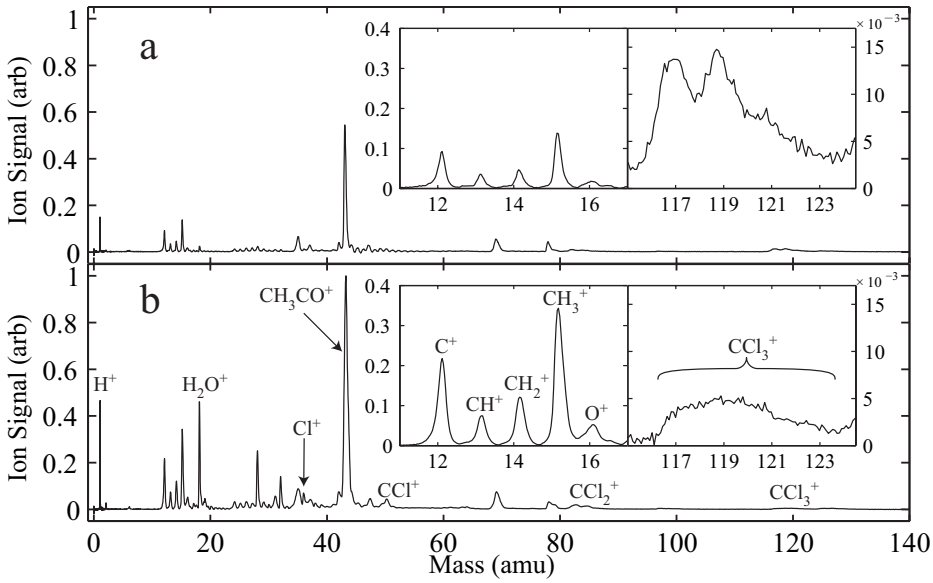

Figure 5.7 TOFMS for TCA taken with (a) an optimally shaped pulse and (b) an nearly transform limited unshaped pulse [30].

enhanced by the optimally shaped pulse. The lack of control seen for TDA is also consistent with our predicitions.

Optimal pulses for maximizing the CF_3^+/CH_3^+ and CCl_3^+/CH_3^+ ratios (characterized using SHG FROG [20]) are shown in Figures 5.8(a) and (b). Both of these pulses have similar periodic temporal structure. However, it is interesting to note that the peak separation in the optimal pulse for CCl_3^+

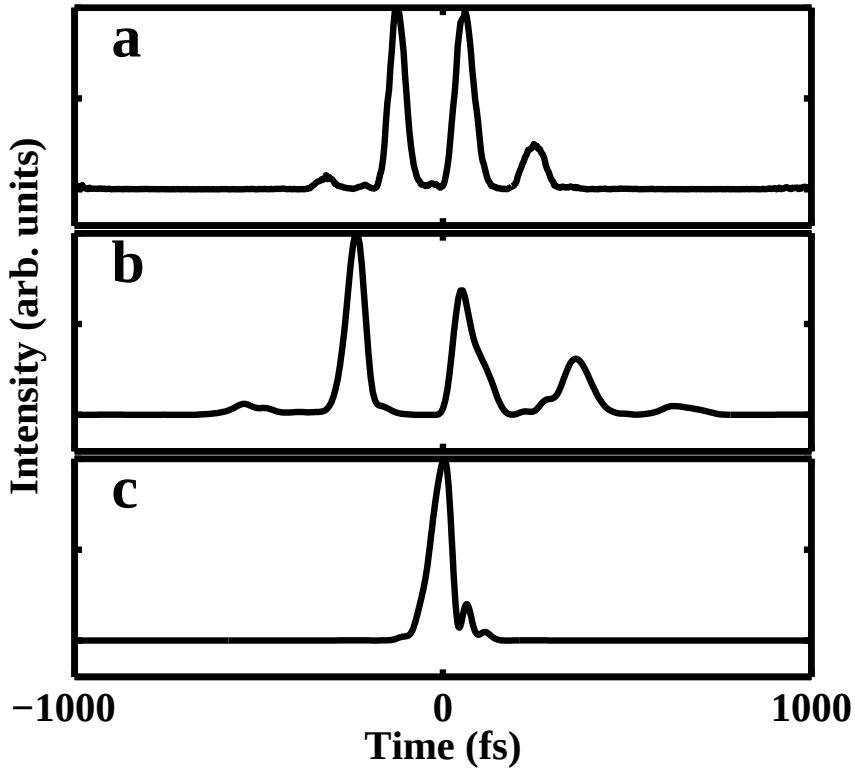

Figure 5.8 Optimal control pulses for controlling the CX_3^+/CH_3^+ ratio in (a) TFA, (b) TCA and (c) TDA.

production is larger than the peak separation in the optimal pulse for CF_3 production. As the pulse shaper is again limited to phase only modulation in these experiments, it is impossible to create a simple pulse pair in the time domain. The pulse sequences discovered by the GA are characteristic of spectral phase modulation. We therefore concentrate on the separation between the

two main pulses in the sequence for our interpretation. The subpulse separation in the optimal control solutions were 170 fs and 330 fs for TFA and TCA, respectively. Multiple optimization runs in TFA yielded similar solutions, but the solutions for TCA displayed significant variation in the spacing between subpulses. A histogram of the dominant Fourier components of optimal solutions discovered by the algorithm for TCA has a peak at 3 Thz and a width of 2 THz, corresponding to solutions with subpulses separated from 250-500 fs. These observations are consistent with our prediction of longer timescales for dissociation and a broader wave packet in TCA relative to TFA. In contrast to the TCA and TFA optimal pulses, the TDA optimal pulse shape, Fig. 5.8(d), has no similar intensity structure. This combined with the lack of control and the stability of the parent ion indicates that enhanced ionization does not contribute to the production of CD_3^+.

The optimal control pulses discovered for TCA suggest that the GA has chosen a longer delay between subpulses in TCA because the wave packet takes longer to reach the enhancement position. Furthermore, the GA finds a range of optimal subpulse delays, suggesting a broad wave packet crossing the enhanced ionization position. We look to pump-probe measurements for confirmation of these ideas. In the pump-probe experiments we recorded the TOFMS as a function of pump-probe delay between two, unshaped 33 fs

pulses. The pump and probe pulse intensities were 2.2×10^{14} W/cm^2 and 1.2×10^{14} W/cm^2 respectively. These intensities are similar to the intensities of the sub-pulses in the solutions found in the learning control experiments. The expectations based on the structure calculations are that there should be enhancements in the CF_3 and CCl_3^+ productions at nonzero time delays, with no enhancements in the CD_3^+ production. More specifically, based on the shape of the relaxed and stiff potential energy curves, we expect the enhancement in TCA to come later and be broader than the enhancement in TFA.

Figure 5.9 shows the pump-probe ion signal for all three molecules. All ion signals in the TOFMS showed a significant enhancement at $t = 0$, when the two pulses overlapped in time. All of the ion yields in the figure are normalized to the ion signal at $t = 0$. The CF_3 yield has two distinct peaks following $t = 0$ (at $t = 170$ fs and $t = 255$ fs), and the CCl_3^+ yield has one broad peak (at about $t = 350$ fs). The CD_3^+ yield shows no structure after $t = 0$. No other peaks in the TOFMS showed any significant modulation after $t = 0$ in any of the three molecules.

That both the TFA and TCA show evidence of enhanced CX_3^+ production at nonzero time delays, while the TDA does not, is consistent with the structure and wave packet calculations and the control data. The timing of the

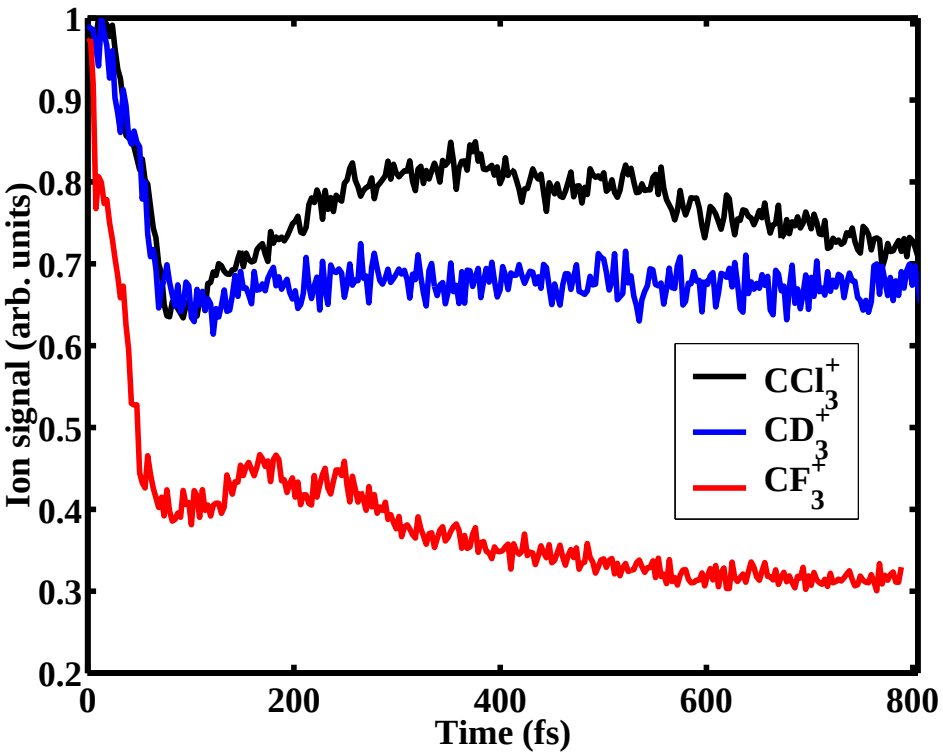

Figure 5.9 Pump-prove ion yield of CCl_3^+ (black), CF_3^+ (red) and CD_3^+ (blue).

first peak in the CF_3^+ yield matches the subpulse spacing in the optimal pulse for TFA, and the timing of the peak in the CCl_3^+ yield matches the subpulse spacing in the optimal pulse for TCA. Furthermore, the spread of optimal subpulse spacings for TCA (250-500 fs) is consistent with the width of the peak in the pump-probe data (∼300 fs). The enhancement in the CCl_3^+ ion yield does not show a double enhancement structure like that seen in CF_3^+. This is because the wave packet evolving on the TCA "relaxed" potential does not acquire a significant amount of energy at the point of its launch. That means that the relaxation of the molecule occurs before the slowly evolving

wave packet encounters a barrier to dissociation. Once the CH_3CO^+ fragment rearranges, with a timescale similar to that in TFA^+, the molecule can slowly dissociate along C-CCl_3, reaching the enhanced ionization position much later than in TFA. In the pump-probe data for TCA, both the broader width and the slower motion of the wave packet, compared with TFA, are evident. The pump-probe experiment serves as a direct measurement of the spatial extent of the the wave packet during dissociation.

To further test the control model for TCA and TDA, we performed a polarization test similar to that done for TFA and described in Chapter 4. We placed a small aperture (500 μm) in the TOFMS, and measured the fragment yield through the aperture for optimally shaped pulses with the laser polarized both parallel and perpendicular to the TOFMS axis. It was found that the CCl_3^+ ion yield demonstrated a 1.2 times increase for the data taken with the laser pulse polarization parallel to the TOF axis. Because enhanced ionization is not responsible for any increase in CD_3^+ ion yield, we measure no difference in the CD_3^+ yield a function of polarization.

In this chapter, we have shown that we can predict the outcome of learning control experiments. By developing a model for control in one molecule, TFA, we have been able to predict whether or not control was possible through enhanced ionization in similar molecules, TCA and TDA. We used molecular

structure calculations and quasi-static molecular ionization calculations to help us make more detailed predictions about the control in TCA and TDA. These results show that there is promise for using shaped, ultrafast laser pulses as "photonic" reagents in chemical reactions.

In this chapter, and in Chapter 4, we have concentrated on halogenated acetones that have only one methyl group substituted with halogens. We would like to see what happens when we balance the molecule, i.e. by replacing hydrogens in both methyl groups with halogens. Will we see the same type of control, or will the control mechanism be different due to the balancing of the halogens in the molecule? We look to answer these questions in Chapter 6.

Chapter 6

Balancing the Halogens

Up to this point, all of the molecules discussed in this thesis have dealt with halogenated acetones where hydrogens from only one of the methyl groups were exchanged with halogen atoms. It was found that enhanced molecular ionization was responsible for controlling the CF_3^+/CH_3^+ and CCl_3^+/CH_3^+ ratio when the hydrogen atoms were replaced with the electronegative atoms fluorine and chlorine. However, when hydrogen was exchanged for deuterium, we saw that we had little control over the CD_3^+/CH_3^+ ratio, as the parent ion in this case had a stable geometry.

In this chapter, we explore what happens when we make a modification to the molecule that exchanges hydrogen atoms on the other methyl group with halogen atoms. The molecule that we are studying control in is 1,1-3,3,3 dibromo-trifluoroacetone ($CHBr_2COCF_3$, Br_2TFA). This structure of

this molecule is similar to TFA, except now we are replacing two hydrogen atoms on the CH_3 group with two Br atoms.

As in our experiments with TFA and TCA, we used the GA to perform a global search for control over different fragment channels, unbiased toward any expected result. In the feedback experiment with Br_2TFA the GA was able to control the relative production of charged methyl fragments.

Figure 6.1 shows the temporal phase and intensity for an optimal laser pulse when maximizing the ratio of $CF_3^+/CHBr_2^+$. The pulse has a high intensity ($\sim 1 \times 10^{14}$ W/cm^2), nearly transform-limited primary pulse, followed by a less intense, longer pulse approximately 300 fs later. Repeated runs of the GA produced similar solutions, with the time delay between the two pulses varying from 250 to 300 fs. The inset to Fig. 6.1 shows the control ratio achieved when maximizing the production of either $CF_3^+/CHBr_2^+$ (A) or $CHBr_2^+/CF_3^+$ (B). It was found that the optimal pulse for maximizing the ratio of $CHBr_2^+/CF_3^+$ is a low intensity, unshaped laser pulse.

Although the control experiments with Br_2TFA were similar to those with TFA and TCA, subtle differences found in the optimal control pulses suggest a different underlying control mechanism. For TFA and TCA the optimal solutions were composed of a series of pulses with the two main sub-pulses having similar intensity (see Fig. 3.4 and Fig. 5.8(b)). For Br_2TFA, an intense

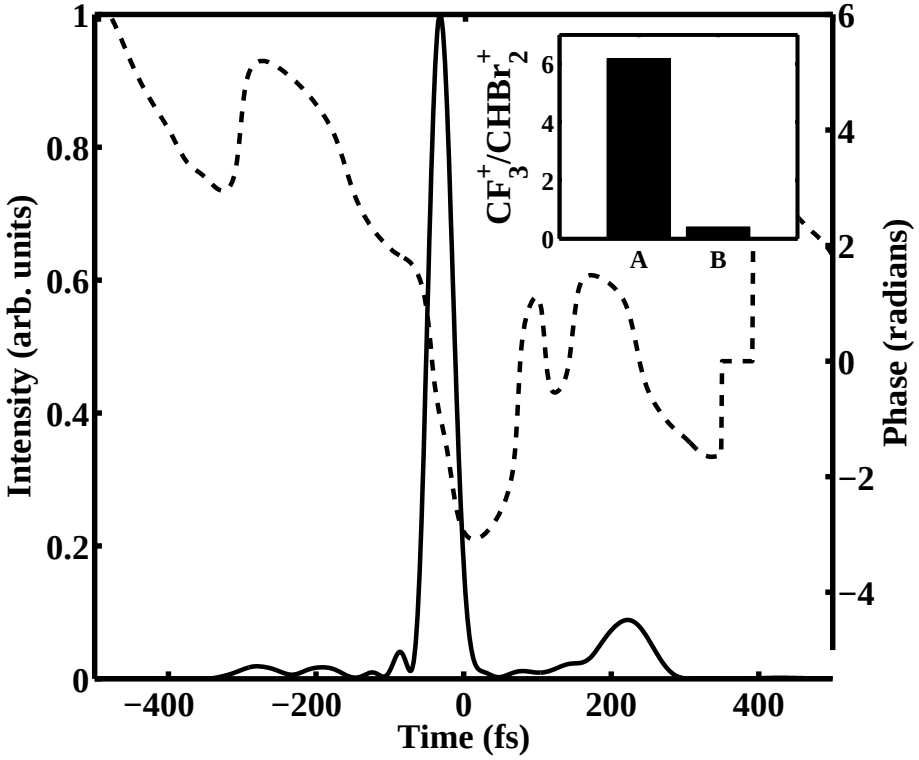

Figure 6.1 Optimal control pulse for maximization of the $CF_3^+/CHBr_2^+$ ratio. The solid line denotes the intensity profile, $I(t)$, and the dashed line denotes the phase, $\phi(t)$. Inset: $CF_3^+/CHBr_2^+$ ratio when the goal was to maximize A) the $CF_3^+/CHBr_2^+$ ratio and B) the $CHBr_2^+/CF_3^+$ ratio.

pulse is followed by a substantially less intense pulse, which would be relatively ineffective for enhanced ionization. Additionally, the control in Br_2TFA was more pronounced than in TFA or TCA (over an order of magnitude in the fragment ratio for Br_2TFA), largely because of the more substantial decrease in the $CHBr_2^+$ yield (compared with CH_3^+) for an optimal pulse. As a final piece of evidence to show that enhanced ionization was not playing a role in the control, we performed the same rough estimates of fragment kinetic

energies as was done for both TFA and TCA. This rough measurement shows that the CF_3^+ fragments in Br_2TFA acquire no additional kinetic energy with an optimal pulse. In the TFA and TCA experiments using the optimal pulse shape increased the kinetic energy of the CF_3^+ and CCl_3^+ fragments due to the effects of enhanced ionization.

As with TFA and TCA, the optimal pulse structure suggests that fragment dynamics play a role in the control mechanism. We investigated this further with a series of pump-probe experiments to measure fragment yields as a function of time delay between the two laser pulses. In these experiments the intensity of the probe pulse was about a factor of four less than that of the pump pulse so that it was incapable of independently photoionizing any of the molecules.

The yields for CF_3^+, $CHBr_2^+$, and $CHBr_2CO^+$ are shown in Fig. 6.2. Production of CF_3^+ is maximized at a delay of $\sim$ 300 fs. Coinciding with this is a decrease in the $CHBr_2^+$ signal. The $CHBr_2CO^+$ signal also appears to be anti-correlated with the CF_3^+ signal except for small delays when the overlapping pulses produce an anomalously large ion signal. The depths of modulation are significant, approaching 25% of the $(t \rightarrow \infty)$ asymptotic values. Also unlike the TFA and TCA pump-probe data, other fragments in the Br_2TFA spectrum showed modulations in their pump-probe signals (CH and

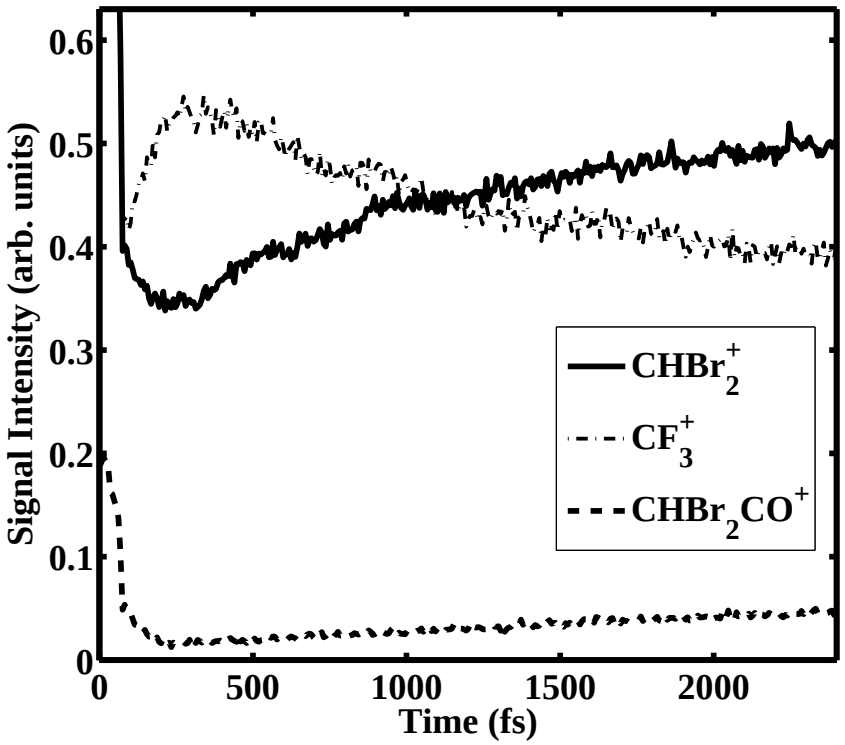

Figure 6.2 $CHBr_2^+$ (solid), CF_3^+ (dash-dot) and $CHBr_2CO^+$ (dashed) signals as a function of pump-probe delay. All yields are normalized to the CF_3^+ signal at zero time delay.

$CHBr$). The pump-probe data indicates that the dynamics occurring after ionization is rich and more complicated that those seen in TFA and TCA. However, in this thesis we will only concentrate on the dynamics associated with the control goal.

The peak in the CF_3^+ yield is similar to results with TFA and TCA. However, the accompanying decrease in the $CHBr_2CO^+$ and $CHBr_2^+$ signals is different (with TFA and TCA the CH_3^+ fragment showed no modulation) and

suggests that charge is transferred from CF_3 to either $CHBr_2CO^+$ or $CHBr_2^+$ [44]. Furthermore, with charge transfer, as opposed to enhanced ionization, the absence of a coulomb repulsion between two closely spaced, charged fragments explains the lack of energetic fragments during control. Before describing further tests of this charge transfer model, we will discuss formation of the fragments from the parent molecule.

In the experiments with TFA or TCA, ionization on the leading edge of the laser pulse produced CF_3 (or CCl_3) and CH_3CO^+ because of the instability of the parent ions. As there is no significant $CHBr_2COCF_3^+$ in the TOFMS for Br_2TFA, we infer that $CHBr_2COCF_3^+$ also auto-dissociates. However, unlike TFA and TCA, the fragmentation of $CHBr_2COCF_3^+$ is not dominated by a single dissociation channel (such as formation of CH_3CO^+ and CF_3 in TFA). $CHBr_2^+$ production is significant at all intensities, so we must consider at least two dissociation channels for the parent ion leading to final products $CHBr_2CO^+ + CF_3$ or $CHBr_2^+ + CO + CF_3$. While not critical for the analysis below, we hypothesize that these final products are formed first by dissociation of $CHBr_2COCF_3^+$ into $CHBr_2CO^+$ and CF_3^+, and then possibly further dissociation of $CHBr_2CO^+$ into $CHBr_2^+$ and CO. This hypothesis is based upon several observations. One is that ionization removes an electron from an orbital on the CO, and another is that CF_3CO^+ is relatively unstable

and not produced in our experiment. Finally, the $CHBr_2^+$ and $CHBr_2CO^+$ yields are correlated, and have similar dependence on laser intensity as discussed below.

In order to better understand the fragmentation following ionization, we measured the fragment yields as a function of intensity for a single, transform-limited laser pulse. The yields for $CHBr_2CO^+$, $CHBr_2^+$, and CF_3^+ as a function of peak intensity are shown on a log-log scale in Fig. 6.3. The FWHM of the pulse was kept at a constant 35 fs. On a log-log scale the $CHBr_2^+$ and $CHBr_2CO^+$ yields as a function of pulse intensity have slopes of 3.5 and 3.2, respectively. This indicates that $CHBr_2^+$ and $CHBr_2CO^+$ are produced by processes of similar multi-photon order. However, the CF_3^+ yield has a slope of 4.4 indicating that production of CF_3^+ is a higher order process.

At low laser intensities the parent ion dissociates primarily into $CHBr_2CO^+$ and neutral CF_3. If the $CHBr_2CO^+$ fragment is left in an excited state it then dissociates into $CHBr_2^+$ and CO with the branching ratio for this three-way fragmentation channel increasing slightly with pulse intensity. Therefore, ionization of Br_2TFA can launch a wave packet on two different, but energetically close, potential energy surfaces (PES's) corresponding to the two dissociation channels,

$$CHBr_2COCF_3 + nh\nu \rightarrow CHBr_2CO^+ + CF_3, \tag{6.1}$$

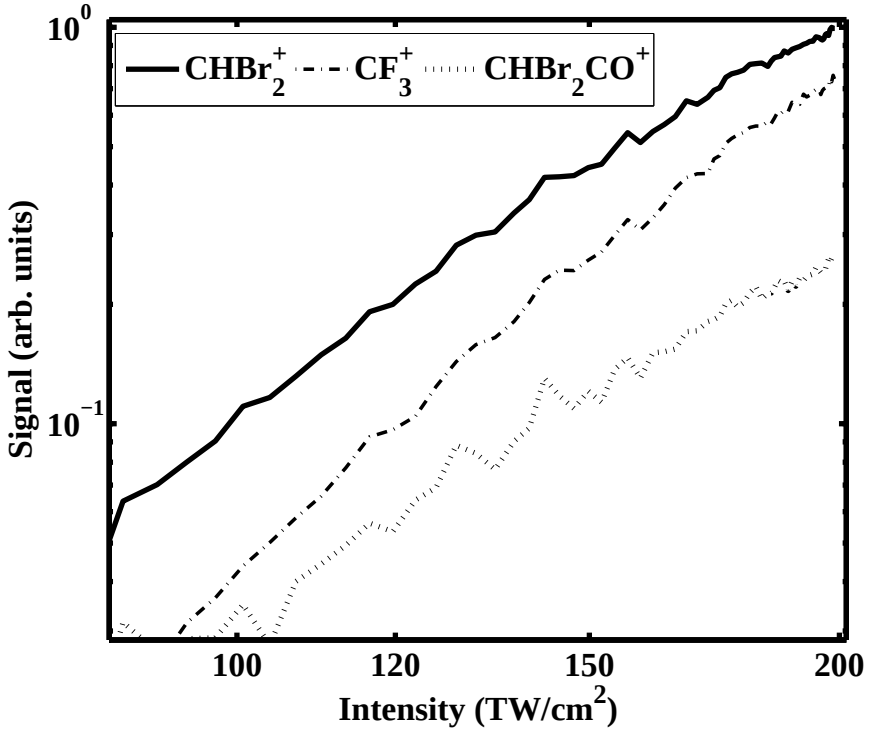

Figure 6.3 $CHBr_2^+$ (solid), CF_3^+ (dashed) and CH_3CO^+ (dotted) signals as a function of laser pulse peak intensity plotted on a log-log scale.

and

$$HBr_2COCF_3 + nh\nu \rightarrow CHBr_2CO^{+*} + CF_3 \rightarrow CHBr_2^+ + CO + CF_3 \quad (6.2)$$

Because the changes in fragment yields are relatively large and appear to show a high degree of anti-correlation, we believe that the PES leading to CF_3^+ and the PES's leading to $CHBr_2CO^+$ and $CHBr_2^+$ must be strongly coupled by the probe pulse. The strong coupling of these surfaces by the laser pulse suggests that the coupling is resonance mediated and the time dependence of

the coupling suggests that the resonance is dynamic [45]. These observations lead to the hypothesis that the charge transfer is mediated by adiabatic rapid passage (ARP)— with a twist. In the usual form of ARP [46], the laser frequency is adiabatically swept, or "chirped", through a static atomic or molecular resonance. For this dynamic ARP, the laser frequency can remain fixed while the difference in energy between two molecular electronic states sweeps through a resonance.

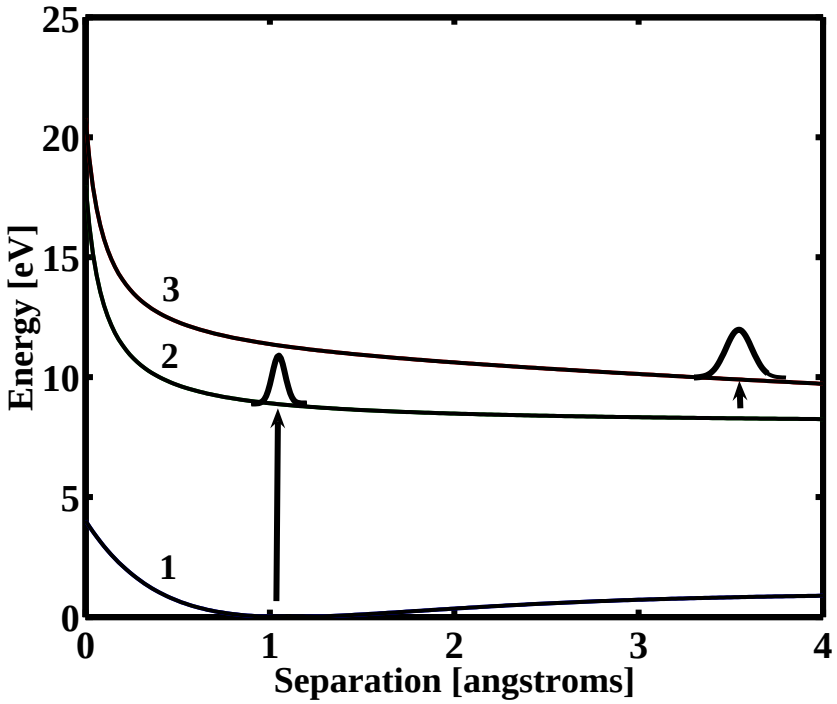

Figure 6.4 Simplified cartoon of hypothetical potential energy surfaces involved in the control mechanism.

Figure 6.4 shows the hypothetical PES's that describe the dynamics associated with the control mechanism. The pump pulse launches a wave packet

from the neutral ground state of the molecule (PES 1) onto a dissociative ionic PES (PES 2) representing fragmentation into $CHBr_2CO^{+*} + CF_3$ or $CHBr_2CO^{+} + CF_3$. When the probe pulse comes ∼350 fs later, the wave packet is promoted to another dissociative ionic PES (PES 3) that leads to $CHBr_2CO + CF_3^{+}$.

In a dressed state picture of the molecular levels, the two electronic states associated with PES's 2 and 3 in Fig. 6.4 are degenerate, but because of their coupling they repel each other, making an avoided crossing. Depending on the electric field strength of the laser and the speed of the fragments, the avoided crossing can be traversed diabatically, resulting in little population transfer between the states, or adiabatically, resulting in almost full transfer. We now describe the results of several tests of the dynamic ARP hypothesis.

Our first test was to measure how the charge transfer depends on probe pulse intensity. Fig. 6.5 shows the ion signals as a function of probe intensity, with the probe pulse coming 350 fs after a transform limited pump pulse. The CF_3^+ signal increases rapidly for low intensities but saturates at higher intensities, as expected for ARP [46]. Increasing the Rabi frequency, e.g. by increasing pulse intensity, allows one to change the passage from diabatic to adiabatic. Once the Rabi frequency becomes large enough to satisfy the adiabatic condition [46], there is no further increase in population transfer.

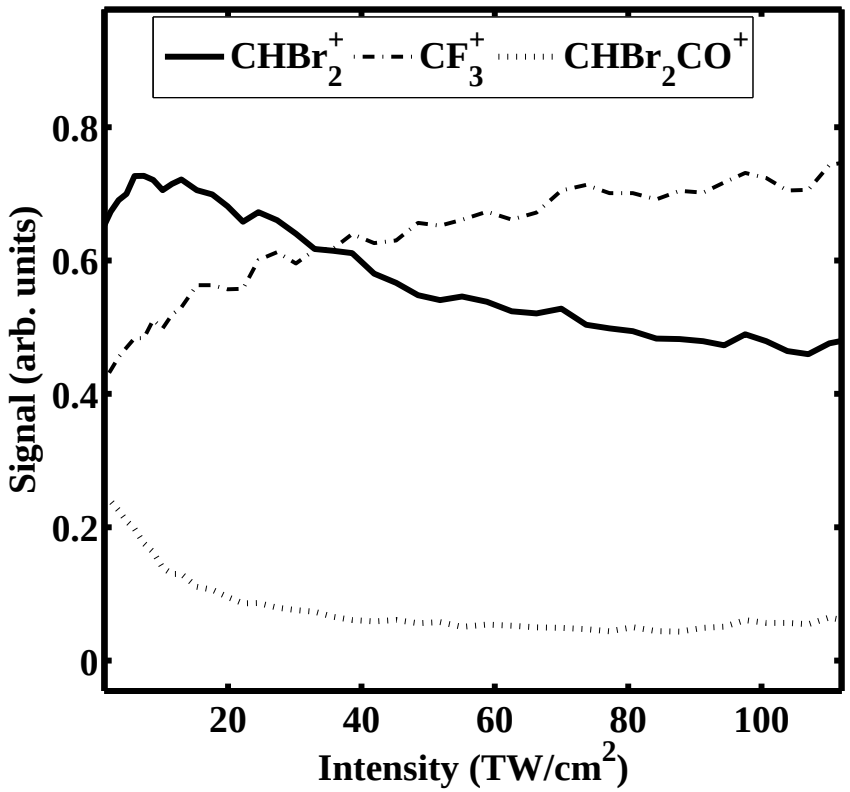

Figure 6.5 $CHBr_2^+$ (solid), CF_3^+ (dashed) and CH_3CO^+ (dotted) signals as a function of peak intensity, for a fixed pulse duration. This data was taken while scanning the intensity of the probe pulse, which was timed to coincide with the CF_3^+ enhancements seen in Fig. 6.2.

The intensity dependences seen in Fig. 6.5 are distinctly different from those of the single pulse intensity scan shown in Fig. 6.3. When the probe pulse energy is increased, production of $CHBr_2CO^+$ and $CHBr_2^+$ actually decreases (aside from a small initial increase in $CHBr_2^+$) and they are anti-correlated with the CF_3^+ fragment. The correlation coefficients were calculated for these curves, and were found to be -0.96 between the CF_3^+ and the $CHBr_2^+$

fragments, -0.91 between CF_3^+ and $CHBr_2CO^+$ and -0.97 between CF_3^+ and $CHBr_2^+$ with $CHBr_2CO^+$.

It is clear that most of the anti-correlation occurs between the $CHBr_2^+$ and the CF_3^+ fragments. Furthermore, the combined decrease in $CHBr_2CO^+$ and $CHBr_2^+$ yields is equivalent to the increase in CF_3^+ yield – the sum of the three varies by less than 3%.

The ARP charge transfer model is supported by both the learning control and the pump-probe data but has not yet explained the widths of the peaks in the pump-probe data. We would like to know if the widths of the pump-probe ion yields arise due to a broad resonance, or due to a spatially broad wave packet sweeping past a narrow resonance. Our first hypothesis was that the widths correspond to the time during which the PES's are resonantly coupled by the laser pulse. To test this, we repeated the pump-probe measurements (see Fig. 6.2) with two different central frequencies (380 and 391 THz) for the probe pulse while limiting its bandwidth enough to nearly double its duration. Peak timings and widths for the $CHBr_2^+$ and CF_3^+ fragment yields in these two scans were similar to each other and to earlier pump-probe results with the full laser bandwidth. There were slight differences in the $CHBr_2CO^+$ peak, but these are difficult to analyze because of the long duration of this peak. Since analysis of the $CHBr_2CO^+$ fragment dynamics is not central to this

chapter (we are describing control over the $CF_3^+/CHBr_2^+$ ratios and the anti-correlation is most prevalent between the $CHBr_2^+$ and the CF_3^+ fragments) we will not concentrate on the differences seen in this ion signal.

Based on the $CHBr_2^+$ and CF_3^+ behavior we conclude that the widths of the pump-probe peaks are not limited by the laser bandwidth. Instead, they must be dictated by the spread of the dissociating wave packet as it crosses the resonance. Hence, the pump-probe data represents a measurement of the quantum mechanical probability density of the wave packet. Furthermore, the fact that the pump-probe peaks did not move by more than 50 fs with probe pulse tuning places a lower limit on the molecular chirp rate of $\sim$210 THz/ps.

If the spread of the wave function of the dissociating molecule does determine the width of the peaks in the pump-probe data, then increasing the duration of the probe pulse (to better match wave function spread) should increase the charge transfer — as long as the probe pulse has sufficient intensity to strongly couple the PES's and make the transition across the resonance adiabatic. To test this, we measured fragment yields as a function of probe pulse duration for two different probe energies.

Figure 6.6 shows the CF_3^+, $CHBr_2^+$, and $CHBr_2CO^+$ signals as a function of second order spectral phase ("chirp"). Probe pulse duration is related to

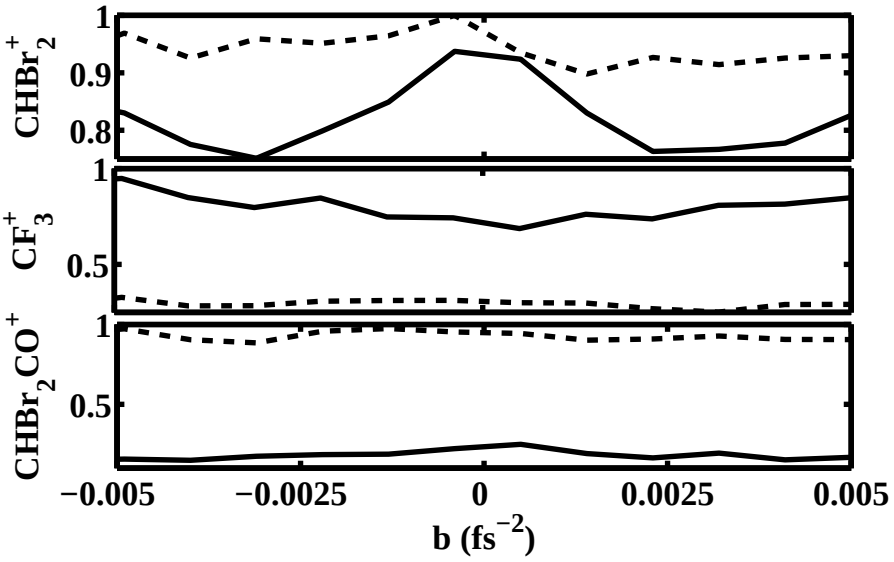

Figure 6.6 $CHBr_2^+$, CF_3^+, and $CHBr_2CO^+$ yields as a function of chirp parameter b where the temporal phase of the probe pulse, with central frequency ω_0, is $\phi(t) = \omega_0 t + bt^2$. Data are shown for the maximum probe pulse intensity (solid) and for lower intensity (dotted).

the chirp parameter, b, by

$$\tau = (2\ln(2)/\pi\Delta\nu)\sqrt{1 + b^2/a^2}\ ,$$

where $\Delta\nu$ is the laser bandwidth (15.8 THz), and $a = ln2/\tau_p^2$ (8.8×10^{-4} fs^{-2}) where τ_p is the transform limited pulse duration (28 fs). By adjusting the chirp to change the probe pulse duration we kept the probe pulse energy fixed and confirmed our lower bound for the molecular chirp rate by comparing the

charge transfer with positive and negative laser chirp. The pump-probe time delay was set to 280 fs (roughly the peak of the charge transfer process) and chirp rate was kept below 80 THz/ps to avoid overlap of the stretched probe pulse with the pump.

For a low probe energy ($\sim 50\mu$J), there is little variation in the fragment yields as a function of probe pulse duration. However, for a higher probe energy ($\sim 100\ \mu$J), the $CHBr_2^+$ and $CHBr_2CO^+$ ion signals go down with increasing probe pulse duration, while the CF_3^+ signal *increases* with increasing probe pulse duration. This is consistent with the pump-probe signal width being limited by the spread of the dissociative wave function. Only the portion of the wave function in the vicinity of the resonance *while the probe pulse is on* can be transferred between PES's.

Furthermore, while there is a slight asymmetry in the data with respect to positive and negative laser chirp, the lack of a substantial difference means that the molecular chirp rate must be much larger than the maximum probe laser chirp rate of 80 THz/ps. This is consistent with our earlier lower bound of 210 THz/ps. The slight asymmetry is consistent with the positive chirp making the passage more diabatic while the negative chirp makes the passage more adiabatic. A laser frequency sweep in the same direction of the molecular chirp should make the process further adiabatic, thereby enhancing charge

transfer.

By changing the molecule to include two bromine atoms on the other methyl group, we have seen that the control over the halogenated methyl ratio $CF_3^+/CHBr_2^+$ can be explained by a different mechanism that what was seen in controlling the methyl ratios in TFA and TCA. We have seen that a dynamic resonance leads to effective charge transfer that is mediated by adiabatic rapid passage.

The change in mechanism with the change in molecular structure is interesting. One explanation for this mechanistic change might lie in a reduced mass argument. The reduced mass of the CH_3CO and CF_3 and CCl_3 in TFA and TCA are 27 and 31 amu, respectively. In Br2TFA, the reduced mass of the $CHBr_2CO$ and CF_3 fragments is 51 amu. The larger reduced mass in Br2TFA would cause the vibrational period of the $C-C$ bond connecting them to be longer. This means that as the molecule begins to dissociate along this $C-C$ bond, the fragments will slowly separate from each other. This slow dissociation is what allows us to satisfy the adiabaticity condition needed for ARP, and charge transfer to occur. However, in TFA and TCA, the small reduced mass will allow the halogenated methyl fragments to quickly dissociate from the acetyl fragment. This fast dissociation will cause the two states responsible for charge transfer to diabatically pass through the central laser

energy, disallowing a charge transfer scenario. However, this allows a wave packet to then make it to the critical interfragment distance where enhanced ionization is possible. There has been work done on the diatomic ion I_2^{2+} that suggests that charge transfer may occur earlier than enhanced ionization [47]. As another test of this argument, we looked at the pump-probe ion yield of the molecule 3-dibromo-1,1,1-trifluoroacetone ($CH_2BrCOCF_3$, BrTFA). The results are shown in Figure 6.7. The reduced mass of this molecule is 44 amu.

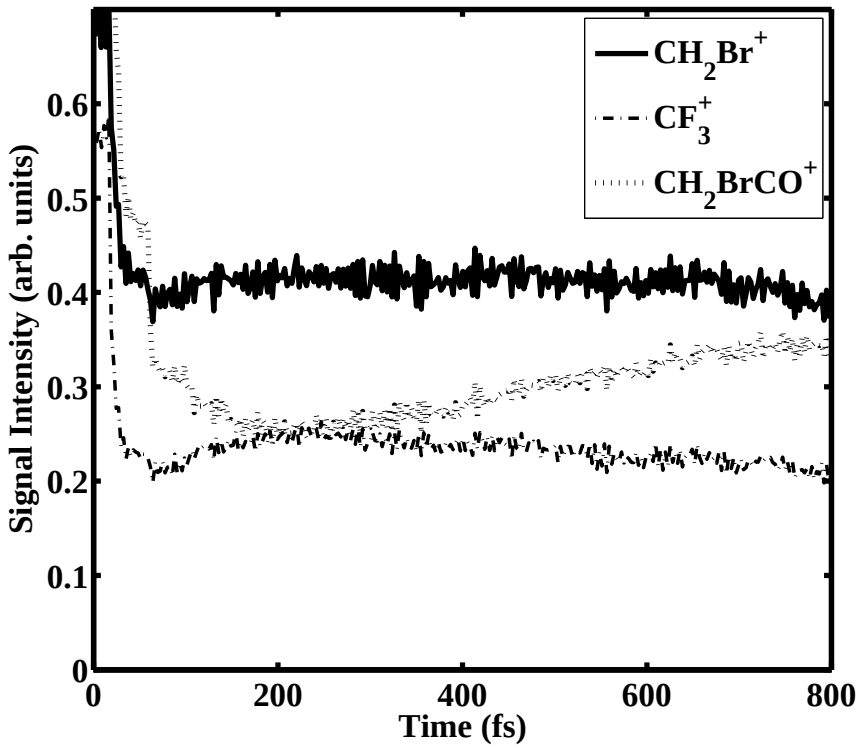

Figure 6.7 CH_2Br^+ (solid), CF_3^+ (dash-dot) and CH_2BrCO^+ (dashed) signals as a function of pump-probe delay. All yields are normalized to the CH_2BrCO^+ signal at zero time delay.

It is clear that there is an anticorrelation between the CH_2BrCO^+ and CF_3^+ fragments. It appears that at this reduced mass, the evolution of the system is still slow enough to satisfy the adiabaticity condition. It is not yet known what the critical reduced mass marks the line between the phenomena of enhanced ionization and charge transfer. In fact, we do see evidence that this line may not exist, but that the change from enhanced ionization to charge transfer may be a smooth transition. Although not shown, the CH_3CO^+ fragment in TCA shows a hint of anticorrelation with $CClk$ peak. While this is an extremely small signal, it may mean that we are starting to see the change in mechanism from enhanced ionization and charge transfer.

We have found that while the control mechanism changed from enhanced ionization to charge transfer, we were still capable of performing tests that led to an understanding of the control mechanism. We used the same tools that have been available to us and that have proven invaluable for obtaining information about the molecular dynamics responsible for control: analysis of the optimal control pulse, pump-probe spectroscopy and intensity scans. These tools have also allowed us to develop an initial hypothesis for why we see a change in the control mechanism. Future work will concentrate on investigating this interesting regime where enhanced ionization gives way to charge transfer.

An interesting outcome that has arisen from the control experiments on Br_2TFA is that the pump-probe spectroscopy appears to indicate that we are measuring the quantum mechanical probability density of the dissociative nuclear wave packet. We investigate the possibility of measuring the dissociative wave function of the molecule. We discuss this in the next chapter.

Chapter 7

Wavefunction Measurement

Our work on controlling fragmentation of Br2TFA, which we discussed in Chapter 6, has produced interesting results that have led us down a different experimental direction. In Chapter 6 we discussed how the width of the CF_3^+ pump-probe ion yield (see Fig. 6.2) was not due to a broad resonance, but is due to a spatially broad wave packet passing through a dynamic resonance.

This led us to see whether we could interpret our results as being a measure of the quantum mechanical probability distribution of the dissociating wavefunction, $|\psi(t, R_0)|^2$. If this is the case, we would like to make a full measurement of this wavefunction. That would entail also obtaining phase information about the wavefunction.

Measurements of molecular wavefunctions have been reported, for both electronic and vibrational wavefunctions in diatomic molecules [48, 49, 50].

These techniques relied on quantum state tomography [49]. While this technique is highly effective, it becomes difficult to implement when one is working with polyatomic molecules. In our case, we are only making measurements of ions in a TOFMS. This means that the measurement will only be along one dimension, that of the dissociation coordinate. However, a measurement of the wavefunction could yield important information about the shape of the PES on which the wave packet is evolving along the dissociation coordinate. Measurements of these dissociating wave functions could serve as valuable tools for understanding the shapes of PES's in complicated polyatomic molecules. They will also provide us with realtime "movies" of the molecule dissociating.

Figure 7.1 shows the ion yields for both the $CHBr_2^+$ and the CF_3^+ again for reference. The ion yields for these fragments show strong a anticorrelation at times beginning at $\sim$ 200 fs and lasting for $\sim$ 1 ps. It was found in Chapter 6 that charge transfer was responsible for the observed signals. [51]. Figure 7.2 illustrates the pathway for charge transfer. The pump pulse ionizes the molecule, launching a nuclear wave packet from the ground state potential energy surface (PES 1) onto an ionic dissociative PES (PES 2), which leads to fragmentation producing $CHBr_2^+$ and CF_3. The wave packet evolves on PES 2, where it is subsequently excited to PES 3 at some time t later by the probe pulse. PES 3 leads to fragmentation producing $CHBr_2$ and CF_3^+. It was dis-

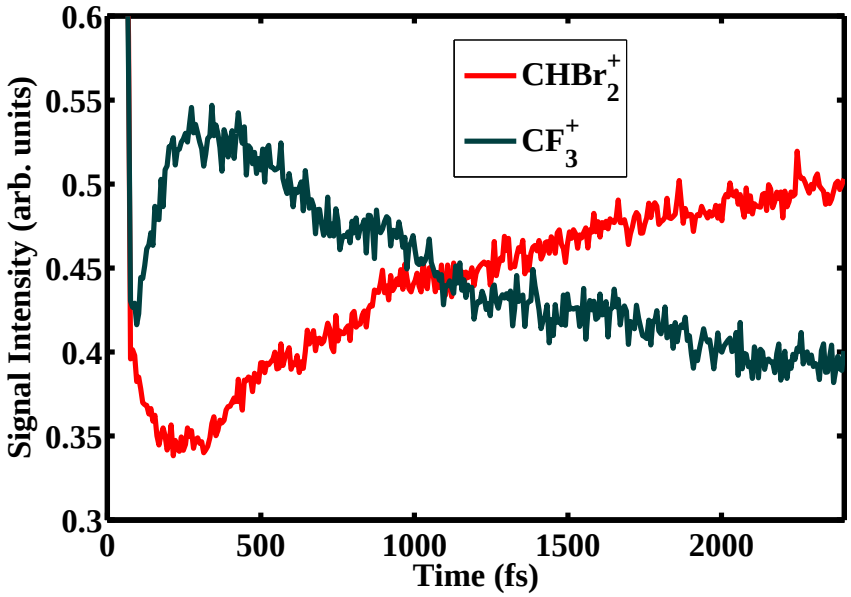

Figure 7.1 $CHBr_2^+$ (red) and CF_3^+ (black) signals as a function of pump-probe delay. The yields are normalized to the CF_3^+ signal at zero time delay.

cussed in Chapter 6 that the width of the wave packet was responsible for the long temporal dynamics seen in Fig. 7.1. As the wave packet passes through the resonance between PES 2 and PES 3, a fraction of it is promoted to PES 3. Because the probe pulse in these experiments is short, we believe that we are only promoting a small "slice" of a spatially broad wave packet to PES 3 as it passes through the resonance at the critical inter-fragment distance, $r = R_0$. This data leads us to believe that the enhancement seen in the CF_3^+ is the quantum mechanical probability distribution of the dissociative wave packet on PES 2 at the critical inter-fragment distance where ARP occurs. It should be noted that while the fragment signals seen in Fig. 7.1 are highly anticorre-

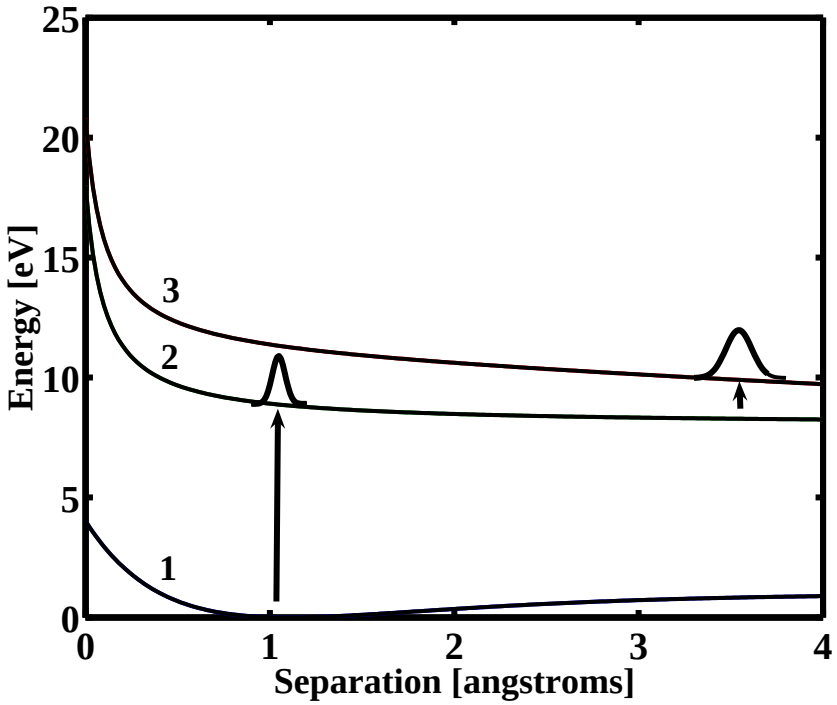

Figure 7.2 Simplified cartoon of hypothetical potential energy surfaces involved in the charge transfer control mechanism.

lated, they are not perfectly anticorrelated. This is because some of the wave packet created on PES 2 is launched to another PES during the probe pulse interaction. This is seen in modulations of the other fragments $CHBr^+$ and CH^+.

The enhancement seen in the CF_3^+ ion yield in Fig. 7.1 provides a measure of $|\psi(r;t)|^2$. However, to obtain complete knowledge of the dissociating wave function, we also have to measure $\phi(r;t)$. One way to obtain the phase of this dissociative wavefunction is to interfere two separate wave packets on PES 2. This is done by using two pump pulses, separated by a time τ, which is shorter

than the time it takes for the initial enhancement to be seen in the pump-probe ion signals. Then we can come in with the third probe pulse, exciting the total wave packet onto PES 3 at some time t later. The measurement of the total wave packet on PES 3 will give us an interferogram of the wave packet.

Mathematically, we can represent the wave packet being created on PES 2 as

$$\psi(r;t)_{\text{total}} = \psi(r;t) + b\psi(r;t-\tau) \ , \tag{7.1}$$

where b in Eq. 7.1 allows for the case where the two wave packets are not identical in amplitude. At a time t which is later than the pump-pump delay τ, we measure the quantum mechanical probability distribution of interfering wave packets,

$$|\psi(r;t)_{\text{total}}|^2 = |\psi(r;t)|^2 + b^2\,|\psi(r;t-\tau)|^2 + 2b\,\text{Re}\left\{\psi^\star(r;t)\psi(r;t-\tau)\right\} \tag{7.2}$$

by promoting the total wave packet onto PES 3. At the critical inter-fragment distance, R_0, where the charge transfer occurs, Eq. 7.2 becomes

$$\begin{aligned} |\psi(R_0;t)_{\text{total}}|^2 &= |\psi(R_0;t)|^2 + b^2\,|\psi(R_0;t-\tau)|^2 \\ &+ 2b\cos\left(\phi(t-\tau)-\phi(t)\right)\,|\psi(r;t)|\,|\psi(r;t-\tau)| \ . \end{aligned} \tag{7.3}$$

It is seen from Eq. 7.4 that all of the information about the wave packet is in the measurement. We only have to make a measurement of the two wave packets individually, similar to that of the single pump-probe experiments, to measure the terms $|\psi(R_0;t)_{\text{total}}|^2$ and $b^2\,|\psi(R_0;t-\tau)|^2$. Once this is done, we can subtract these terms from Eq. 7.4, and divide to get a normalized phase difference term,

$$S_1(t,\tau) = \cos\left(\phi(t-\tau) - \phi(t)\right) \ . \tag{7.4}$$

The argument of Eq. 7.4 gives us the phase difference between the wave packets at time t and time $t+\tau$. Integration yields the phase at the inter-fragment distance R_0.

The treatment above only considers the portion of the total nuclear wave-functions. However, the electronic portion of the wavefunction cannot be ignored. With each pump pulse we are only *partially* ionizing the molecule. This partial ionization acts to create an entangled molecular wave function where the nuclear and electronic portions of the wave function are no longer separable. Because of this, our treatment of the interference has to take into account the electronic portion of the molecular wave function. In the case where a single pump pulse ionizes a valence electron, giving it an energy ε, the

total molecular wavefunction can be expressed as

$$\Psi_{\text{total}} = \theta_{\text{neutral}}(t)\psi_{\text{bound}}(t) + \chi_{\varepsilon}(t)\theta_{\text{ion}}(t)\psi_{\text{diss}}(t) \ , \tag{7.5}$$

where $\theta_{neutral}$ and θ_{ion} are the ground neutral and ionic nuclear wavefunctions respectively. The normalization of the nuclear wavefunctions is such that $|\langle\psi_{\text{diss}}|\psi_{\text{diss}}\rangle|^2$ produces the probability that the molecule dissociates. Eq. 7.5 takes the wave function at a single place in space, so that we can concentrate on the temporal dynamics. For convenience, we define

$$\Psi_{\text{diss}}(t) = \chi_{\varepsilon}(t)\theta_{\text{ion}}(t)\psi_{\text{diss}}(t) \tag{7.6}$$

as the dissociative part of the total wave function and

$$\Psi_{\text{bound}}(t) = \theta_{\text{neutral}}(t)\psi_{\text{diss}}(t) \tag{7.7}$$

as the bound part of the total wave function. Following a single pump pulse the total wave function can then be written as

$$\Psi_{\text{total}} = \Psi_{\text{bound}} + \Psi_{\text{diss}} \ . \tag{7.8}$$

If we take into account two pump pulses, then the wavefunction can be expressed as

$$\Psi_{\text{total}}(t) = \Psi_{\text{bound}} + \Psi_{\text{diss}}(t) + \Psi_{\text{diss}}(t+\tau). \tag{7.9}$$

The TOFMS measures only ionic fragments. Because of this, concentrate on the ionic, dissociative portion of the wavefunction. This portion of the wavefunction can be expressed as

$$\Psi_{\text{disstotal}}(t) = \chi_{\varepsilon}(t)\theta_{\text{ion}}(t)\psi_{\text{diss}}(t) + \chi_{\varepsilon}(t+\tau)\theta_{\text{ion}}(t+\tau)\psi_{\text{diss}}(t), \tag{7.10}$$

which will lead to the measurement probability of an ion,

$$\begin{aligned} P_{\text{ion},\varepsilon} &= \left|\chi_{\varepsilon}(t)\theta_{\text{ion}}(t)\psi_{\text{diss}}(t)\right|^2 + \left|\chi_{\varepsilon}(t+\tau)\theta_{\text{ion}}(t+\tau)\psi_{\text{diss}}(t+\tau)\right|^2 + \\ &\quad 2\left|\chi_{\varepsilon}(t)\theta_{\text{ion}}(t)\psi_{\text{diss}}(t)\right|\left|\chi_{\varepsilon}(t+\tau)\theta_{\text{ion}}(t+\tau)\psi_{\text{diss}}(t+\tau)\right|\cos\left(\Delta\phi_d + \Delta\phi_i\right). \end{aligned} \tag{7.11}$$

where $\Delta\phi_i$ and $\Delta\phi_d$ are the electronic and nuclear phase differences

$$\Delta\phi_d = \phi_d(t) - \phi_d(t+\tau) \text{ and } \Delta\phi_i = \phi_i(t) - \phi_i(t+\tau) \tag{7.12}$$

that are associated with nuclear and electronic parts of the wave function

$$\chi_{\varepsilon}(t)\theta_{\text{ion}}(t) = \left|\chi_{\varepsilon}(t)\theta_{\text{ion}}(t)\right| e^{i\phi_i(t)} \text{ and } \psi_{\text{diss}}(t) = \left|\psi_{\text{diss}}(t)\right| e^{i\phi_d(t)}\ . \tag{7.13}$$

The probability given in Eq. 7.11 is for measurement of a fragment correlated with an electron with energy ε. However, our measurement averages over ε. In this case, the probability in Eq. 7.11 becomes an integral,

$$\begin{aligned} P_{\text{ion}} &= \int d\varepsilon \quad |\chi_\varepsilon(t)\theta_{\text{ion}}(t)\psi_{\text{diss}}(t)|^2 + |\chi_\varepsilon(t+\tau)\theta_{\text{ion}}(t+\tau)\psi_{\text{diss}}(t+\tau)|^2 + \\ &\qquad 2\,|\chi_\varepsilon(t)\theta_{\text{ion}}(t)\psi_{\text{diss}}(t)|\,|\chi_\varepsilon(t+\tau)\theta_{\text{ion}}(t+\tau)\psi_{\text{diss}}(t+\tau)|\cos\left(\Delta\phi_d + \Delta\phi_i\right). \end{aligned} \tag{7.14}$$

From Eq. 7.14, it is clear that integration over ε will cause a damping of the interference as each χ_ε will have its own distinct phase evolution. We investigated what happens to this term if we were to integrate over a Gaussian distribution of photoelectron energies,

$$P(\varepsilon) = \sqrt{\frac{\alpha}{\pi}}\, e^{-\alpha(\varepsilon-\varepsilon_0)^2}. \tag{7.15}$$

The result of the integration is that of multiplying Eq. 7.11 by a Gaussian function of the pump-pump delay τ,

$$\begin{aligned} P_{\text{ion}} &= |\chi_\varepsilon(t)\theta_{\text{ion}}(t)\psi_{\text{diss}}(t)|^2 + |\chi_\varepsilon(t+\tau)\theta_{\text{ion}}(t+\tau)\psi_{\text{diss}}(t+\tau)|^2 + \\ &\qquad 2e^{-\tau^2/(4\hbar^2\alpha)}\,|\chi_\varepsilon(t)\theta_{\text{ion}}(t)\psi_{\text{diss}}(t)|\,|\chi_\varepsilon(t+\tau)\theta_{\text{ion}}(t+\tau)\psi_{\text{diss}}(t+\tau)|\cos\left(\Delta\phi_d + \Delta\phi_i\right). \end{aligned} \tag{7.16}$$

This leads to a normalized phase term

$$S_1(t,\tau) = \Gamma cos\left(\Delta\phi_d + \Delta\phi_i\right) \tag{7.17}$$

where

$$\Gamma = e^{-\tau^2/(4\hbar^2\alpha)}. \tag{7.18}$$

Figure 7.3 plots the results Eq. 7.16. It is evident from from this figure that

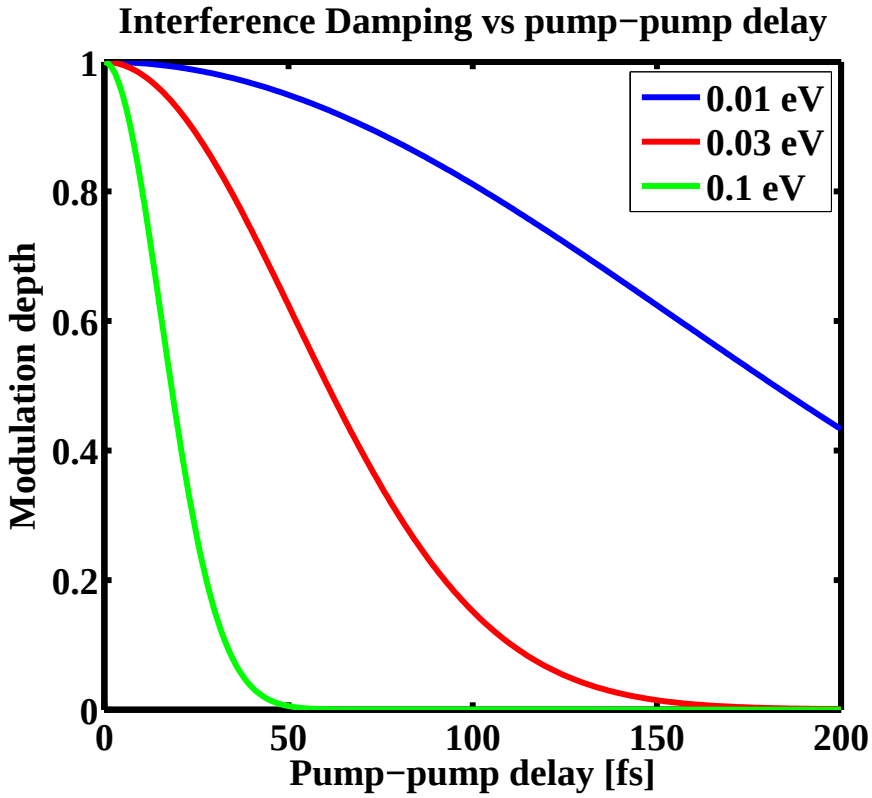

Figure 7.3 Plot showing how width of photoelectron distribution and pump-pump delay, τ, can damp the interference between two wave packets.Note that we expect that our initial measurements will have photoelectron distributions between 10 and 30 meV.

as τ increases, the width of the photoelectron energy distribution needed to resolve the interference needs to be narrow. So, what we want to perform our measurement with short time delays and narrow photoelectron distributions. Another way to reducing the effects of damping is to correlate electron energy with the ionic fragment energy. This will eliminate the integral in Eq. 7.14, thereby eliminating the effect of damping. However, we do not currently have the capability of measuring both positive ions and electrons in a correlated measurment. Another way of reducing the number of electronic states that we have to integrate over is to lower the intensity of our pump pulses. This will minimize the dynamic Stark broadening. This means that our experiments should be performed in the low intensity, multiphoton ionization limit. To reach this limit, we set our pump pulse intensities so that minimal ionization signal was present, which corresponds to intensities of $\sim 7{\times}10^{13}$ W/cm^2.

Figure 7.4 shows CF_3^+ ion yield for a wave packet interference experiment taken with $\tau = 30$ fs pump-pump delay. The black curve in this figure represents the coherent sum of two wave packets that are launched on PES 2 as measured by a pump-pump probe experiment. The red curve is the sum of two single pump-probe measurements, representing an incoherent sum of the wave packets. It is clear from Fig. 7.4 that the coherent sum has a larger signal level than that of the incoherent sum. This is evidence that we are

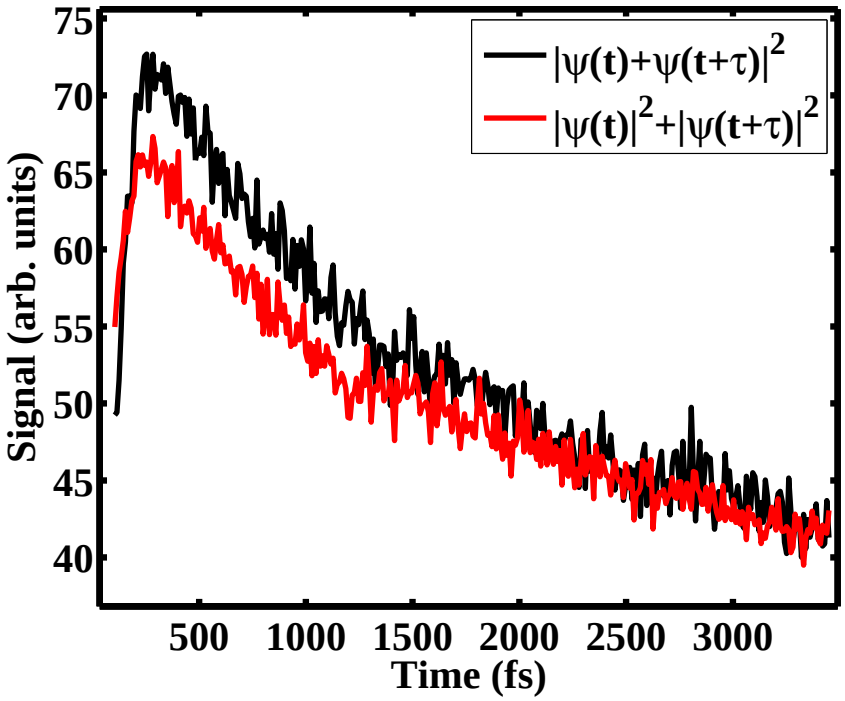

Figure 7.4 The black line shows the CF_3^+ ion yield for two wave packets being launched on PES 2. The red line shows the results of two individual pump-probe experiments being added together. Note that the black curve has a large signal, indicating that the interference is being measured.

indeed measuring interference of the wave packets. Using this result, we can reconstruct the phase of the wavefunction. This result is shown in Figure 7.5. The phase difference shown in Fig. 7.5 only encompasses the times that the two signals in Fig. 7.4 show interference. We ignore the long and very short delay times as the wave packets have little signal in their tails. It is interesting to note that the phase difference is largely linear. We performed wave packet calculations on a modified version of the relaxed ionic state curve for trichloroacetone (see Fig. 5.1(a)). The results of these calculations show that

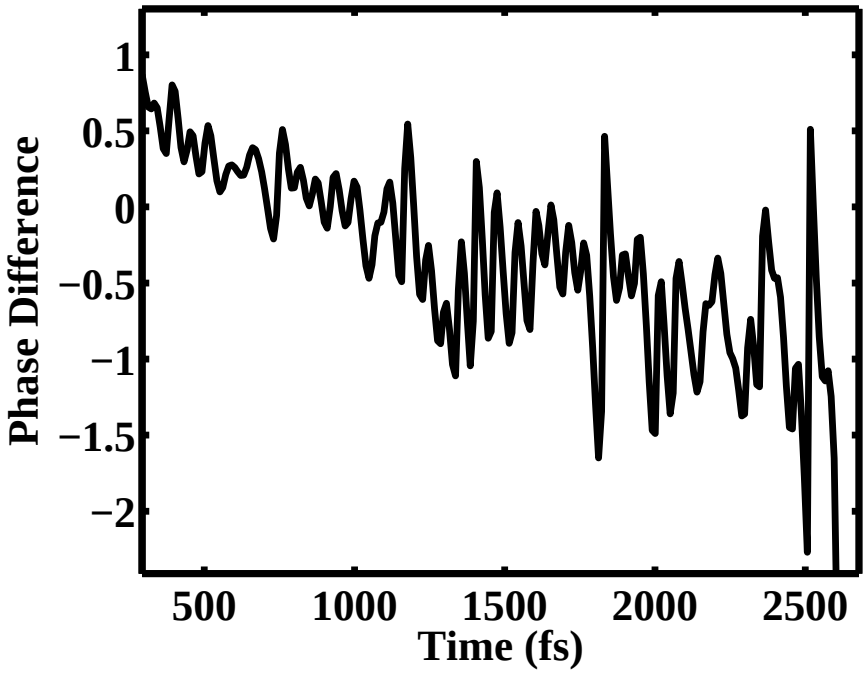

Figure 7.5 Reconstruction of the phase of the wavefunction from the data shown in Fig. 7.4.

a wave packet evolving on this PES will have largely quadratic phase. These results lead us to expect largely quadratic phase in our measurements. The derivative of quadratic phase is a linear function of time. While we have not yet generated PES's for the Br2TFA case yet, we have reason to believe that the wave packet evolving on PES 2 in Br2TFA will behave similarly to the wave packet in our calculations. The noise in the phase difference signal increases with time. This is due to the fact that the difference between the two signals in Fig. 7.4 is approaching zero at longer time delays. In fact, the noise in the phase difference signal is an artifact of the noise in our pump-pump-probe

data. The phase should be a smoothly varying function.

The measurement shown in Fig. 7.4 was performed with a pump-pump delay of 30 fs in attempt to beat the damping effects shown in Fig. 7.3. This time delay is shorter than the time durations of our pump pulses (33 fs). Because of this, we have to consider optical interference as a limiting factor in the experiment. To limit the effects of optical interference, we performed the experiment by adjusting the phase relationship between the two pump pulses to be $\pi/2$ [47]. This method helps to keep the overall energy of the double pulses constant for all time delays. The two pump pulses are generated in our optical pulse shaper. Using the pulse shaper to make the two pump pulses has the advantage of allowing us to have two phase locked pulses, without having to build a complicated interferometer that keeps the phase between two pulses locked [50]. This method also permits independent control over both the time delay and relative carrier phase between the two pulses, thereby allowing us to produce pulse pairs with arbitrary phase relationship at any given time delay. Alternatively, it can produce pulses with arbitrary time delays with a given phase relationship [6].

We used SHG FROG to measure the phase relationship between the pump pulses, as well as monitored the energy of the two pulses. With a $pi/2$ phase relationship, the energy of the double pulse should be constant for all time

delays.

In order to determine what portion of the raw coherent signal is a result of optical interference, we set the pump-pump delay to be 30 fs, and scanned the phase of the first pulse through 2π radians. Figure 7.6 shows the result of this experiment. The large modulations in all fragment yields are largely

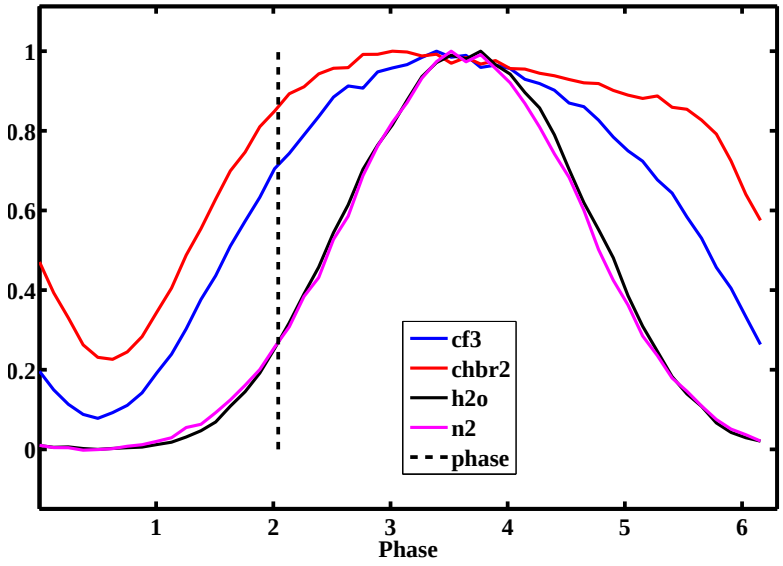

Figure 7.6 Ion yields as a function of phase between the two pump pulses. The black vertical dotted line is where we have determined a $\pi/2$ phase relationship between the two pump pulses to be. This is the phase that we took the data seen in Fig. 7.4

due to optical interference. The signal shapes of the N_2^+ and the H_2O^+ also indicate that a higher order process is responsible for the ionization, as the curves appear to be the shape of a sinusoid taken to a higher power. The vertical black dotted line in Fig. 7.6 marks the phase where we took the data

seen in Fig. 7.4. Note that it is $\pi/2$ radians from the peak of the N_2^+ and H_2O^+ ion signals. We choose these signals because they display the effects of the optical interference cleanly. The CF_3^+ and $CHBr_2^+$ ion yields in Fig. 7.6 (blue and red, respectively) have different shapes. It appears as if the these two fragments are saturating. They also do not show the full depth of modulation like the nitrogen and water peaks.

While working at a phase relationship of $\pi/2$ between the two pump pulses limits optical interference, it does not completely eliminate it. The data shown in Fig. 7.4 was processed to eliminate any effects of optical interference. The raw data showed that the CF_3^+ ion yield for the coherent sum was always larger than the ion yields for the incoherent sums. To eliminate any optical effects, we analyzed the $CHBr_2^+$ ion yield as a function of intensity. We look at this fragment because the wave packets are launched onto PES 2, which produces $CHBr_2^+$. We then fit this data to a log-log line, to determine the multiphoton order for making $CHBr_2^+$. We can then use this number to calculate how much wave packet is created by optical interference. This gives us an optical factor. We then divide the coherent CF_3^+ signal by this optical factor to remove any wave packet signal due to optical interference. We then shift the coherent signal down so that the asymptotic values of the ion yields of the coherent and incoherent signals are equal, assuming that the wave packet goes to zero

amplitude for long time delays. This step was done assuming that the offset between the coherent and the incoherent signal was due to background CF_3^+ measured from other PES's (not PES 3).

The results of this preliminary experiment show promise for the idea of measuring dissociative wave functions in polyatomic molecules. We chose to work with Br2TFA in this case because the charge transfer mechanism relies on a single photon process. However, we have reason to believe that we can use this same method to measure wave functions where the control mechanism is a multiphoton process. This means that we should be able to make wavefunction measurements in any molecule where we can transfer between different charge states or fragments in a pump-probe measurement.

For instance, we saw in Chapters 4 and 5 that the CF_3^+ and CCl_3^+ pump-probe ion yields, in TFA and TCA respectively, showed a similar enhancement to what is seen in Fig. 7.1. We have reason to believe that in both of these molecules the pump-probe ion yields of CF_3^+ and CCl_3^+ represent a measure of $|\psi(t)|^2$. In both cases, the probe pulse launches a wave packet onto a state where the halogenated methyl fragments are measured by enhanced ionization, which is multiphoton event. What makes these molecules particularly interesting for this measurement is that we have one dimensional potential energy surfaces calculated for them (see Fig. 4.11 for TFA and Fig. 5.1(a) for TCA).

Using these calculated potentials we have already made wave packet calculations which tell us what the wavefunction shape is. In the case of TFA, the shape of the wave packet from the calculations matches well with the shape seen in the pump-probe ion yield of CF_3^+ (see Figs. 5.5(a) and the red curve in Fig. 5.9).

There are technical issues with making the wave packet interference in these molecules. For instance, the turn on time for the wave packet occurs around 100 fs for both TFA and TCA, which is faster than that seen in the Br2TFA. This means that we will have to continue to work at short pump-pump delays to avoid the second pump pulse from acting like a probe. We also have to worry about the strong probe needed for enhanced ionization creating background fragments due to other processes, as the intense probe pulse can independently ionize both TFA and TCA. These are experiments that will be carried out in the future.

These experiments can be made easier by implementing improvements to experimental apparatus. For instance, our lab has just constructed a new filamentation chamber that will allow us to take our 33 fs pulses down to 16 fs [52]. This will allow us to reach shorter pump-pump delays, which are needed to eliminate damping of the interference without having to worry about optical interference. Future plans also include making a detection system that

can detect both electrons and positive ions. This will allow us to make a correlation between electron energy and ion fragment energy. This will cause the integral in Eq. 7.14 to collapse, completely eliminating any damping of the interference.

In these experiments, we relied on a multiphoton transition to get us to the first ionized state, PES 2. However, we would like to work in a single photon, weak field regime. To work in this regime, we need to be able to make UV light. Our lab already has the capability of making high energy, compressed ultrafast UV pulses [53]. However, we would also like to be able to shape these UV pulses. To do this, we have made plans to construct a UV pulse shaper. This will allow us the capability of producing two UV pulse pairs. We will also have the ability to do two color pump-pump experiments.

In this chapter, we have shown that it is feasible to measure dissociative wavefunctions along the dissociation coordinate in polyatomic molecules. The measurements shown in this chapter are preliminary but promising. The techniques used to measure the wavefunction in Br2TFA in this chapter are general techniques, and can be used to measure wavefunctions in any molecule where we can measure a transfer between different charge or fragment states.

Chapter 8

Conclusion and Future Directions

The work presented in this thesis has demonstrated that it is not only possible to control molecular dynamics using closed-loop learning control, but it is also possible to understand the solutions that the learning control process yields. It was shown in Chapter 4 for TFA, that we were able to understand the control mechanism responsible for controlling the CF_3^+/CH_3^+ ratio. This led to the development of a model which allowed us to predict the outcome of control experiments in TCA and TDA, which were discussed in Chapter 5. With the ability to predict the outcome of these control experiments, one can start to think of the shaped ultrafast laser pulses as "photonic reagents".

In Chapter 6, we explored the question of what would happen if we were to alter the molecule by taking two hydrogens off the methyl group and replacing them with bromine atoms. By balancing the halogens in this halogenated ace-

tone, we were able to see the control mechanism that controlled the fragment ratio $CF_3^+/CHBr_2^+$ change from enhanced ionization, which was seen in TFA and TCA, to charge transfer in Br2TFA. Using parts of the model we had developed for the enhanced ionization control mechanism in TFA, we were able to understand the mechanism for control.

Our efforts to understand the mechanism responsible for control in these molecules opened up other interesting opportunities for understanding control of molecular dynamics. It was shown in Chapter 6 that the pump-probe measurements of Br2TFA yielded the quantum mechanical probability density of the dissociating wavefunction. With the capability of measuring $|\psi(t, R_0)|^2$, we then looked into the possibility of making a full measurement of the wavefunction, which entailed measuring the phase, $\phi(t)$, of the wavefunction. To do this, we launched two wave packets on the dissociative potential energy surface. Then we relied on a measurement of the wave packet interference. This measurement allowed us to reconstruct the phase of the wavefunction. While these results are preliminary, they show that this method for measuring dissociative wavefunctions in other polyatomic molecules is promising. The only requirement is that a wave packet passes through a dynamic resonance. We have seen in Chapters 4 and 5 for the cases of TFA and TCA that molecules undergo enhanced ionization at critical inter-fragment distances. This process

happens via a dynamic resonance. We have performed experiments on other molecules that show evidence of a wave packet passing through a dynamic resonance. Pump-probe ion yields for fragments of the molecule $CHBr_2Cl$ are shown in Figure 8.1.

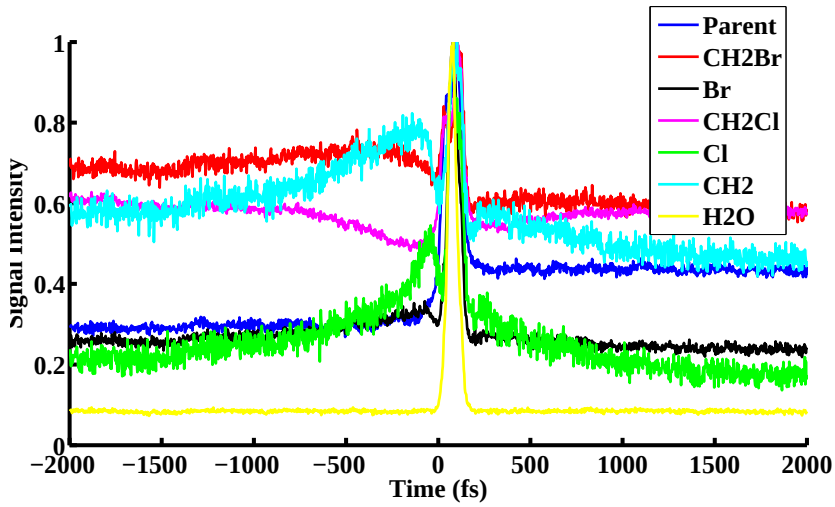

Figure 8.1 Pump-probe ion yields for fragments from bromochloromethane. Note the enhancements and anticorrelated behavior of some of the fragments that is similar to what was seen in Br2TFA and BrTFA.

There is still one interesting fact about these learning control experiments that we have not addressed. In all cases, we were trying to *selectively* break the $C-C$ bonds in the halogenated acetones. However, we never actually demonstrate bond selective chemistry. In TFA and TCA, intensity scan data and molecular structure calculations show that the molecules were unstable to dissociation after ionization. In both cases, after ionization, the molecule dissociated into CH_3CO^+ and CF_3^+ or CCl_3^+. This means that control was

over ionization rather than dissociation. We had very little control over breaking the $C-C$ bond which would lead to an increase in the desired methyl fragment. The case is the same in Br2TFA. Although we were able to control the molecular dynamics, we still have not achieved the "holy grail" of coherent control–selective bond breaking.

This leads us to ask the following question–is it possible to perform bond selective chemistry using shaped, ultrafast laser pulses? To answer this question, we began work on a different set of molecules, the halomethanes (CH_2BrX, where X is either Br or Cl). These molecules have the property that some of the fragments actually have lower ionization potentials than the molecule itself. We feel that the one important aspect to achieving the goal of bond selective chemistry lies in the ability to dissociate the molecule in a bound electronic state, i.e. perform neutral dissociation. Using these molecules, we performed two pulse experiments where the first pulse dissociates, and the second pulse ionizes. Figures 8.2 and 8.3 show preliminary results from these experiments.

In both of these figures, the data was taken in a pump-probe configuration with a constant time delay between the two pulses. The first pulse in time was made to be weak, so that very little ion signal was present in the TOFMS. This pulse was designed to mainly dissociate the molecule. The second pulse

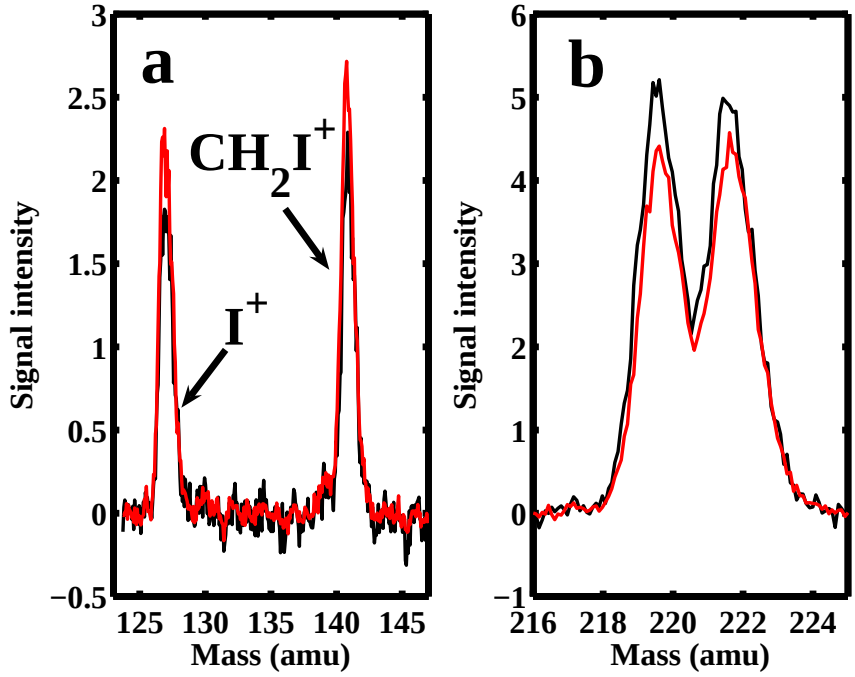

Figure 8.2 (a) CH_2I^+ and (b) CH_2BrI^+ ion signals taken with a constant pump-probe delay of 2 ps, with the first pulse being weak, and the second pulse being strong. The red curve was taken with both pulses on simultaneously (cooperative) and the black curve is the sum of two spectra taken with each pulse separately (uncooperative).

in time was made more intense so that it could ionize the fragments. The idea of the experiment is that when both pulses act cooperatively, then the dissociation pulse will create neutral fragments, which are subsequently ionized by the second pulse. This data is represented by the red curve in Figs. 8.2 and 8.3. The black signal in the figures is the sum of two traces taken with the two pulses acting independently, or non-cooperatively. It is clear from both figures that in the case of some fragments, when the pulses act cooperatively, that their ion yield increases, at the expense of the parent ion. These results

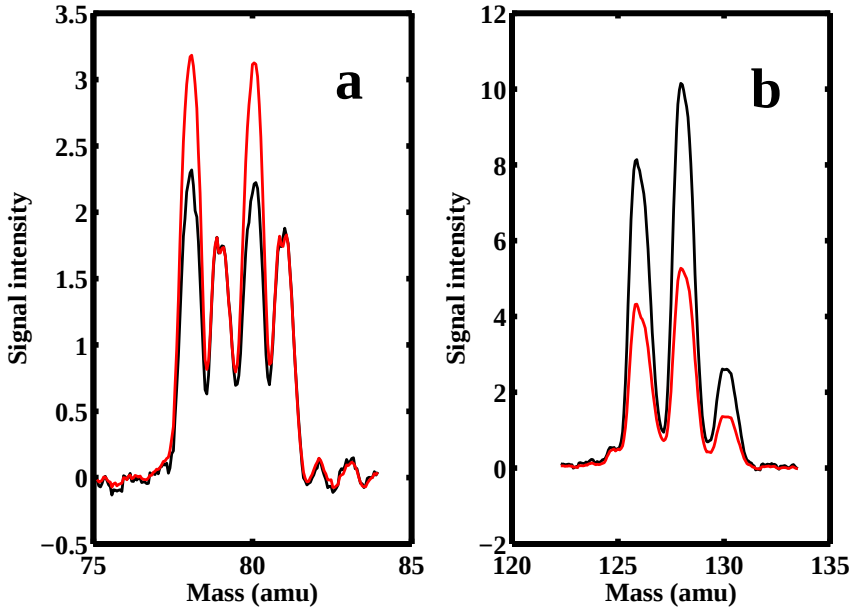

Figure 8.3 (a) Br^+ and (b) CH_2BrCl^+ taken in the same manner as the data shown in Fig. 8.2.

show that their might be a bound, dissociative electronic state that we can access.

The preliminary results on the halomethanes show that neutral dissociation is possible. These results show promise for the ability for us to attain the goal of bond selective chemistry. However, while we have not been successful at specifically breaking bonds, we have been successful at coherently controlling molecules to achieve a desired state. Future experiments will include methods such as closed-loop learning control in a pump-probe configuration, where the pump pulse can be optimally shaped to dissociate the molecule, and the probe will act as an ionizing pulse.

This thesis has shown that it is possible to understand solutions obtained from learning control. We have seen that a wave packet description of control is a powerful method for understanding control mechanisms. The wave packet description of control allows us to understand control in terms of dynamic resonances. These dynamic resonances are general and apply to nearly all molecules. While the work presented here relied on dynamic resonances on ionic states, future work will look to exploit dynamic resonances in bound electronic states.

Bibliography

[1] Warren, W., Rabitz, H., and Dahleh, M. *Science* **259**, 1581 (1993).

[2] Tannor, D. J., Kosloff, R., and Rice, S. A. *J. Chem. Phys.* **85**(10), 5805–5020 (1986).

[3] Brumer, P. and Shapiro, M. *Chem. Phys. Lett.* **126**(6), 541–546 (1986).

[4] Zhu, L., Kleiman, V., Li, X., Lu, S. P., Trentelman, K., and Gordon, R. J. *Science* **270**(5233), 77–80 (1995).

[5] Weiner, A. M. *Prog. Quant. Electr.* **19**, 161–237 (1995).

[6] Tull, J. X., Dugan, M. A., and Warren, W. S. *Adv. Magn. Opt. Res.* **20**, 1–50 (1997).

[7] Judson, R. S. and Rabitz, H. *Phys. Rev. Lett.* **68**(10), 1500–1503 (1992).

[8] Bardeen, C. J., Yakovlev, V. V., Wilson, K. R., Carpenter, S. D., Weber, P. M., and Warren, W. S. *Chem. Phys. Lett.* **280**, 151–158 (1997).

[9] Assion, A., Baumert, T., Bergt, M., Brixner, T., Kiefer, B., Seyfried, V., Strehle, M., and Gerber, G. *Science* **282**, 919–922 (1998).

[10] Hornung, T., Meier, R., Zeidler, D., Kompa, K. L., Proch, D., and Motzkus, M. *App. Phys. B* **71**(3), 277–284 (2000).

[11] Štefan Vajda, Bartelt, A., Kaposta, E.-C., Leisner, T., Lupulescu, C., Minemoto, S., Rosendo-Francisco, P., and Wöste, L. *Chem. Phys.* **267**, 231–239 (2001).

[12] Levis, R. J., Menkir, G. M., and Rabitz, H. *Science* **292**, 709–713 (2001).

[13] Weinacht, T. C., Bartels, R., Backus, S., Bucksbaum, P. H., Pearson, B., Geremia, J. M., Rabitz, H., Kapteyn, H. C., and Murnane, M. M. *Chem. Phys. Lett.* **344**, 333–338 (2001).

[14] Cardoza, D., Langhojer, F., Trallero-Herrero, C., Monti, O. L. A., and Weinacht, T. *Phys. Rev. A* **70**, 053406 (2004).

[15] Daniel, C., Full, J., González, L., Lupulescu, C., Manz, J., Merli, A., Štefan Vajda, and Wöste, L. *Science* **299**, 536–539 (2003).

[16] Bartels, R. A., Murnane, M. M., Kapteyn, H. C., Christov, I., and Rabitz, H. *Phys. Rev. A* **70**, 043404 (2004).

[17] Cardoza, D., Baertschy, M., and Weinacht, T. *J. Chem. Phys.* **123**, 074315 (2005).

[18] Cardoza, D., Baertschy, M., and Weinacht, T. *Chem. Phys. Lett.* **411**, 311–315 (2005).

[19] Backus, S., III, C. G. D., Murnane, M. M., and Kapteyn, H. C. *Review of Scientific Instruments* **69**(3), 1207–1223 (1998).

[20] Trebino, R., DeLong, K. W., Fittinghoff, D. N., Sweetser, J. N., Krumbugel, M. A., Richman, B. A., and Kane, D. J. *Rev. Sci. Instrum.* **68**(9), 3277–3295 (1997).

[21] Nuernberger, P. and Weinacht, T. C. *Design and Construction of an Apparatus for the Neutral Dissociation and Ionization of Molecules in an Intense Laser Field.* PhD thesis, Stony Brook University, (2003).

[22] Cohen, M. *private communication* (2006).

[23] Zeidler, D., Frey, S., Kompa, K.-L., Proch, D., and Motzkus, M. *Phys. Rev. A* **64**, 023420 (2001).

[24] Weinacht, T. C. and Bucksbaum, P. H. *J. Optics B* **4**, R35–R52 (2002).

[25] Zhu, W. and Rabitz, H. *Int. J. Quant. Chem* **93**, 50 (2003).

[26] Brumer, P. W. and Shapiro, M. *Principles of the Quantum Control of Molecular Processes.* Wiley-Interscience, Hoboken, NJ, (2003).

[27] Rice, S. A. and Zhao, M. *Optical Control of Molecular Dynamics.* Wiley-Interscience, New York, NY, (2000).

[28] Geremia, J., Zhu, W., and Rabitz, H. *J. Chem. Phys.* **113**, 10841 (2000).

[29] Langhojer, F., Cardoza, D., Baertschy, M., and Weinacht, T. *J. Chem. Phys.* **122**, 014102 (2005).

[30] Langhojer, F. and Weinacht, T. C. *Toward understanding closed loop learning control: The importance of basis in searching the phase space.* PhD thesis, Stony Brook University, (2004).

[31] Geremia, J. M., Weiss, E., and Rabitz, H. *Chem. Phys.* **267**, 209–222 (2001).

[32] Herek, J. L., Wohlleben, W., Cogdell, R. J., Zeidler, D., and Motzkus, M. *Nature* **417**, 533–535 (2002).

[33] Tannor, D. J. and Rice, S. A. *J. Chem. Phys.* **83**(10), 5013–5018 (1985).

[34] White, J. L., Pearson, B. J., and Bucksbaum, P. H. *J. Phys. B: At. Mol. Opt. Phys.* **37**, L399–L405 (2004).

[35] Ammasov, M., Delone, N., and Krainov, V. *Sov. Phys. JETP* **64**, 1191 (1986).

[36] Tong, X., Zhao, Z., and Lin, C. *Phys. Rev. A* **66**, 033402 (2002).

[37] Anand, S., Zamari, M., Menkir, G., Levis, R., and Schlegel, H. *J. Phys. Chem. A* **108**, 3162 (2004).

[38] Hankin, S., Villeneuve, D., Corkum, P., and Rayner, D. *Phys. Rev. A* **64**, 013405 (2001).

[39] Schmidt, M., Baldridge, K., Boatz, J., Elbert, S., Gordon, M., Jensen, J., Koseki, S., Matsunaga, N., Nguyen, K., Su, S., Windus, T., Dupuis, M., and Montgomery, J. *J. Comput. Chem* **14**, 1347 (1993).

[40] Møller, C. and Plesset, M. *Phys. Rev.* **46**, 618 (1934).

[41] Baruah, T. and Pederson, M. *private communication* (2004).

[42] Ivanov, M., Seideman, T., Corkum, P., Ilkov, F., and Dietrich, P. *Phys. Rev. A* **54**, 1541 (1996).

[43] Chelkowski, S. and Bandrauk, A. *J. Phys. B* **28**, 723 (1995).

[44] Garavelli, M., Page, C. S., Celani, P., Olivucci, M., Schmid, W. E., Trushin, S. A., and Fuss, W. *J. Phys. Chem. A* **105**, 4458–4469 (2001).

[45] Lein, M., Erdmann, M., and Engel, V. *J. Chem. Phys.* **113**, 3609 (2000).

[46] Goswami, D. *Physics Reports* **374**, 385 (2003).

[47] Gibson, G., Coffee, R., and Fang, L. *Phys. Rev. A* **73**, 023418 (2006).

[48] Skovsen, E., Stapelfeldt, H., Juhl, S., and Molmer, K. *Phys. Rev. Lett.* **91**, 090406 (2003).

[49] Ititani, J., Levesque, J., Zeidler, D., Niikura, H., Pepin, H., Kieffer, J., Corkum, P., and Villeneuve, D. *Nature* **432**, 867 (2004).

[50] Ohmori, K., Katsuki, H., Chiba, H., Honda, M., Hagihara, Y., Fujiwara, K., Sato, Y., and Ueda, K. *Phys. Rev. Lett* **96**, 093002 (2006).

[51] Cardoza, D., Pearson, B., Baertschy, M., and Weinacht, T. *J. Photochem. Photobio.* **180**, 277 (2006).

[52] Brown, R. and Weinacht, T. C. *Design and construction of system for sub-20fs pulses through self-phase modulation.* PhD thesis, Stony Brook University, (2006).

[53] Flickinger, D. and Weinacht, T. C. *Design and construction of system for ultrafast ultraviolet-blue pump-probe exposure of biological samples.* PhD thesis, Stony Brook University, (2005).

Appendix A

Genetic Algorithm Operators

This appendix discusses some of the details about our genetic algorithm. In particular, we will present details about the parameters of the GA.

Typically, a generation of pulse shapes consisted of forty pulses. Each pulse's genetic code typically consisted of twenty numbers. These twenty genes then encoded the spectral phase.

In all of the closed-loop learning control experiments discussed in this thesis, we used two operators to perform the mating functions described in Chapter 2. These two operators were two-point crossover and mutation. In two-point crossover, two points in the genetic code of two pulse shapes are randomly selected. This divides the two pulse shapes into three sections. The operation occurs when the code between the two selected genes are swapped between the pulses. This then creates two children pulses that have genetic

code from both parents. If we define the parents' genes to be

$$P_1 = x_{i1}G_{i1}P_2 = x_{i2}G_{i2} \tag{A.1}$$

where x_{i1} and x_{i2} are the gene values and G_{i1} and G_{i2} are the N genes. If we choose two indices j and k in each parent, then the operator creates the two children

$$C_1 = \begin{cases} x_{i1}G_{i1} & , \quad 1 \leq i < j \\ x_{i2}G_{i2} & , \quad j \leq i \leq k \\ x_{i1}G_{i1} & , \quad k < i \leq N \end{cases} \tag{A.2}$$

and

$$C_1 = \begin{cases} x_{i2}G_{i2} & , \quad 1 \leq i < j \\ x_{i1}G_{i1} & , \quad j \leq i \leq k \\ x_{i2}G_{i2} & , \quad k < i \leq N \end{cases} \tag{A.3}$$

In the mutation operator, each gene in each pulse shape has some probability of changing, similar in concept to mutation in nature. However, we are able to define the parameters of this change. In our case, each gene as a small probability of changing ($\sim 2\%$), and the mutation changes the gene to a number randomly selected from a gaussian distribution of numbers with width, σ (~ 0.05), centered about zero. We can express the mutation operator

Table A.1 Parameters used in our implementation of the genetic algorithm.

Parameter	Quantity
Population size	40
Number of Genes	20
% Survive	50
% Mutate	20
% Crossover	70
% Elite	10
Mutation Rate	0.02
Mutation spread (around 0)	0.05

as

$$C = \begin{cases} x_i G_i \rightarrow y_i G_i & if \quad P < 0.02 \\ \\ x_i G_i \rightarrow x_i G_i & if \quad P > 0.98 \end{cases} \tag{A.4}$$

where y_i is chosen by the gaussian distribution centered about zero,

$$y_i = \frac{1}{\sqrt{2\pi}} e^{-\frac{1}{2\sigma^2}}. \tag{A.5}$$

A summary of the typical parameters of the GA implemented in our lab are shown in Table A.1. It should be noted that the GA is programmed is such a way that all of the rates and quantities in Table A.1 can be changed. The quantities presented here are typically used values.

Appendix B

Molecular ADK Enhanced Ionization Calculation

This appendix displays the code used to calculate the enhanced ionization distance for TFA. This code makes the approximation that the TFA ion is "diatomic" like. This code was written in Matlab.

```
%ADK code to study ionization rate based on Misha Ivanov and
%Paul Corkum's model for enhanced ionization of molecular ions
%All units are atomic units unless otherwise stated

%field amplitude
amp=0.0585;%*sqrt(2.3/1.4); % Based roughly on the
                            %intensities we measure
                            %for pump probe data -
                            %should be checked
%laser frequency (nu)
freq=0.0093;
%timesteps to evaluate ionization rate at
dt=2;
t=-1000:dt:1000;
r=2:0.2:12;
```

```
%charges for the two 'nuclei' in our 'diatomic molecule'
Za=1;
Z=1;
IP=0.3; % from NIST chemistry webbook value for Ip for CF3
        %Using a relatively high value from the spread of
        %measured values in order to get as close to the
        %vertical Ip as possible, since many methods measure
        %adiabatic
IP2=0.56;% using triplet state for CH3COCF3++
         %from Mark's MP2 calculations -vertical Ip
m=0;
l=0;
l1=1;
l2=2;
l3=3;
l4=4;
am=abs(m);
kappa=sqrt(2*IP);

%Here are rates for SO
Cl=0;
Cl1=0.41;
Cl2=-0.31;
Cl3=0.01;
Cl4=0;

[T,R]=meshgrid(t,r);

%electric field
%FWHM is 30fs so in atomic units that means 1240 au of time,
%and thus tau=FWHM/(sqrt(2ln2)), we get tau=1240/1.66=744
envelope=exp(-(T/(1053)).^2);
carrier=cos(2*pi*freq*T);
F01=amp.*envelope.*carrier;
F0=abs(F01);
%for the upper adiabatic state, the fields
%always add! New line here to roughly account for field at
%barrier max according to r0 code - what you really want is the
%field of the ion at saddle point of the inner barrier for the
%inner barrier term - the code r0.m calculates the saddle point
```

```
%position whose variation with field strength is roughly given
%by the formula below
R0=R/2.*(1-F0/(0.1));
Fion=Za./(R-R0).^2; % using the field at the saddle point
Ftot=F0+Fion;

%calculate the stark shift term
stark=(F0.*R)/2;
IP2red=(-(0.76196+(0.54362-0.76196)./(1+10.^(R-3.21635)))
+(.7620+.5572))-stark;
kappa2=sqrt(2*IP2red);
Zadd=Za+Z;

%factorial term
q=(-1)^m*sqrt(((2*l+1)*factorial(l+am))/(2*factorial(l-am)));
q1=(-1)^m*sqrt(((2*l1+1)*factorial(l1+am))/
   (2*factorial(l1-am)));
q2=(-1)^m*sqrt(((2*l2+1)*factorial(l2+am))/
   (2*factorial(l2-am)));
q3=(-1)^m*sqrt(((2*l3+1)*factorial(l3+am))/
   (2*factorial(l3-am)));
q4=(-1)^m*sqrt(((2*l4+1)*factorial(l4+am))/
   (2*factorial(l4-am)));

%B^2term term
B2=((Cl*q)+(Cl1*q1)+(Cl2*q2)+(Cl3*q3)+(Cl4*q4))^2;

%Now ionization rate for internal barrier
w1=(B2/((2^am)*factorial(am))).*(1/(kappa^((2*Z)/kappa-1)))
.*((2*kappa^3)./Ftot).^((2*Z)/kappa-am-1)
.*exp((-2*kappa^3)./(3*Ftot));

%external barrier term
w2=(B2/((2^am)*factorial(am)))
.*(1./(kappa2.^((2*Zadd)./kappa2-1)))
.*((2.*kappa2.^3)./F0).^((2*Zadd)./kappa2-am-1)
.*exp((-2.*kappa2.^3)./(3*F0));

%Now wupper
%the 0.01 in the next equation (or generally the factor in
```

```
front of wtot is just to control the absolute ionization
%rate ADK tends to overpredict rates and so we limit the
%rate here, which also takes into account the fact that not 100
%percent of the wavefunction
%will be trapped in the upper adiabatic state. We're not
%really interested in absolute rates here, so our main concern
%lies in not saturating and seeing the dependence on C-C bond
%length.
wtot=0.5*(w1.*w2)./(w1+w2+1e-8);
%now probability
figure;
time=ones(1,max(size(t)));
int1=abs(wtot)*time';
size_int1=size(int1);
int1=int1*dt; %step size in atomic units to make
              %integral scaled properly
prob=1-exp(-1*int1);
plot(r,(prob),'k','linewidth',3);
setaxesa
xlabel('C-CF_3 bond length (Angstroms)');
ylabel('IonizationProbability');
```